

ScuDo
Scuola di Dottorato ~ Doctoral School
WHAT YOU ARE, TAKES YOU FAR

Doctoral Dissertation
Doctoral Program in Physics (30th Cycle)

Hybrid Resistive Switching Devices Based on Soft Nanocomposites

By

Krishna Rajan

******

Supervisors:
Prof. C. F. Pirri
Prof. C. Ricciardi
Prof. A. Chiolerio

Doctoral Examination Committee:
Prof. Cicero. Giancarlo, Referee, Politecnico Di Torino
Prof. Daghero. Dario, Referee, Politecnico Di Torino
Prof. Iannotta. Salvatore, Referee, Consiglio Nazionale delle Ricerche, Parma
Prof. Spiga. Sabina, Referee, Consiglio Nazionale delle Ricerche, Agrate Brianza
Prof. Truccato. Marco, Referee, University of Turin

Politecnico di Torino
2018

Declaration

I hereby declare that, the contents and organization of this dissertation constitute my own original work and does not compromise in any way the rights of third parties, including those relating to the security of personal data.

Krishna Rajan

2018

* This dissertation is presented in partial fulfillment of the requirements for **Ph.D. degree** in the Graduate School of Politecnico di Torino (ScuDo).

I would like to dedicate this thesis to my loving parents

Acknowledgments

At the very outset, I would like to thank my parents who had given me the mental and emotional strength and support for the tough journey called Ph.D. I wish to thank Prof. Alessandro Chiolerio, my advisor, who was instrumental throughout my research programme. I have been very fortunate to learn a lot from him during this short span of time. It has always been a great pleasure and pleasant experience to have associated with Dr. Chiolerio especially when in conversation on various aspects of life and science. I am also grateful to Prof. Carlo Ricciardi for serving as my co-advisor. I would also like to take this opportunity to thank Dr. Sergio Bocchini, Dr. Annalisa Chiappone, Dr. Ignazio Roppolo, Dr. Dennis Perrone, Dr. Katarzyna Bejtka, Dr. Marco Fontana and Dr. Adriano Sacco for all their wonderful support during my PhD.

I must thank Politronica Inkjet Printing S.r.l for helping me with inkjet printing. The support that they have extended to me was immensely helpful. Some of the results presented here are the results of collaboration with Prof. Joshua Yang's team. I am grateful to Dr. Yang and his team at the University of Massachusetts. I would also like to acknowledge my gratitudes to Mr. Ye Zhuo of Prof. Yang's team for teaching me some device fabrication techniques.

Last but not least, I would like to acknowledge my heartfelt thanks to my husband Dr. Jijeesh Ravi Nair., who was always there with me throughout the process and helping me by way of providing significant scientific inputs which has tremendously helped me in achieving excellent results.

Abstract

This thesis investigates the preparation and characterization of organic Nano composite (NC) based hybrid Resistive switching device (RSD) or memristor. The research in this field has been going on for years, yet a proper device with a unified working principle has never been developed in practical memory application. The main aim of the research activity is to fabricate an RSD based on organic nanocomposite and to focus on its working mechanism, material properties and electrical characteristics in detail. Several experiments were conducted to obtain an optimized hybrid device measuring its endurance, memory retention, memory window (On/Off) etc. The initial stage of research dealt with the development of a planar symmetric RSD based on Silver NC. Here the resistive switching was explained in terms of field-induced formation of conductive filament along the silver clusters. This work enables the assembling of a logic device, which exhibits a bipolar non-volatile switching behaviour that is controlled by means of the current compliance level. The work further progressed with the use of silver salt along with Ionic Liquid (IL) in various polymeric matrices. This active matrix worked well both on symmetric (RSDs with identical electrodes) as well as on asymmetric RSDs (RSDs with electrodes made different metal). The addition of room temperature Ionic Liquid plays an important role in initiating permanent memory and reducing the set voltage range which was a real eye opener in the present research work. The presence of well dispersed silver ions in the polymer matrix which has a great diffusivity, helps to maintain reversible electrochemical states that store information or logic bits in the form of

recoverable conducting filament in our polymer based hybrid switching matrix. In this work, we present a detailed study showing the interaction between the polymer and the Nano particles by means of various techniques. The hybrid switching matrix based RSDs discussed here, present some of the best results obtained worldwide in the field of Polymer hybrid RSDs. The active switching matrices prepared throughout our research enables an easy deposition onto various substrates thus widening printed electronics potentialities. The final part of the thesis deals with the fabrication and characterization of a low power, high speed hybrid selector device.

Contents

1. Introduction 1
   1.1 Thesis Organization 1
   1.2 Overview of device technologies for storage devices 2
   1.3 The missing circuit element 3
   1.4 Memristors or Resistive Switching Devices 7
      1.4.1 Resistive switching behaviours 8
      1.4.2 Types of resistive switching devices 9
   1.5 Applications 15
      1.5.1 Memory Devices 15
      1.5.2 The artificial synapse 17
   1.6 State Of The Art 18
   1.7 References 21
2. Materials, Methods & Technologies 34
   2.1 Introduction 34
   2.2 Device Architecture 34
      2.2.1 Planar Symmetrical Device based on Au electrodes 35
      2.2.2 Planar Asymmetrical Device based on Ag and Pt electrodes 35
      2.2.3 Stacked Device 36
   2.3 Polymer NC based Switching Matrix Preparation 38
      2.3.1 Ex-Situ Ag based Switching matrix 38
      2.3.2 In-Situ Ag based Switching matrix 41

2.3.3 PVDF-HFP_$AgNO_3$_Ionic Liquid....42
2.3.4 PEO_$AgNO_3$_Ionic Liquid....45
2.3.5 PMMA_$AgNO_3$_Ionic Liquid....47
2.3.6 PMMA. A2_Au NPs....47
2.4 Switching Matrix Deposition Techniques....48
2.4.1 Spin Coating....48
2.4.2 Inkjet Printing....48
2.5 Characterization Techniques....49
2.6 References....52
3. Metallic Ag NP based RSD....54
3.1 Introduction....54
3.2 Nanoparticle Synthesis Methods....55
3.3 Ex-Situ Ag Based RSD....56
3.3.1 Device Fabrication....57
3.4 In-Situ Ag Based RSD....75
3.5 References....77
4. Ionic Liquid embedded Fluoro polymer composite based RSDs....83
4.1 Introduction....83
4.2 Planar symmetrical device based on PVDF-HFP_$AgNO_3$_IL....83
4.3 Planar Asymmetrical device based on PVDF-HFP_$AgNO_3$_IL.....91
4.4 Stacked Asymmetrical device based on PVDF-HFP_$AgNO_3$_IL.....92
4.5 References....95
5. PEO Based Smart Hybrid Devices....97
5.1 Introduction....97
5.2 PEO based planar symmetrical device....98
5.3 PEO based planar Asymmetrical device....100
5.3.1 Planar asymmetrical device based on PEO_$AgNO_3$_IL....100
5.3.2 Planar asymmetrical device based on PEO_IL....106

5.4 Switching Mechanism of PEO based smart hybrid RSDs.....111
5.5 References 115
6. Performance comparison of hybrid RSDs.....118
6.1 Introduction 118
6.2 Electrical Characteristics of individual RSDs 118
6.2.1 PVDF-HFP based hybrid device.....119
6.2.2 PEO based hybrid device.....120
6.2.3 PMMA based hybrid device 121
6.3 Comparison study.....123
6.4 References 129
7. PMMA based ultra-low voltage switching device 131
7.1 Introduction 131
7.2 PMMA and Au NP based threshold switching device 132
7.3 Device Switching Speed Analysis.....134
7.4 References 138
8. Summary and Conclusion.....139
8.1 Summary of Results 139
8.2 Conclusion and Future Outlook.....142

List of Figures

Figure 1.1: The four fundamental two terminal circuit elements: resistor, capacitor, inductor and memristor 3

Figure 1.2: Pinched hysteresis loop of memristor (V v/s I). 5

Figure 1.3: Two terminal memrsitor realised by HP. a) TiO2 based representation of the Memristor. b) Coupled variable resistor model 6

Figure 1.4: Types of resistive switching. a) Bipolar Switching. b) Unipolar Switching 9

Figure 1.5: Pictorial representation of field induced metallic filament formation in a hybrid RSD. 11

Figure 1.6: Pictorial representation of resistive switching mechanism in ECM. a) Electrochemically active metal ions migrating to cathode. b) Precipitation of active metal atoms at the electrochmically inert electrode and forms a conducting filament. c) Electrochemical dissolution of the filament with change in applied polarity 13

Figure 1.7: Four regions in the Current v/s Voltage plot 14

Figure 1.8: Read/Write circuit for a memrsitor based memory 16

Figure 1.9: Memristor based circuit mimicking biological synapse.....18

Figure 1.10: Potential fields of applications of memristive devices.....19

Figure 2.1: Schematic representation of the planar device. Inset shows the image of the real device with switching matrix deposited on the device 36

Figure 2.2: Schematic representation of Au/ITO based stacked device. Inset provides the real image of the stacked device. 37

Figure 2.3: SEM image of BE deposited using dog bone shadow mask. 38

Figure 2.4: TGA analysis performed on Ag NP suspension.....39

Figure 2.5: Schematic representation of the finally prepared Ag NP based switching matrix 40

Figure 2.6: SEM image of the switching composite.....40

Figure 2.7: Impedance measure performed on the Ag NO and PVDF-HFP based switching matrix. 41

Figure 2.8: DSC thermograms of pure Poplymer (PVDF-HFP), PVDF-HFP_$AgNO_3$ and finally PVDF-HFP_$AgNO_3$_IL 43

Figure 2.9: FESEM image of the PVDF-HFP_$AgNO_3$_IL matrix at different magnifications.....44

Figure 2.10: ATR FTIR spectra of PVDF-HFP_$AgNO_3$_IL.....44

Figure 2.11: Switching matrix characterization. a)FESEM image of the PEO_$AgNO_3$_IL matrix. b) Nyquist response of PEO_$AgNO_3$_IL matrix.....46

Figure 2.12: DSC thermograms of pure Polymer (PEO) and PEO_AgNO3_IL matrices.....47

Figure 2.13: Voltage waveform applied to generate ink droplet. Inset provides the ink drop ejected from the nozzle.....49

Figure 2.14: Probe set up for electrical measurement in stacked Asymmetrical device 50

Figure 3.1: Initial electroforming process taking place at 13V 58

Figure 3.2: DC cycling after electroforming Process. a) Consecutive set process after electroforming. b) Variation in Set voltage with cycles.....58

Figure 3.3: Electrical characterization performed on RSD. a) Cyclic IV performed on RSD in logarithmic scale at 10 µA current compliance. b) Cyclic IV performed on RSD in logarithmic scale at 1 mA current compliance 59

Figure 3.4: Optical characterization performed on the RSD a) FESEM image of the volatile characterized device b) Optical microscopy image of the characterized sample (non-volatile) after performing a mathematical algorithm to enhance the difference in the active gap before and after electrical characterization(The region between the orange lines constitute the active gap between the Au electrodes.) 61

Figure 3.5: On Resistance and Off current plotted as a function of set Compliance current. 62

Figure 3.6: Pulse characterization performed on the non-volatile device. 63

Figure 3.7: SEM image of the spin coated Ag and PVDF-HFP based switching matrix (side view) on the RSD 64

Figure 3.8: Viscosity measurement carried out on the Ag NP and PVDF-HFP based ink 65

Figure 3.9: Schematic representation of the ink jet printed planar device using different techniques a) polymer NC being inkjet printed using DOP mode, inset: physical device after polymer NC printing and b) polymer NC being inkjet printed in POF mode, inset: physical device after Ag NC printing. 66

Figure 3.10: Electrical characterization performed on DOP RSD a) Initial electroforming at 32.5 V. b) Cyclic I-V performed on DOP in logarithmic scale at 10 µA set and reset current compliance. c) Cyclic I-V performed on DOP in logarithmic scale at 100 µA set compliance and 1mA reset compliance 67

Figure 3.11: Pulse characterization performed on the non-volatile device. 69

Figure 3.12: optical characterization performed on DOP RSD a) FESEM image of the device with active switching matrix inkjet printed between the gold electrodes, after electrical characterization b) Optical microscopy image of the characterized sample after false colour mapping 69

Figure 3.13: High-Resolution survey on Ag^{3d} spectrum of the aged DOP RSD. Inset provides the electrical characterization result carried out on the aged device 70

Figure 3.14: Electrical characterization performed on POF RSD a) Initial Cyclic I-V measurement on the device. b) Plot showing the HRS of the first cycle in both polarities (continuous line showing smoothing by means of Savitzky-Golay filter). c) I-V measurement carried out at reduced voltage range 71

Figure 3.15: Tests performed on aged POF RSD a) SEM image before characterization b) Electrical characterization performed on the aged device. c) SEM imaging performed after characterization.....72

Figure 3.16: Schematic representation of the active gap between the electrodes of a) DOP RSD and b) POF RSD 73

Figure 3.17: Schematic representation of field induced filament formation and destruction in Ex-Situ based RSD. Green circles represents the Ag NPs.....74

Figure 3.18**:** DC characterization performed on In-Situ based RSD. Inset provides the electroforming process.....75

Figure 4.1: Electrical characterization performed on the planar symmetrical device. a) Initial set taking place at -25V. b) Complete cyclic IV measure. Inset provides Zoom near -0.6 to +0.6 V, to understand the transition from LRS to HRS

in both polarities. c) FESEM image of the device with active switching matrix spin coated between the gold electrodes, after electrical characterization, inset: Magnified portion between the electrodes. 85

Figure 4.2: Electrical characterization performed on the planar symmetrical device with PVDF-HFP_$AgNO_3$_IL as switching matrix. a) Initial set taking place at -2.2V. b) Complete cyclic IV measure with 100µA compliance. Inset shows the further reduction of initial set with increase in $AgNO_3$ concentration c) Cyclic IV measure at higher reset compliance. d) Behavior of a single cycle at 1mA reset compliance. 86

Figure 4.3: Nyquist response of the Matrix 1 and Matrix 2 analyzed from 1 kHz to 10 MHz 88

Figure 4.4: FESEM image of the characterized sample. a) Image of the switching gap with spin coated PVDF-HFP_$AgNO_3$and IL after electrical characterization. b) Magnified portion between the electrodes with percolation paths (evidenced by orange hand drawn lines) and Ag NPs (coloured in green) that bridge the two electrodes 88

Figure 4.5: Retention characteristics of the device read at 0.05V. 89

Figure 4.6: X-ray photoelectron spectra of NC based RSD prepared with PVDF-HFP_$AgNO_3$_IL on planar device. a) Survey Spectra. B) High Resolution (HR) spectra for N1s. c) HR spectra for Ag3d peaks (black line for experimental data, dashed black line for fitting curves and green line for reconstructed signal). The analyses are made on fresh untested sample (Fresh: not tested), sample after electrical characterization (Not Aged), on a one-month-aged sample submitted to electrical characterization (Aged), which was kept at ambient conditions, and finally on commercial $AgNO_3$ powder (a and b graphs only). 90

Figure 4.7: Electrical Characterization performed on planar asymmetrical device with PVDF-HFP_$AgNO_3$_IL as switching matrix. a) Initial electroforming taking place at 2.29 V. b) Cyclic IV behaviour after forming. 92

Figure 4.8: General IV behavior of the stacked device. 93

Figure 4.9: Pulse test carried on the stacked device. a) Input pulse signal applied. b) Output obtained 94

Figure 5.1: Electrical Characterization performed on PEO_AgNO3_IL based planar symmetrical device. a) Forming Process. b) Behaviour of individual cycle in logarithmic scale. c) Subsequent cycles after forming. d) On/Off current at a read voltage of 0.5V throughout continuous cyclic sweeps 99

Figure 5.2: FESEM imaging on the RSD. a) Fresh device with switching matrix coated. b) Electrically characterized sample 99

Figure 5.3: Electrical Characterization performed on PEO_$AgNO_3$_IL based planar asymmetrical device. a**)** Forming process. b**)** Continuous resistive switching taking place throughout the 500 working cycles. c**)** On and Off current read at 0.1V throughout continuous cyclic sweeps. d) Retention test carried out on the device. e) Set and reset voltage levels throughout the cyclic sweeps. 101

Figure 5.4: Electrical characterization carried out to study about the formed filament a) On Resistance and Off Current plotted as a function of Compliance current. b) On Resistance plotted as a function of Temperature. 102

Figure 5.5: Optical microscopy and FESEM imaging performed on a single RSD. a) Optical micrograph of pristine device. b) Device imaged after switching on the device (inset shows the corresponding IV sweep). c) FESEM image corresponding to panel b 103

Figure 5.6: FESEM image of planar asymmetrical device showing the evolution of formed filament with an increase in number of cycles. a) RSD before electrical characterization. b) After 10 cycles of cyclic sweeps. c) 100 consecutive cyclic sweeps. d) 500 consecutive cyclic sweeps. (The red colored connections between the electrodes is by a mathematical algorithm performed to enhance the difference in the active gap after different number of cyclic sweeps) 104

Figure 5.7: Real-time observation of the filament formation and annihilation. In the left we have the real FESEM images and the corresponding right side panels are the images that have been subjected to a mathematical algorithm to enhance the differences between the real FESEM images taken before and after stress (grey area corresponds to tungsten nano probe). a) Filament formation at set threshold. b) Filament dissolution at reset threshold c) Further filament formation. 105

Figure 5.8: Cyclic curve showing reset process a) negative polarity cycled till -0.6V b) after further increasing the negative sweep voltage to -2V. 106

Figure 5.9: Electrical characterization performed on the planar asymmetric RSD with PEO_IL as switching matrix. a) Forming process b) IV behavior of a single cycle shown in logarithmic scale. c) On/Off current ratio read at 1.5 V throughout continuous cyclic sweeps. d) Retention test performed on the device. 107

Figure 5.10: FESEM imaging and EDX carried on RSD with PEO and IL as switching matrix a) FESEM image of the asymmetrical RSD with the entire

switching gap. b) Individual Silver filament between the electrodes. c) EDX line profile concerning the silver intensity in the active gap. 108

Figure 5.11: Represents the metallic Ag filament growth in PEO_IL matrix based RSD. a) Schematic representation of the Ag filament growth. b) Current-time plot of the RSD 110

Figure 5.12: Schematic representation of the switching mechanism in planar symmetric device. a) Pristine device. b) Device in On state. c) Device in Off state. [Gray circles corresponds to Ag ions from the $AgNO_3$, Red circles corresponds to Nitrate ions, Circles with A and C corresponds to the anion and cation part of the IL. All these are dispersed in the polymer matrix] 112

Figure 5.13: Schematic representation of the switching mechanism in planar asymmetric device. a) Pristine device. b) Device in On state. c) Device in Off state. [The red circle corresponds to the region on the Ag electrode from where the Ag ions have been oxidised and diffused into the switching matrix] 113

Figure 5.14: Schematic representation of the switching mechanism in planar asymmetric device with PEO_IL as switching matrix. a) Pristine device. b) Device in On state. c) Device in Off state. [The red circle corresponds to the region on the Ag electrode from where the Ag ions have been oxidised and diffused into the switching matrix] 114

Figure 6.1: Electrical characterization performed on the planar asymmetric RSD with $AgNO_3$_IL_PVDF-HFP as switching matrix. a) Initial electroforming taking place at 2.29 V. b) Cyclic IV behaviour after forming. c) FESEM performed in the active switching gap of the RSD. d) On/Off current ratio at a read voltage of 0.1 V throughout continuous cyclic sweeps. 120

Figure 6.2: Electrical characterization performed on the planar asymmetric RSD with $AgNO_3$_IL_PEO as switching matrix. a) Initial electroforming taking place at 8.4 V. b) Cyclic IV behaviour of remaining cycles after forming. c) FESEM performed in the active switching gap of the RSD. d) On/Off current ratio at a read voltage of 0.5V throughout continuous cyclic sweeps. 121

Figure 6.3: Electrical characterization performed on the planar asymmetric RSD with $AgNO_3$_IL_PMMA as switching matrix. a) Initial electroforming taking place at 6.5 V. b) Cyclic IV behaviour of remaining cycles after forming. c) FESEM performed in the active switching gap of the RSD. d) On/Off current ratio at a read voltage of 0.5V throughout continuous cyclic sweeps. 122

Figure 6.4: FESEM imaging on the active gap of the RSD before and after characterization. a,b: Device before and after characterization of A_gNO_3_IL_PVDF-HFP based matrix. c,d: Device before and after characterization of A_gNO_3_IL_PEO based matrix. e,f: Device before and after characterization of A_gNO_3_IL_PMMA based matrix. 124

Figure 6.5: DSC thermograms of the polymer based switching composites and individual components of the switching matrix. a) A_gNO_3 b) IL c) PVDF-HFP. d) $AgNO_3$_IL_PVDF-HFP. e) PEO. f) $AgNO_3$_IL_PEO. g) PMMA. h) $AgNO_3$_IL_PMMA. 125

Figure 6.6: FESEM images of the films composed of 3 different NCs. a) $AgNO_3$_IL_PVDF-HFP. b) $AgNO_3$_IL_PEO. c) $AgNO_3$_IL_PMMA. 127

Figure 7.1: Electrical Characterization performed on the device. a) Cyclic IV performed on the device. b) Closer look at the negative cycle. c) On and Off current read at -180 µV from the cyclic IV curve 133

Figure 7.2: Pulse endurance performed on the device. a) Pulse input. b) Output 133

Figure 7.3: Switching speed determination test. a) Input pulse in black and the output current obtained (blue). b) The zoom in section of the switching part. c) Plot of switching speed as a function of set voltage 134

Figure 7.4: Relaxation time determination test. a) Input pulse in black and the output current obtained (blue). b) The zoom in section of the relaxed part. c) Plot of relaxation time as a function of set voltage 135

Figure 7.5: Arrhenius plot: Switching speed plotted as function of Temperature 136

Figure 7.6: Schematic plot showing the state transition of the device due to Electrostriction effect 137

Figure 8.1: Ph.D. Work Time frame 140

List of Tables

Table 1.1: Basic Circuit components and their corresponding differential equation. 6

Table 1.2: Specifications of already available commercial memory technologies v/s Memristor device 20

Table 6.1**:** Summary of the electrical measurement data obtained from the RSD using 3 polymer matrices. 123

Table 6.2: Values of ΔHm and ΔHm0 of PVDF-HFP and PEO matrix 126

Table 8.1: Table summarizing the entire results obtained so far 141

Chapter 1

Introduction

1.1 Thesis Organization

The thesis is organized as follows:

Chapter 1 provides a brief overview on the existing memory technologies and their limitations. This leads to our discussion on memristors or Resistive Switching Devices (RSD). A detailed explanation on types of switching devices and switching behaviors has been given. This chapter is concluded by discussing the main applications and the present state of art of these devices.

Chapter 2 describes the materials, methods and technologies used in the present research work. This chapter deals with the experimental procedures, setups and various technologies used. In *Chapter 3,* we start discussing about the different polymer NC used to develop RSDs. This section provides the explanation on metallic silver nano particle based RSDs. The work gives a detailed explanation on the switching mechanism and electrical parameter dependence on the switching behavior. This chapter also discuss about various deposition techniques used to deposit the switching matrix, and the difference in the switching behavior based on these techniques. *Chapter 4* deals with a slightly different type of switching matrix. This consists of a polymer matrix and a metallic salt. After further studies, it was observed that the addition of Ionic Liquid (IL) into this matrix, improved the device switching behavior. Two different device architectures have been explained here. The difference in

switching behavior with respect to the device architecture has been presented and explained.

Chapter 5 deals with PEO, Silver salt and IL based switching matrix. RSD based on this switching matrix exhibits the best performance among all the previously discussed devices. Here we have explained about the device electrode symmetry and its dependence on the switching behavior. This particular polymer composite that we have synthesized can be considered as an excellent switching matrix for future organic RSDs. *Chapter 6* provides a performance comparison of various RSDs based on different switching matrices. This chapter deals with the switching performance of PEO, PVDF-HFP and PMMA based IL and $AgNO_3$ embedded RSDs. The comparison study was performed on planar asymmetrical devices. The major switching differences seen in the 3 devices were explained based on the physical and chemical properties of the switching matrix. *Chapter 7* deals with low power and high speed switching devices based on polymer NC. The results that we have obtained with this device have been presented as they display some interesting results which has not been previously reported. *Chapter 8,* summarizes the results presented in the entire thesis. The final part of this chapter concludes the thesis and proposes future prospective applications.

1.2 Overview of device technologies for storage devices

A simple prediction by Gordon Moore in the year 1965 opened a powerful economic cycle of investments. This statement "number of devices that can be integrated on a chip of fixed area would double every 12 months" [**1**] became the driving force behind the dramatic reduction in the unit cost for high density memory devices [**2**].

Memory devices have always played a significant role in the market of electronic devices. Flash memory is one of the most important type of electronically erasable programmable read only memory (EEPROM) which is found everywhere including smartphones, digital cameras, PC etc. As with other solid-state technologies, flash memory's history includes rapidly increasing capacity, smaller physical sizes, and constantly falling prices. This powerful electronic economic industry based on flash is anticipated to run out of the road in 2020s due to scalability issues in underlying device physics and fabrication processes [**3**]. This paves the way for alternative technologies. The bigger question which remains unanswered is that if these new technologies could actually integrate dynamic memory (RAM) and non-volatile memory in a single universal memory tech. Under these circumstances several non-volatile memory

technologies based on various concepts have been introduced like ferroelectric random access memory, magneto resistive random access memory, Phase change random access memory and Resistive switching random access memory [**4-7**]. Resistive Switching memories can be generally viewed as "Memristors". Memristor or Resistive Random Access Memory (ReRAM) which is supposed to be an integral part of future computing devices is presently one of the most interesting research fields.

1.3 The missing circuit element

It was during the year 1971 that Leon Chua, a circuit theorist conceived the idea of a missing passive two-terminal electrical component [**8**] and postulated its existence mathematically. Although in 1971 he showed that such an element had many interesting and valuable circuit properties, it didn't gain its importance until HP came up with their miraculous development of the Mysterious Memristor in 2008 [**9**]. Chua noted that there were six different mathematical relations connecting the four fundamental circuit variables: current *i*, voltage *v*, charge *q* and flux *φ*. **Figure 1.1** provides these basic relations between the variables and the circuit elements.

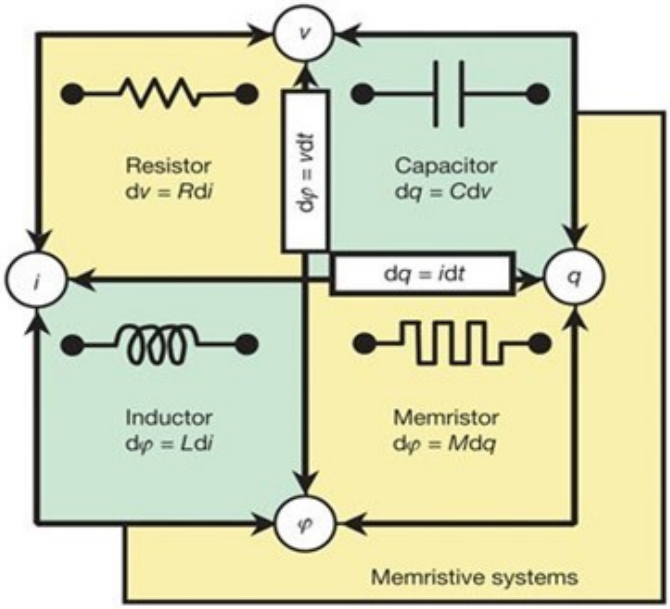

Figure 1.1: The four fundamental two terminal circuit elements: resistor, capacitor, inductor and memristor [**9**].

The missing element which is the Memristor is characterised by its Memristance M, which provides a functional relation between charge and flux,

$$d\varphi = Mdq \tag{1.1}$$

Memristor has originally been defined in terms of a non-linear functional relation between flux linkage $\varphi(t)$ and the amount of charge that has flowed through the device $q(t)$:

$$f\big(\varphi(t), q(t)\big) = 0 \tag{1.2}$$

Where $\varphi(t)$ and q are the time domain integrals of memristor electric voltage v and electric current i.

$$\varphi(t) = \int_{-\infty}^{t} v(t)dt \tag{1.3}$$

And

$$q(t) = \int_{-\infty}^{t} i(t)dt \tag{1.4}$$

In this way a memristor is characterized by its memristance function, which describes the charge-dependent rate of change of flux with charge:

$$M(q) = \frac{d\varphi}{dq} \tag{1.5}$$

Substituting (1.3) in (1.5) we get

$$M(q(t)) = \frac{\frac{d\varphi}{dt}}{\frac{dq}{dt}} = R_M(q) \tag{1.6}$$

Similarly Substituting (1.4) in (1.5) we get

$$M(\varphi(t)) = \frac{\frac{dq}{dt}}{\frac{d\varphi}{dt}} = G_M(\varphi) \tag{1.7}$$

Here $R_M(q)$ and $G_M(\varphi)$ are the Memresisitance and the Memductance at charge q and flux φ respectively. $R_M(q)$ has the unit of Ohms (Ω) and $G_M(\varphi)$ has the unit of Seimens (S)

As explained by Chua, Memristors exhibit a distinctive fingerprint characterized by pinched hysteresis loop which is completely confined to the first and third quadrants of the V-I plane, whose contour shape changes with both the

amplitude and frequency of any periodic sine wave like input voltage and current source [**10**]. **Figure 1.2** provides the basic pinched hysteresis loop of a memristor.

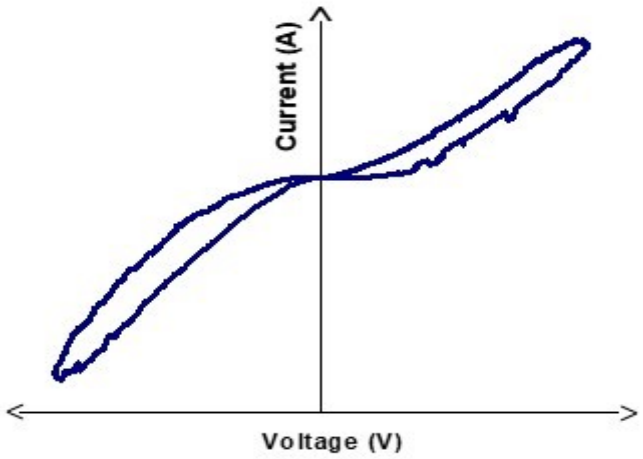

Figure 1.2: Pinched hysteresis loop of memristor (V v/s I).

Equation (1.6) can also be written as:

$$V(t) = M(q(t))i(t) \qquad (1.8)$$

This is very much like a charge dependent Ohm's law. In equation (1.8) if i(t) = 0 then V(t) = 0. Therefore M(t) is a constant (Memory Effect) [**11**].

Table 1.1 sum up all the basic electronic components including the mysterious Memristor and their corresponding defining equations.

As mentioned earlier it was HP to come up with the first experimental working model of a realistic memristor. This memristor was a simple two terminal device. The structure constituted of a TiO_2 thin film which was sandwiched between platinum (Pt) electrodes (**Figure 1.3a**).

Table 1.1: Basic Circuit components and their corresponding differential equation.

Component	Unit	Differential Equation
Resistor	Ohm (Ω)	$R = \frac{dv}{di}$
Capacitor	Farad (F)	$C = \frac{dq}{dv}$
Inductor	Henry (H)	$L = \frac{d\varphi}{di}$
Memristor	*Ohm (Ω)*	$M = \frac{d\varphi}{dq}$

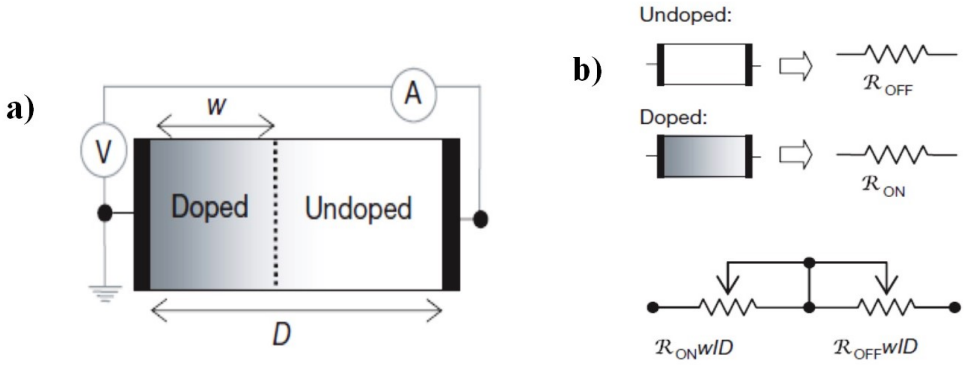

Figure 1.3: Two terminal memrsitor realised by HP. a) TiO2 based representation of the Memristor. b) Coupled variable resistor model **[9]**.

Here the thin semiconductor film (TiO_2) of thickness D (10-30 nm) is sandwiched between the two metal contacts. The semiconductor layer has mainly 2 parts as seen in **figure 1.3a**. It has a region of width 'W' which is doped with oxygen vacancies and thus it behaves as a semiconductor. The undoped region has an insulating property. Therefore when W = D, the resistance of the device can be denoted by R_{ON} and when W = 0, the resistance of the device will be R_{OFF}. Thus the total resistance of this memristor can be denoted as the sum of the

resistance of the resistances of the doped and undoped regions, whose value depends on the value of W as shown in **figure 1.3b**. By applying an external bias V(t) across the device, the boundary between the doped and undoped region shifts due to the drift in the charge dopants. By considering a simple case of ohmic conduction and linear ionic drift in a uniform field with average ion mobility μ_V, we get

$$V(t) = [R_{ON}\frac{W(t)}{D} + R_{OFF}\left(1 - \frac{W(t)}{D}\right)]i(t) \quad (1.9)$$

$$\frac{dW(t)}{dt} = \mu_V \frac{R_{ON}}{D} i(t) \quad (1.10)$$

Thus we can write W(t) as:

$$W(t) = \mu_V \frac{R_{ON}}{D} q(t) \quad (1.11)$$

Putting (1.11) in (1.9) we obtain the expression for Memristance of this system. Here by assuming $R_{ON} << R_{OFF}$ we obtain,

$$M(q) = R_{OFF}[1 - \frac{\mu_V R_{ON}}{D^2} q(t)] \quad (1.12)$$

From equation (1.12) we understand that as the film thickness D decreases or as doping increses thereby increasing μ_V, the memristance of the device also increases. Thus to sum up we can summarise that a memristor is a device whose electrical resistance is not constant but depends on the history of current that had previously flowed through the device.

The development of memristor by HP and the exponential growth of Moore's law and the fear of saturation that is about to reach in the microelectronic industry spurred further research on this topic.

1.4 Memristors or Resistive Switching Devices

Resistive switching has been widely studied in recent years due to the potential applications in nonvolatile resistive memory devices [**12-15**]. Non-volatile memories (NVMs) have become a major technology in storing of digital information. This effect of resistive switching is also the base of the behaviour of memristor devices. Resistive Switching Devices (RSD) are two terminal nonlinear dynamic electronic devices that can have broad applications in the fields of nonvolatile memory, reconfigurable logic, analog circuits, and neuromorphic

computing [**16**]. Even though the concept of two terminal RSDs became significant after 2008, there were many studies reported way back which explained resistance switching in three terminal hybrid electronic devices **[17-19]**. Erokhin et al. [**19**] has demonstrated a 3 terminal hybrid device based on PANI emaraldine base-PEO/LiCl in which the transition in the resistance state was observed due to the electrochemical control of the redox state of PANI. Before explaining more about the RSDs, a detailed explanation of the resistance switching and its different types is needed.

Resistive switching is the physical phenomenon that consists of a sudden and non-volatile change of the impedance due to the application of electric stress, typically voltage or current pulsing. This effect may allow the fabrication of future novel electronic memory concepts, such as non-volatile random access memories (RAM), hence, it is also termed resistive RAM, RRAM, or ReRAM. In the following part we will discuss about the main types of resistive switching.

1.4.1 Resistive switching behaviours

Resistive switching can be divided into two main categories: Switching assisted by filament formation [**20-23**] and switching assisted by an interface [**24**]. Filamentary switching is due to the formation of local conductive filaments, which is formed as a result of redistribution of oxygen vacancies [**25**] or the diffusion of metal ions [**26**]. For interface switching, different mechanisms have been proposed, such as charge trapping [**27**], or polarization switching [**28**].

In most of the organic devices, switching has been attributed to filamentary conduction mechanism. In polymer-based systems, carbonaceous filaments can arise from arrested degradation of the organic film [**29**] or metal filaments might form across organic layer [**20**, **30-32**]. Filamentary conduction can also arise from localized high mobility paths within the polymer material due to defects or field-induced electronic processes [**33**]. In general the filamentary switching happening in most of the devices takes place due to a local redox reaction. Thus this can also be generalised as redox based switching. Redox based switching can be broadly classified into four: Electro Chemical Metallization (ECM) which will be explained further in detail, Valence change mechanism (VCM), Thermo-chemical mechanism (TCM) and Interfacial coupling mechanism (ICM). VCM occurs by the migration of oxygen anions due to an applied field and because of the valence change of the cation sublattice [**34, 35**]. TCM as the name suggests is a temperature assisted process. This process is related to a stoichiometric change in the oxide due to a current induced increase in temperature [**34**]. ICM which has been observed by Chiolerio et al. [**36**] in polymer composite matrices is a

switching effect where the switching is induced by electron transfer between the polymer matrix and the ZnO particles which is assisted by the polymer secondary bonds.

So far there is no unified switching mechanism that has been explained. Mentioning about resistive switching, usually there are two main switching modes observable in devices, bipolar and unipolar switching. In the former type of switching, the set process (Transition from High resistance state to Low resistance state) and Reset process (Transition from Low resistance state to High resistance state) takes place at different polarities (**figure 1.4a**). While in the latter the set and reset happens at the same polarity (**figure 1.4b**), that is either they can happen in the positive or in the negative cycle. ECM mechanism which is cation assisted and VCM which is anion assisted switching process generally exhibits bipolar switching behaviour, whereas TCM which can be both cation and anion assisted exhibits unipolar switching process [**34**]. While performing electrical measurements compliance current (CC) is set in order to ensure the safe operation of the device. The compliance level is set usually during the set operation. This ensures that the device current does not exceed the compliance level. Many studies have shown the importance of compliance on the switching behaviour of RSDs [**38-40**].

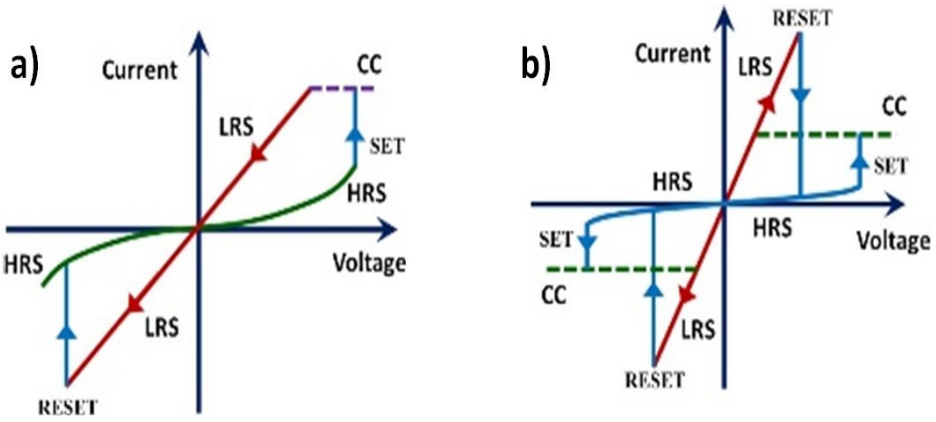

Figure 1.4: Types of resistive switching. a) Bipolar Switching. b) Unipolar Switching **[37].**

1.4.2 Types of resistive switching devices

RSDs are classified into organic, inorganic and hybrid, according to the nature of the active layer that is present between the two electrodes or leads.

Inorganic RSDs represent the most widely studied case due to their simpler switching matrix compared to organic and hybrid RSDs [**41-45**]. Thin film based RSDs are good examples of inorganic RSDs, where a careful control of the active material thickness allows to electrically tune certain properties and to modulate the current flowing perpendicularly to the same film [**46**]. The technologies used for thin film deposition is more matured, controllable and widespread and thus inorganic RSDs are more probable to hit the market at the first place. Nanocomposite (NC) RSDs, alternatively known as hybrid, features a matrix and an active filler that do not share the same electronic behavior. NC RSDs are normally characterized by a passive matrix containing dispersed active fillers in the form of clusters or nanoparticles (NPs), which can be electrically activated and can also produce current modulation [**47-51**]. Extensive research and studies were conducted on RSDs based on different switching matrices, each of which has its unique properties. Organic RSDs exploit the intrinsic properties of organic materials, including processability, low cost, good retention time, high endurance and mechanical flexibility, when coupled with polymeric or natural flexible substrates [**52-57**]. In the present thesis, main focus is given to RSDs based on polymers and Nano Composites (NC) or in other words Hybrid RSD.

1.4.2.1 Hybrid (Organo-metallic) RSD

Hybrid nanomaterials gained widespread interest due to their novel properties in various fields of science including optoelectronics, anti-bacterial, medicine, environment applications etc [**58-62**]. Nanometer-sized materials feature quantum confinement of charge carriers and often result in amazing properties that could be exploited to realize electronic devices enhanced with innovative functionalities [**63, 64**]. NCs can be easily prepared by blending polymers with inorganic NPs such as silver, gold etc [**65**]. Such devices offer several potential advantages like reduced cost if compared to batch-processed inorganic materials, ease of additive manufacturing (i.e. printing) over large areas, high throughput processing, light-weight and flexible mechanical properties [**51**]. Nanomaterials used in this field include metallic NPs [**66**] as well as nanotubes, nanowires, nanorods etc [**67,68**].

The resistive switching process happening in these devices are mainly due to 1: formation of metallic filament 2: Interface switching. In the former, which is a common mode of switching in hybrid memristors [**69-73**] a metallic conductive filament is formed between the two terminals. In filamentary resistive switching, current in LRS flows through the confined local path in the insulating matrix while current in HRS flows through the films homogeneously. Although the filamentary conducting path has been presented in many systems, the composition of filaments vary from case to case. In case of devices with inert electrodes, the

switching is activated once the nanoparticle film exhibits controllable resistive switching that depends on the operational parameters including the applied bias, temperature, and sweep frequency. The film's resistance behaviour is explained due to the formation and rupturing of nano filament caused mainly because of electro migration effect which is the transport of the material due to the gradual movement of ions, which in turn is due to a transfer of the momentum between the electrons and the diffusing metal atoms [**69, 74**]. Sandouk et al. [**69**] has explained an RSD based on inert electrodes, where the nanofilament formation and destruction has been explained by means of electromigration effect. R. M. Mutiso et al. [**33**] has described the resistive switching mechanism in a Silver/Polystyrene/Silver nano gap device. They observed a switching due to metallic filament formation. Here they used Polystyrene as the polymer composite in which silver (Ag) nanowires were dispersed. By an increase in the applied field, the resistance switching took place in the device near percolation threshold. The mechanism behind this resistance switching was explained by means of field induced formation of Ag filaments which bridge adjacent nanowire clusters. Similar explanation of resistive switching was also given by Rajan et al. [**39,40**] where the switching was explained by means of field induced filamentary formation. **Figure 1.5** provides a schematic representation of the field induced filament formation in a nanoparticle incorporated polymer composite.

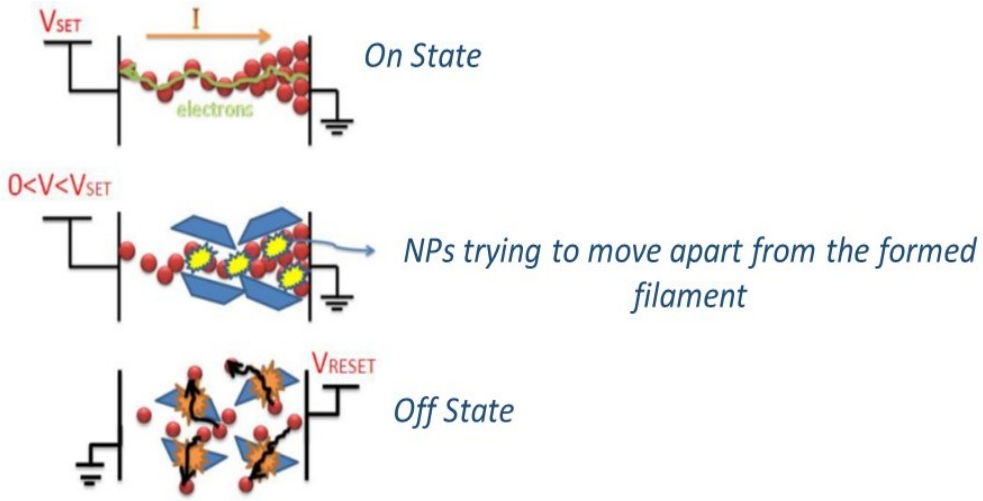

Figure 1.5: Pictorial representation of field induced metallic filament formation in a hybrid RSD.

Suppose that we have our polymeric matrix and we have some metallic NPs/clusters dispersed in it. These clusters could actually exist both as neutral or

ionized clusters. Once we apply a bias to the electrodes, and as the voltage reach their threshold value, the metallic NPs or ions will gain enough driving force as they get charged in order to move. Then they move randomly in the polymer matrix and a connection is formed between these particles. This metallic filament allows the electrons to move freely through this and thus causing the device to switch on. As the voltage or field decreases the ions or NPs may experience a small repulsion from the formed filament but this filament still remains due to the polymer matrix hindrance. Once the voltage reduces and reaches reset threshold, we have a complete rupturing of the formed filament due to the movement of the metallic NPs and ions from the formed filament which leads to the Off state of the device.

Electrochemical metallization memory (ECM) devices are now gaining very much research interest. These are the most commonly seen devices which exhibit filamentary conduction [**71**]. The conduction mechanism happening in these devices is a little different. In ECM cells, the filament is mediated by a REDOX reaction. ECM cells usually consist of an active and a passive electrode. Electro Chemical Metallization (ECM) memories feature a filament composed of reduced metal (produced by migration of the metallic electrodes) through the polymeric matrix, taking advantage of a fast read/write/erase process and a long retention period [**75, 76**]. Usually, the layout of RSDs consists of a stacked structure in which the intermediate layer is composed of a very thin film (≈100 nm or less) of polymeric material. Active electrodes or polymers containing metal ions that can be reduced by an applied voltage are used in order to create the conductive filament across the polymer. The presence of polar atoms (e.g. oxygen or fluorine) in the polymeric chain that can coordinate metal ions, regardless of their position (side or principal chain), is essential for the production of metal filaments [**53**]. **Figure 1.6** provides a schematic representation of the formation and dissolution of conductive filament in an ECM. When an active bias (positive) is provided to the active electrode (Ag, Cu, Ni etc), the metal oxidizes and the formed cations migrate through the solid electrolyte towards the electrochemically inert electrode (Au, Pt etc) where they are reduced by the electrons flowing from the cathode. This process is represented in **figure 1.6a**. The precipitation of the active metals at the cathode leads to the growth of metal protrusion which reaches the anode to form a highly conductive filament. This step is shown in **figure 1.6b**. Finally when a negative bias is provided to the active electrode, the electrochemical dissolution of the conductive filament takes place which is usually at the tip of the filament protruding towards the active electrode (**Figure 1.6c**).

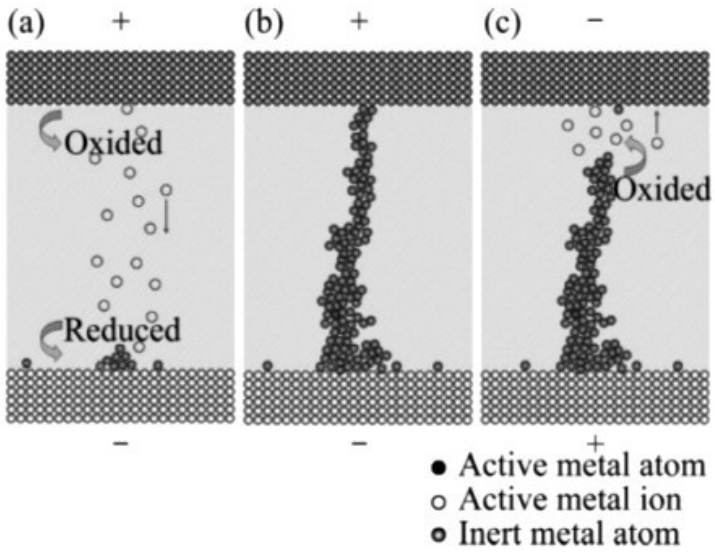

Figure 1.6: Pictorial representation of resistive switching mechanism in ECM. a) Electrochemically active metal ions migrating to cathode. b) Precipitation of active metal atoms at the electrochmically inert electrode and forms a conducting filament. c) Electrochemical dissolution of the filament with change in applied polarity **[77].**

ECM memories can be regarded as the next generation memory devices, due to the possibility of scaling down almost to the atomic level. One of the most peculiar feature of filament type resistive switching is that the switching does not depend on the device area [**78**].

In interface type switching, the conduction depends on the barrier height at the interface of the active switching layer and the electrode. This interface barrier can be modulated by applied electrical stimuli [**77**]. Lin et al. has described well the interface type switching where Gold nanoparticles are embedded in Polystyrene [**79**]. The current transition happening in this device is explained by means of trap filled space charge limited current model (SCLC). The SCLC occurs when the number of acceptor levels is smaller when compared to the injected charge concentration. This forms a space charge cloud near the electrode [**80**]. In SCLC model the current V/s voltage curve will have mainly 4 regions which explains the entire switching process. At lower voltages the current increases linearly as the bias voltage is increased. This region is known as the Ohmic region, where the device behaves as an ideal resistor. Afterwards, current shows a voltage square dependence. This region where the current shows a voltage square dependence is the SCLC. This occurs when the equilibrium charge

concentration (before charge injection) is negligible compared to the injected charge concentration. This forms a space charge cloud near the injecting electrode. As bias increases the traps gets filled and above a certain limit known as the trap-free voltage limit (V_{TFL}) the device enters the trap free SCLC. The four states mentioned can be simplified into 4 equations as:

Ohmic:

$$J \sim \mu V \tag{1.13}$$

Space-Charge Limited Current (SCLC):

$$J \sim \mu V^2 \tag{1.14}$$

Trap-Free Voltage Limited (V_{TFL}):

$$V_{TFL} \sim d^2 N_t \tag{1.15}$$

Trap-Free SCLC:

$$J \sim \mu V^2 \tag{1.16}$$

Where J is the current density, V is the applied voltage, μ is the carrier mobility charge, d is the distance between the electrodes and N_t is the concentration of trapped charges. **Figure 1.7** provides the Current V/S Voltage plot which provides all the four states mentioned in the SCLC model.

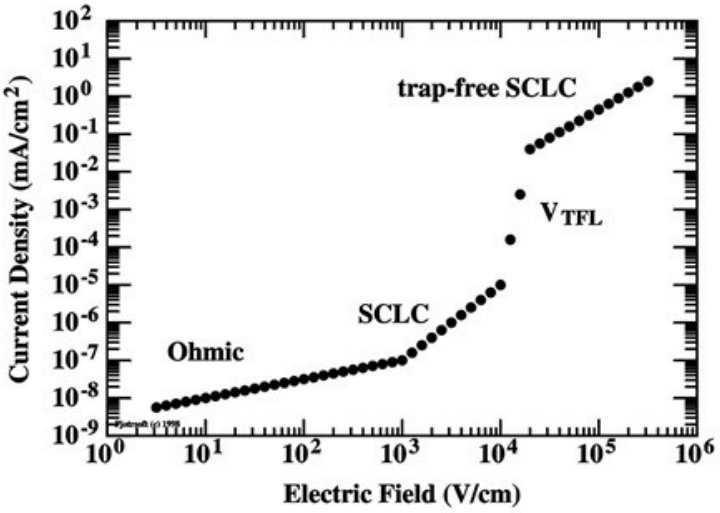

Figure 1.7: Four regions in the Current v/s Voltage plot **[80]**.

1.5 Applications

Memristor has the ability to enhance several areas of Integrated Circuit design and computing [**11**]. One of the most widespread area where memristors are being applied is in the field of Non Volatile memory devices. Other widely studied area is in the field of neuromorphic computing where memristors are presently used to emulate a neural synapse. In the following subsections we will see how a memristor can be used in memory devices and how they can function as an artificial neural synapse, hopefully allowing us to emulate a human brain.

1.5.1 Memory Devices

As discussed previously, the semiconductor industry has drastically increased the number of components per chip according to Moore's law. Further advances have also been achieved through various other technologies in electronic systems that adds extra functionalities [**81**]. In order to make progress in the semiconductor industry in the same rate, further miniaturization is needed. There are several alternate technologies which have been put forward. Memristors and Resistive random access memory (RRAM) are the frontrunners among all. Considering a feasible application for memristors, the first suggestion would be in memory devices because of their small feature size and this in turn could offer an increase in memory density, requiring less power.

In the present market there are mainly three types of memories: Dynamic Random Access Memory (DRAM) which is the fastest and consumes energy during refreshing cycles. Flash Memory or simply Flash which is nonvolatile but with low cyclic endurance. And finally the Hard Disk Drives which has a really high data storage capacity but slow access times and consumes large amount of power. Imagine to have a single device which has the benefits of all the above mentioned individual devices but none of the drawbacks [**82**]. Memristors or RSDs are strongly considered to be the replacement for the above technologies. Thanks to the two terminal nature of these devices, they can be easily integrated onto crossbar architecture that has the ability for heavy data storage. Presently, RSDs or Memristors have been developed with ultra-high switching speed (~10 ns) and long retention time with large number of write-read-erase-write cycles [**83-87**].

There has been many ways proposed for reading and writing data using memristor circuits [**88-90**]. Here a novel nondestructive read/write circuit composed of memristors explained by M. Elshamy et al [**88**] has been shown

(**Figure 1.8**). This particular read/Write circuit exhibits faster access time, less power consumption and a high storage density.

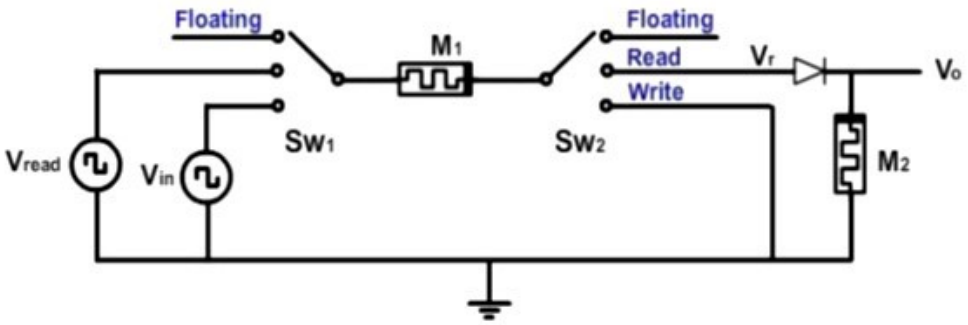

Figure 1.8: Read/Write circuit for a memrsitor based memory **[88].**

In this simple memristor based circuit, only two logic levels, 0 and 1 can be stored. The write process can be implemented by connecting Switch 1(SW1) to input voltage (V_{in}) and SW2 to ground. The applied voltage magnitude and pulse duration should be selected to have an acceptable writing speed with minimum power consumption. In the case of read operation, the read voltage can actually disturb the stored data due to the accumulative property of memristors. In reading process, initially SW1 is connected to read voltage and SW2 to the diode (**Figure 1.8**). To read the stored data, the read voltage (V_{read}) is applied for a certain pulse duration (T_{read}). In reading process we have 2 scenarios: One in which the read data is "1" and the other when its "0". In the former case when the read data is 1, memristor M1 will be in its On state, and voltage drop across it will be low. This makes V_r equal to V_{read}. Memristor M2 is the load resistor and the output voltage across M2 indicates the data that is stored in M1. Voltage drop across M2 is given by the below expression.

$$V_0 = V_r - n \times V_T \times \ln\left(\frac{I_d}{I_{sat}}\right) \qquad (1.17)$$

Where I_d is the diode On current, I_{sat} is the diode saturation current, n is the ideality factor and V_T is the thermal voltage (26 mV at room temperature). Thus in the case when "1" is read, the voltage drop across M2 is $V_0 = V_H$. V_H is designed as high as possible compared to V_L. In the second case when the read data is "0", M1 is at Off state and this results in a high voltage drop across it which makes the diode Off and thus the output voltage V_O is V_L. The other extended range of application as well as qualities when compared to current memory is that they have the ability of being optically transparent and physically

flexible [**91-93**]. While using memristors for creating large crossbar arrays for potential memory applications, sneak path current is a major issue. This is a major problem in crossbar arrays that effects the reliable reading of data from individual memory cells and increases power consumption [**94**]. By using selector devices along with transistors or memristors, the problem of sneak path current can be mitigated. Usually selector devices are tunneling diodes, threshold switches, bidirectional varistors etc. Among these a simple two terminal volatile or otherwise threshold memristor or RSD can act as a very good selector device which can mitigate the issue of sneak path current without compromising the scalability and 3D stacking capability of memristor. The key requirements for selector devices are: high selectivity (High On to Off ratio between the current at a particular voltage), steep turn on slope, high current density, fast turn On and Off and high endurance. Many research teams are now working on selector devices incorporated in high density memory arrays [**95-98**].

1.5.2 The artificial synapse

Memristors have been experimentally proven to be similar to our synapse. This is a great step towards building neuromorphic chips using memristors. Finally they can be used to emulate a working human brain, which is indeed a very challenging result.

There have been so many studies going on in the direction of memristors emulating a biological synapse [**96, 99-101**]. Neurons consist of axons and dendrites and each neuron is interconnected with junctions know as synapses. Axons and dendrites are responsible for transmitting information while the synapse controls the signals [**102**]. Synapses are junctions between the neurons where the presynaptic terminal of one cell comes into contact with the postsynaptic membrane of another. The neurons are excited at these junctions. There are mainly two types of synapses: Electrical and Chemical synapse. Electrical synapses occur when the pre synapse is in electrical continuity with the post synapse. Here the electrical changes in one cell are transmitted instantaneously to the next. Chemical synaptic junctions are much more complicated. In this case, the gap between the pre and post synaptic terminal is larger and the information is carried by neuroactive substances released at the presynaptic side of the junction. Spike-Time-Dependent-Plasticity (STDP) is known as one of the fundamental rules of learning and memory in the brain, which can explain how synapse can adapt to the surrounding environment. Memristor based models can emulate the STDP in neuronal communication [**103, 10**]. The STDP rule is one of the fundamental rules of learning and memory in the

brain which actually explains how the synapse adapts to the surrounding [**104**]. Recently J.Yang et al [**96**] has come up with a diffusive memristive device which can mimic a real synapse. This could actually be used as a key element in next generation computers that can emulate the human brain.

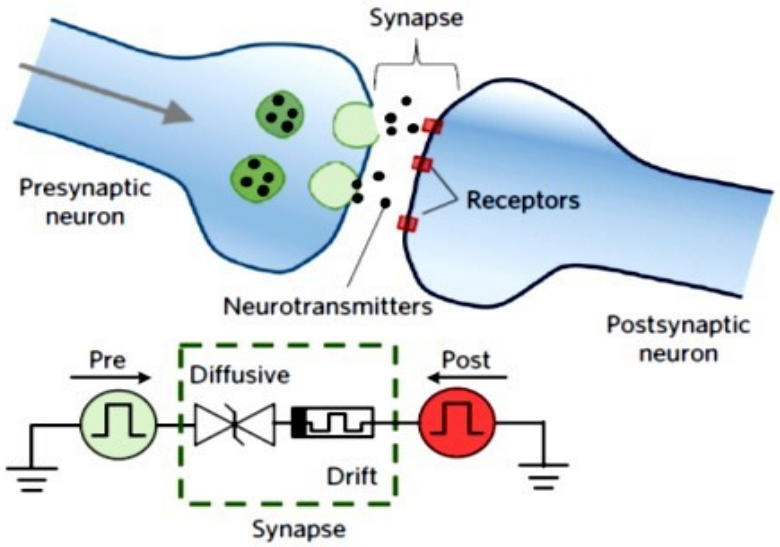

Figure 1.9: Memristor based circuit mimicking biological synapse **[96].**

Figure 1.9 provides the combined circuit element that Yang's team has come up with. The circuit shows the combination of a diffusive as well as a drift memristor which is connected to a voltage source. This set up is very similar to a biological synapse which is connected to a pre and post synaptic neuron. The circuit set up was able to emulate multiple synaptic functions. To realize all these benefits of memristive devices, they have to be implemented in a crossbar array architecture which provides high density, random access and large connectivity. There are several teams working on the cross bar architecture as well as 3D stacking of these devices [**105, 106**].

1.6 State Of The Art

As mentioned in the beginning of the thesis, even though the concept of memristor was mathematically postulated during 1971, it got its due attention only in 2008 when HP came up with the first implementation of a memristor. Since the Silicon era is almost approaching its end, memristors are believed to take over the electrical circuits and change electronics forever.

The research taking place in this field is huge and rapid and extremely competitive. Every day the field of memristors or RSDs come up with modified design or devices based on optimized technology or mind blowing characteristics. The field of memristors is not just something which is confined in the field of memory devices. The main anticipated application of which is in the field of neuromorphic applications. RSDs could potentially replace integrated electronic devices for advanced computing and digital and analog circuit applications including neuromorphic networks [**107**].

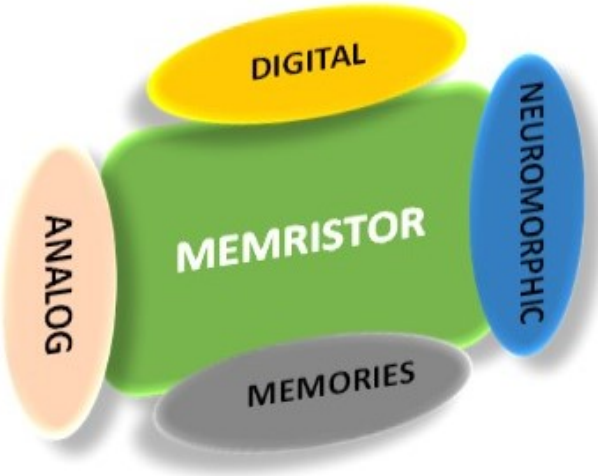

Figure 1.10: Potential fields of applications of memristive devices

As mentioned earlier the first and fastest developing practical application of memristors is in the field of nonvolatile memory for computing. **Table 1.2** provides the features of already existing memory devices and the memristor based device features. Memristors can be used in analog applications such as programmable analog circuits, oscillators, analog filters etc [**108, 109**]. Memristors can be used in digital logic applications such as in memory computing [**110**]. Field Programmable gate array is one of the fastest and promising claim of memristors in the field of digital application [**111**]. Even before the finding of memristors, scientists have been trying to come up with brain like systems which can function as close as human brains. But building a brain like massive parallel system was always challenging due to the lack of devices which can emulate the neural synapse [**112**].

Table 1.2: Specifications of already available commercial memory technologies v/s Memristor device [**107**]

	Available commercial Technologies				**Transpiring Technology**
	DRAM	**Flash (NAND)**	**Flash (NOR)**	**SRAM**	**Memristor**
Cell Density (F^2)	6-30	1-4	1-10	140	4
Retention Time	> 64 ms	> 10 years	> 10 years	As long as voltage is applied	> 10 years
Endurance	$> 10^{16}$ cycles	$> 10^5$ cycles	10^5 cycles	$> 10^{16}$ cycles	$> 10^{12}$ cycles
Read Time	2 ns	0.1 ms	15 ns	0.1 to 0.3 ns	< 2 ns
Feature Size	36 nm	16 nm	45 nm	45 nm	< 5 nm

Promising experimental demonstrations of transistor free memristor based circuits are being carried out which can emulate human neural synapse and is also a great step towards complex memristive neuromorphic networks which can finally emulate a human brain [**96, 113**].

1.7 References

1. Moore, G.E. (1965). Cramming more components onto Integrated Circuits. *Electronics*, 38, pages 114-117.

2. Burr G.W. (2008). Overview of candidate device technologies for storage-class memory. *IBM Journal of Research and Development*, 52, pages 449-464.

3. International technology roadmap for semiconductors. ITRS 2006.

4. Ishiwara. H. (2012). Ferroelectric random access memories. *Journal of Nanoscience and Nan technology*, 12, pages 7619-7627.

5. Tehrani, S.; Slaughter, J. M.; Deherrera, M.; Engel, B. N.; Rizzo, N. D.; Salter, J.; Durlam, M.; Dave, R. W.; Janesjy, J.; Butcher, B.; Smith, K.; Grynkewich, G. (2003). Magnetoresistive random access memory using magnetic tunnel junctions. *Proceedings of the IEEE*, 91, pages 703-714.

6. Raoux, S.; Burr, G. W.; Breitwisch, M. J.; Rettner, C. T.; Chen, Y. C.; Shelby, R. M.; Salinga, M.; Krebs, D.; Chen, S. H.; Lung, H. L.; Lam, C. H. (2010). Phase-change random access memory: A scalable technology. *IBM Journal of Research and Development,* 52, pages 465-479.

7. Pan, F.; Gao, S.; Chen, C.; Song, C.; Zeng, F. (2014). Recent progress in resistive random access memories: materials, switching mechanisms, and performance. *Materials Science and Engineering.* 83, *R*, pages 1-59.

8. Chua, L. (1971). Memristor, the missing circuit element. *IEEE Transcations on Circuit Theory*, 18, pages 507-519.

9. Strukov, D. B.; Snider, G. S.; Stewart, D. R.; Williams, R. S. (2008). The missing memristor found. *Nature*, 453, pages 80-83.

10. Chua, L. (2011). Resistance swtching memories are memristors. *Applied. Physics. A*, 102, pages 765-783.

11. Marani, R.; Gelao, G.; Perri, A. G. (2015). A review on memrsitor applications. arXiv:1506.06899, 2015arXiv150606899M.

12. Waser, R.; Aono, M. (2007). Nanoionics-based resistive switching meories. *Nature Materials*, 6, pages 833-840.

13. Kwon, D. H.; Kim, K. M.; Jang, J. H.; Jeon, J. M.; Lee, M. H.; Kim, G. H.; Li, X. S.; Park, G. S.; Lee, B.; Han, S.; Kim, M.; Hwang, C. S. (2010). Atomic structure of conducting nanofilaments in TiO_2 resistive switching memory. *Nature Nanotechnology*, 5, pages 148-153.

14. Ronald Naber, C. G.; Asadi, K.; Blom, W. M.; Leeuw, D. M.; Boer, B. (2010). Organic non-volatile memory devices based on ferroelectricity. *Advanced Materials*, 22, pages 933-945.

15. Ma, L. P.; Liu, J.; Yang, Y. (2002). Organic electrical bistable devices and rewritable memory cells. *Applied Physics Letter*, 80, pages 2997-2999.

16. Yang, Y.; Lu, W. (2013). Nanoscale resistive switching devices: mechanisms and modelling. *Nanoscale*, 5, pages 10076-10092.

17. Zhou, C.; Newns, D. M.; Misewich, J. A.; Pattnaik, P. C. (1997). A field effect transistor based on the mott transition in a molecular layer. *Applied Physics Letter*, 70, pages 598-600.

18. Roβberg, K.; Paasch, G.; Dunsch, L.; Ludwig, S. (1998). The influence of porosity and the nature of the charge storage capacitance on the impedance behaviour of electropolymerized polyaniline films. *Journal of Electroanalytical Chemistry*, 443, pages 49-62.

19. Erokhin, V.; Berzina, T.; Fontana, M.P. (2005). Hybrid electronic device based on polyaniline-polyethyleneoxide junction. *Journal of Applied Physics*, 97, 064501.

20. Son, J. Y.; Shin, Y. H. (2008). Direct observation of conducting filaments on resistive switching of NiO thin films. *Applied Physics Letter,* 92, pages 222106–222103.

21. Liu, Q.; Sun, J.; Lv, H.; Long, S.; Yin, K.; Wan, N.; Li, Y.; Sun, L.; Liu, M. (2012). Resistive Switching: Real-Time Observation on Dynamic Growth/ Dissolution of Conductive Filaments in Oxide-Electrolyte-Based ReRAM. *Advanced Materials,* 24, pages 1844-1849.

22. Zhu, X.; Su, W.; Liu, Y.; Hu, B.; Pan, L.; Lu, W.; Zhang, J.; Li, R. W. (2012). Resistive Switching Memories: Observation of Conductance Quantization in Oxide-Based Resistive Switching Memory. *Advanced Materials,* 24, pages 3941-3946.

23. Jeong, D. S.; Schroeder, H.; Waser, R. (2006). Impedance spectroscopy of TiO2 thin films showing resistive switching. *Applied Physics Letter*, 89, pages 082909-082911.

24. Sullaphen, J.; Bogle, K.; Cheng, X.; Gregg, J. M.; Valanoor, N. (2012). Interface mediated resistive switching in epitaxial NiO nanostructures. *Applied Physics Letter*, 100, pages 203115-203119.

25. Janousch, M.; Meijer, G. I.; Staub, U.; Delley, B.; Karg, S. F.; Andreasson, B. P. (2007). Role of Oxygen Vacancies in Cr-Doped SrTiO3 for Resistance Change Memory. *Advanced Materials*, 19, pages 2232-2235.

26. Li, M.; Zhunge, F.; Zhu, X.; Yin, K.; Wang, J.; Liu, Y.; He, C.; Chen, B.; Li, R. W. (2010). Nonvolatile resistive switching in metal/La-doped BiFeO3/Pt sandwiches. *Nanotechnology*. 21, 425202.

27. Sawa, A.; Fujii, T.; Kawasaki, M.; Tokura, Y. (2004). Hysteretic current--voltage characteristics and resistance switching at a rectifying Ti/Pr0.7Ca0.3MnO3 interface. *Applied Physics Letter*, 85, 4073-4075.

28. Shuai, Y.; Ou, X.; Luo, W.; Mucklich, A.; Burger, D.; Zhou, S.; Wu, C.; Chen, Y.; Zhang, W.; Helm, M.; Mikolajick, T.; Schmidt, O. G.; Schmidt, H. (2013) Key concepts behind forming-free resistive switching incorporated with rectifying transport properties. *Scientific Reports,* 3, 2208, pages 1-6.

29. Pender, L. F.; Fleming, R. J. (1975). Memory switching in glow discharge polymerized thin films. *Journal of Applied Physics*, 46, 3426.

30. Lai, Y. C.; Wang, D. Y.; Huang, I. S.; Chen, Y. T.; Hsu, Y. H.; Lin, T. Y.; Meng, H. F.; Chang, T. C.; Yang, Y. J.; Chen, C. C.; Hsu, F. C.; Chen, Y. F. (2013). Low operation voltage macromolecular composite memory assisted by graphenenanoflakes. *Journal of Material Chemistry C*, 1, pages 552-559.

31. Joo, W. J.; Choi, T. L.; Lee, J.; Lee, S. K.; Jung, M. S.; Kim, N.; Kim, J. M. (2006). Metal Filament Growth in Electrically Conductive Polymers for Nonvolatile Memory Application. *Journal of Physical Chemistry B*, 110, pages 23812-23816.

32. Joo, W. J.; Choi, T. L.; Lee, K. H.; Chung, Y. (2007). Study on Threshold Behavior of Operation Voltage in Metal Filament-Based Polymer Memory. *Journal of Physical Chemistry B,* 111, pages 7756-7760.

33. Mutiso, R. M.; Kikkawa, J. M.; Winey, K. I. (2013). Resistive switching in silver/Polystyrene/silver nano-gap devices. *Applied Physics Letter*, 103, 223302.

34. Lim, E. W.; Ismail, R. (2015). Conduction mechanism of Valence change resistive switching memory: A survey. *Electronics*, 4, pages 586-613.

35. Waser, R. (2012). Redox-based resistive switching memories. Journal of Nanoscience and Nanotechnology, 12, pages 7628-7640.

36. Chiolerio, A.; Roppolo, I.; Bejtka, K.; Asvarov, A.; Pirri, C. F. (2016). Resistive hysteresis in flexible nanocomposites and colloidal suspensions: interfacial coupling mechanism unveiled. RSC Advances, 6, pages 56661-56667.

37. Prakash, A.; Jana, D.; Maikap, S. (2013). TaOx-based resistive switching memories: prospective and challenges. *Nanoscale Research Letters*, 8, pages 1-17.

38. Cao, X.; Li, X. M.; Gao, X. D.; Zhang, Y. W.; Liu, X. J.; Wang, Q.; Chen, L. D. (2009). Effects of the compliance current on the resistive switching behaviour of TiO_2 thin films. *Applied Physics A*, 97, pages 883-887.

39. Rajan, K.; Bocchini, S.; Chiappone, A.; Roppolo, I.; Perrone, D.; Bejtka, K.; Ricciardi, C.; Pirri, C. F.; Chiolerio, A. (2017). Spin-coated silver nanocomposite resistive switching devices. *Microelectronic Engineering*, 168, pages 27-31.

40. Rajan, K.; Chiappone, A.; Perrone, D.; Bocchini, S.; Roppolo, I.; Bejtka, K.; CAstellino, M.; Pirri, C. F.; Ricciardi, C.; Chiolerio, A. (2016). Ionic

liquid-enhanced soft resistive switching devices. *RSC Advances*, 6, pages 94128-94138.

41. Sun, H.; Liu, Q.; Li. C.; Long, S.; Lv. H.; Bi, C.; Huo, Z.; Li, L.; Liu, M. (2014). Direct observation of conversion between threshold switching and memory switching induced by conductive filament morphology. *Advanced Functional Materials*, 24, pages 5679-5686.

42. Choi, B. J.; Torrezan, A. C.; Strachan, J. P.; Kotula, P. G.; Lohn, A. J.; Marinella, J. M.; Li, Z.; Williams, R. S.; Yang, J. J. (2016). High-speed low -energy nitride memristors. *Advanced Functional Materials*, 26, pages 5290-5296.

43. Muenstermann, R.; Menke, T.; Dittmann, R.; Wasrer, R. (2010). Coexistance of filamentary and homogeneous resistive switching in Fe-doped $SrTiO_3$ thin film memristive devices. *Advanced Materials*, 22, pages 4819-4822.

44. Huang, C. H.; Huang, J. S.; Lin, S. M.; Chang, W. Y.; He, J. H.; Y. L. (2012). ZnO_{1-x} nanorod arrays/ZnO thin film bilayer structure: from homojunction diode and high performance memristor to complementary 1D1R application. *ACS.Nano*, 6, pages 8407-8414.

45. Dongale, T. D.; Shinde, S. S.; Kamat, R. K.; Rajpure K. Y. (2014). Nanostructured TiO_2 thin film memristor using hydrothermal process. *Journal of Alloys and Compounds*, 593, pages 267-270.

46. Simmons, J. G.; Verderber, R. R. (1967). New conduction and reversible memory phenomena in thin insulating films. *Proceedings of the Royal Society of London A*, 301, pages 77-102.

47. Nawrocki, R. A.; Voyles, R. M.; Shaheen, S. E. (2012). Polymer and Nanoparticle-Composite Bistable Devices: Physics of Operation and Initial Applications. (p. 291-314). Springer Netherlands.

48. Jin, Z.; Chen, Y.; Zhou, Q.; Mao, P.; Liu, H.; Wang, J.; Li, Y. (2017). Graphdiyne for multilevel flexible organic resistive random access memory devices. *Materials Chemistry Frontiers*, 1, pages 1338-1341.

49. Sharma, B.; Rabinal, M. K. (2015). Aluminium oxide-silver nanoparticle interfaces for memristive applications. *IOSR.Journal of Electrical and Electronics Engineering*, 10, pages 62-67.

50. White, S. I.; Vora, P. M.; Kikkawa, J. M.; Winey, K. I. (2011). Resistive switching in bulk silver nanowire-polystyrene composites. *Advanced Funtional Materials*, 21, pages 233-240.

51. Mukherjee, B.; Mukherjee, M. (2009). Nonvolatile memory device based on Ag nanoparticle: characterestics improvement. 94, *Applied Physics Letter*, 173510.

52. Ji, Y.; Cho, B.; Song, S.; Choe, M.; Kim, T. W.; Kim, J. S.; Choy, B. S.; Lee, T. (2011). Unipolar bistable switching of organic non-volatile memory devices with Poly (styrene-co-styrenesulfonic acid Na). *Journal of Nanoscience and Nanotechnology*, 11, pages 1385-1388.

53. Lin, W. P.; Liu, S. J.; Gong, T.; Zhao, Q.; Huang, W. (2014). Polymer based resistive memory materials and devices. *Advanced Materials*, 26, pages 570-606.

54. Chu, C. W.; Ouyang, J.; Tseng, J. H.; Yang, Y. (2005). Organic donor acceptor system exhibiting electrical bistability for use in memory devices. *Advanced Materials*, 17, pages 1440-1443.

55. Cho, B.; Kim, T. W.; Song, S.; Ji, Y.; Jo, M.; Hwang, H.; Jung, G. Y.; Lee, T. (2010). Rewritable switching of one diode-one resistor non-volatile organic memory devices. *Advanced Materials*, 22, pages 1228-1232.

56. Yang, Y.; Ouyang, J.; Ma, L.; Tseng, R. J. H.; Chu, C. W. (2006). Electrical switching and bistability in organic/polymeric thin films and memory devices. Advanced Functional Materials, 16, pages 1001-1014.

57. Ling, Q. D.; Liaw, D. J.; Zhu, C.; Chan, D. S. H.; Kang, E. T.; Neoh, K. G. (2008). Polymer electronic memories: materials, devices and mechanisms. *Progress in Polymer Science*, 33, pages 917-978.

58. Sureshkumar, M.; Siswanto, D. Y.; Lee, C. K. (2010). Magnetic antimicrobial based nanocomposite based on bacterial cellulose and silver nanoparticles. *Journal of Materials Chemistry*, 20, pages 6948-6955.

59. Jain, P. K.: Huang, X.; Sayed, I. H.; Sayed M. A. (2008). Noble metals on the nanoscale: optical and photothermal properties and some applications in imaging, sensing, biology, and medicine. *Accounts of Chemical Research*, 41, pages 1578-1586.

60. Maier, S. A.; Brongersma, M. L.; Kik, P. G.; Meltzer, S.; Requicha, A. A. G. (2001). Plasmonics- A route to nanoscale optical devices. *Advanced Materials*, 13, pages 1501-1505.

61. Jain, S.; Hirst, D. G.; Sullivan, J. M. O. (2012). Gold nanoparticles as novel agents for cancer therapy. *The British Journal of Radiology*, 85, pages 101-13.

62. Khin, M. M.; Nair, A. S.; Babu, V. J.; Murugan, R.; Ramakrishna, S. (2012). A review on nanomaterials for environmental remediation. *Energy and Environmental Science*, 5, pages 8075-8109.

63. Chiolerio, A.; Porro, S.; Bocchini, S. (2016). Impedance hyperbolicity in nkjet printed graphene nanocomposites: Tunable capacitors for advanced devices. *Advanced Electronic Materials*, 2, 1500312.

64. Sangermano, M.; Buzzerio, G.; Rizzoli, R.; Ortolani, L.; Morandi, V.; Pirri, C. F.; Chiolerio, A. (2015). Enhanced performance of graphene-epoxy flexible capacitors by means of ceramic fillers. *Macromolecular Chemistry and Physics*, 216, pages 707-713.

65. Kim, T. W. (2010). Effect of Ag nanoparticles on resistive switching of Polyfluorene based organic non-volatile memory devices. *Journal of the Korean Physical Society*, 56, pages 128-132.

66. Rajan, K.; Roppolo, I.; Chiappone, A.; Bocchini, S.; Perrone, D.; Chiolerio, A. (2016). Silver nanoparticle ink technology: state of the art. *Nanotechnology Science and Applications*, 9, pages 1-13.

67. Hota, M. K.; Bera, M. K.; Kundu, B.; Kjundu, S. C.; Maiti, C. K. (2012). A natural silk fibroin protein-based transparent bio memristor. *Advanced Functional Materials*, 22, pages 4493-4499.

68. Liao, Z. M.; Hou, C.; Zhao, Q.; Wang, D. S; Li, Y. D.; Yu, D. P. (2009). Resistive switching and metallic-filament formation in Ag_2S nanowire transistors. *Small*, 21, pages 2377-2381.

69. Sandouk, E. J.; Gimzewski, J. K.; Steig, A. Z. (2015). Multistate resistive switching in silver nanoparticle films. *Science and Technology of Advanced Materials*, 16, pages 1-7.

70. Yang, Y. C.; Pan, F.; Liu, Q.; Liu, M.; Zeng, F. (2009). Fully room temperature fabricated non-volatile resistive memory for ultrafast and high desity memory applications. *Nano Letters*, 9, pages 1636-1643.

71. Billen, J.; Steudel, S.; Muller, R.; Genoe, J.; Heremans, P. (2007). A comprehensive model for bipolar electrical switching of CuTCNQ memories. *Applied Physics Letter*, 91, 263507.

72. Xu, Z.; Bando, Y.; Wang, W.; Bai, X.; Golberg, D. (2010). Real time in situ HRTEM-resolved switching of Ag2S nanoscale ionic conductor. *ACS Nano*, 4, pages 2515–2522.

73. Gao, S.; Song, C.; Chen, C.; Zeng, F.; Pan, F. (2013). Formation process of conducting filament in planar organic resistive memory. *Applied Physics Letter*, 102, 141606.

74. Breitling H.; Hummel, R. (1972). Electromigration in thin silver, copper, gold, indium, tin, lead and magnesium films. *Journal of Physics and Chemistry of Solids*, 33, pages 845-848.

75. Valov, I.; Waser, R.; Jameson, J. R.; Kozicki, M. N. (2011). Electrochemical metalization memories- Fundamentals, application prospects. *Nanotechology*, 22, 289502.

76. Waser, R.; Dittmann, R.; Staikov, G.; Szot, K. (2009). Redox-based resistive switching memories- nanionic mechanisms, prospects and challenges. *Advanced Materials*, 21, pages 2632–2663.

77. Pan, F.; Chen, C.; Wang, Z. S.; Yang, Y. C.; Yang, J.; Zeng, F. (2010). Nonvolatile resistive switching memories-charactersetics, mechanism and challengs. *Progress in natural science: Materials International*, 20, pages 1-15.

78. Lelmini, D.; Spiga, S.; NArdi, F.; Cagli, C.; Lamperti, A.; Cianci, E.; Fanciulli, M. (2011). Scaling analysis of submicrometer nickel-oxide-based resistive switching memory devices. *Journal of Applied Physics*, 109, 034506.

79. Lin, T. H.; Pei, Z.; Chan, Y. J. (2007). Carrier Transport Mechanism in a Nanoparticle-Incorporated Organic Bistable Memory Device. IEEE Electron Device Letters, 28, pages 569-571.

80. http://www.stallinga.org/ElectricalCharacterization/2terminal/index.html.

81. Gale, E. (2014). TiO2-based memristora and ReRAM: materials, mechanisms and models (a review). *Semiconductor Science and Technology*, 29, 104004.

82. Nawrocki, R. A.; Voyles, R. M.; Shaheen, S. E. (2012). Advances in Neuromorphic Memristor Science and Applications Springer Series in Cognitive and Neural Systems. Springer Series in Cognitive and Neural Systems. (P. 219-314). Springer Netherlands.

83. Kuang, Y.; Huang, R.; Tang, Y.; Ding, W.; Zhang, L.; Wang, Y. (2010). Flexible single component polymer resistive memory for ultrafast and highly compatible nonvolatile memory applications. *IEEE Electron Device Letters*, 31, pages 758-760.

84. Lu, W.; Kim, K. H.; Chang, T.; Gaba, S. (2011). Two terminal resistive switches for memory and logic applications. *IEEE Proceedings of the 16th Asia and South Pacific Design Automation Conference*, pages 217-223.

85. Xia, Q.; Robinett, W.; Cumbie, M. W.; Banerjee, N.; Cardinali, T. J.; Yang, J. J.; Wu, W.; Li, X.; Tong, W. M.; Strukov, D. B.; Snider, G. S.; Ribeiro, G. M.; Williams, R. S. (2009). Memristor-CMOS hybrid integrated circuits for reconfigurable logic. *Nano Letters*, 9, pages 3640-3645.

86. Kim, K. H.; Gaba, S.; Wheeler, D.; Albrecht, J. M. C.; Hussain, T.; Srinivasa, N.; Lu, W. (2012). A functional hybrid memristor crossbar-array/CMOS sustem for data storage and neuromorphic applications. *Nano Letters*, 12, pages 389-395.

87. Prakash, A.; Maikap, S.; Chiu, H. C.; Tien, T. C.; Lai, C. S. (2014). Enhanced resistive swithing memory charaecterstecis and mechansm using a Ti nanolayer at the W/TaO_x interface. Nanoscale Research Letters, 9:125.

88. Elshamy, M.; Mostafa, H.; Ghallab, Y. H.; Said, M. S. (2015). A novel non-destructive read/Write circuit for memristor-based memory arrays. *IEEE Transactions on Very Large Scale Integration (VLSI) Systems*, 23, pages 2548-2656.

89. Ho, Y.; Huang, G. M.; Li, P. (2009). Nonvolatile memristor memory: device characterestics and design implications. IEEE. *ACM International Conference on Computer-Aided Design Digest of Technical Papers,* pages 485-490.

90. Yakopcic, C.; Taha, T. M.; Hasan, R. (2014). Hybrid cross bar architecture for a memristor based memory. *Aerospace and Electronics Conference, NAECON 2014 - IEEE National*, pages 1-5.

91. Bessonov, A. A.; Kirikova, M. N.; Petukhov, D. I.; Allen, M.; Ryhanrn, T.; Bailey, M. A. J. (2015). Layered memristive and memcapcitive switchs for printable electronics. *Nature Materials*, 14, pages 199-204.

92. Yeom, S. W.; Shin, S. C.; Kim, T. Y.; Ha, H. J.; Lee, Y. H.; Shim, J. W.; Ju, B. K. (2016). Transparent resistive switching memory using Aluminium Oxide on a flexible substrate. *Nanotechnology*, 27, 07LT01.

93. Hosseini, N. R.; Lee, J. S. (2015). Biocompatible and flexible chitosan based resistive switching memory with magnesium electrodes. *Advanced Functional Materials*, 25, pages 5586-5592.

94. http://eecatalog.com/chipdesign/2014/12/15/%E2%80%9Csneak-path%E2%80%9D-breakthrough-heralds-arrival-of-ultra-high-density-resistive-memory/

95. Midya, R.; Wang, Z.; Zhang, J.; Savelev, S. E.; Li, C.; Rao, M.; Jang, M. H.; Joshi, S.; Jiang, H.; Lin, P.; Norris, K.; Ge, N.; Wu, Q.; Barnell, M.; Li, Z.; Xin, H. L.; Williams, R. S.; Xia, Q.; Yang, J. J. (2017). Anatomy of Ag/Hafnia based selectors with 10^{10} nonlinearity. *Advanced Materials*, 29, 1604457.

96. Wang, Z.; Joshi, S.; Savelev, S. E.; Jiang, H.; Midya, R.; Lin, P.; Hu, M.; Ge, N.; Strachan, J. P.; Li, Z.; Wu, Q.; Barnell, M.; Li, G. L.; Xin, H. L.; Williams, S. R.; Xia, Q.; Yang, J. J. (2017). Memristors with difusive dynamics as synaptic emulators for neuromrphic computing. *Nature Materials*, 16, pages 101-108.

97. Song, J.; Woo, J.; Prakash, A.; Lee, D.; Hwang, H. (2015). Threshold selector with high selectivity and steep slope for crosspoint memory array. *IEEE Electron Device Letters*, 36, pages 681-683.

98. Hurk, J. V.; Linn, E.; Zhang, H.; Waser, R.; Valov, I. (2014). Volatile resistance states in electochemical metallization cells enabling non-destructive readout of complementary resistive switches. *Nanotechnology*, 25, pages 1-6.

99. Mandal, S.; Amin, A.; Alexander, K.; Rajendran, B.; Jha, R. (2014). Novel synaptic memory device for neuromorphic computing. *Scientific Reports*, 4, 5333: 1-10.

100. Li, Y.; Zhong, Y.; Xu, L.; Zhang, J.; Xu, X.; Sun, H.; Miao, X. (2013). Ultrafast synaptic events in a chalcogenide memristor. Sci.Rep. 3, 2013, 1-7.

101. Lin Y. P.; Bennett, C. H.; Cabaret, T.; Vodenicarevic, D.; Chabi, D.; Querlioz, D.; Jousselme, B.; Derycke, V.; Lkein, J. O. (2016). Physical realization of a supervised learning system built with organic memristive synapses. *Scientific Reports,* 6, 31932.

102. http://www.cerebromente.org.br/n07/fundamentos/neuron/parts_i.htm

103. Chua, L. O. (1976). Memristive devices and systems. *Proceeding of the IEEE*, 64, pages 209-223.

104. Cai, W. (2014). Synapse as a Memristor. Memristor Networks. (P. 113-128). New York Dordrecht London Springer.

105. Linn, E.; Rosezin, R.; Kugeler, C.; Waser, R. (2010). Complementary resistive switches for passive nanocrossbar memories. *Nature Materials*, 9, pages 403-406.

106. Yu, S.; Liang, J.; Wu, Y.; Wong, H. S. P. (2010). Read/write scheme analysis for novel complementary resistive switches in passive crossbar memory arrays. *Nanotechnology*, 21, 465202.

107. Mohammad, B.; Jaoude, M. A.; Kumar, V.; Homouz, D. M.; NAhla, H. A.; Qutayri, M.; Christoforou, N. (2015). State of the art of metal oxide memristive devices. *Nanotechnology Reviews*, 5, https://doi.org/10.1515/ntrev-2015-0029.

108. Eshranghian, K.; Kavehei, O.; Cho, K. R.; Chappell, J. M.; Iqbal, A.; Sarawi, S: F.; Abbott, D. (2012). Memristive device fundamentals and modelling: applications to circuits and systems simulation. *Proceedings of the IEEE*, 100, pages 1991-2007.

109. Kavehei, O.; Cho, K. R.; Lee, S. J.; Abbott, D. (2013). Integrated memristor-mos (M2) sensor for basic pattern matching applications. *Journal of Nanoscience and Nanotechnology*, 13, pages 3638-3640.

110. Hamdioui, S.; Xie, L.; Nguyen, H. A.; Taouil, M.; Bertels, K.; Corporaal, H.; Jiao, H.; Catthoor, F.; Wouters, D.; Eike, L.; Lunteren, J. V. (2015). Memristor based computation in memory architecture for data intensive applications. *In proceedings of the 2015 design, Automation and Test in Europe conference and Exhibition*, pages 1718-1725.

111. Wang, W.; Jing, T. T.; Butcher, B. (2010). FPGA based on integration of memristors and CMOS devices. *Proceedings of 2010 IEEE international symposium on circuits and systems,* 11462826.

112. Vourkas, I. (2016). Emerging memristor-based logic circuit design approaches: A review. *IEEE Circuits and Systems magazine*, 16, pages 15-30.

113. Prezioso, M.; Bayat, M.; Hoskins, B. D.; Adam, G. C.; Likharev, K. K.; Strukov, D. B. (2015). Training and operation of an integrated neuromorphic network based on metal-oxide memristors. *Nature*, 521, pages 61–64.

Chapter 2

Materials, Methods & Technologies

2.1 Introduction

The field of memristors is under vigorous research phase. Since there is no unique memristors with unique switching properties which can be regarded as the device to replace the silicon technology, a great deal of studies are being conducted on the switching medium, switching mechanism, device structure etc. A number of studies have been reported in this field, each of which displays good engineering properties.

This chapter deals mainly with all the materials, characterizations and other technologies used during the entire framework of research. Since the main focus during the PhD programme was on polymer NC based RSDs, several polymer based switching composites were synthesized and characterized. Several electrode configurations have also been studied in order to understand the switching differences. This chapter gives a thorough understanding on how the polymer NCs and corresponding switching devices were fabricated. All the electrical, optical and chemical characterizations carried out on the switching matrix as well as on the device will be discussed in this chapter.

2.2 Device Architecture

Device architecture plays an important role in the behavior of the RSD. Architecture in this particular study refers to the electrode structure as well the electrode symmetry. In the present work we have considered planar as well as

stacked device. RSDs very much depend on the electrode structure and symmetry [**1, 2**].

2.2.1 Planar Symmetrical Device based on Au electrodes

The use of planar devices are not common when it comes to real time applications. But during the initial phase of any study, these device architectures are always preferred due to the possibility for a clear visualization of what happens in the matrix or the device itself while electrically probed.

A planar device structure with gold (Au) electrodes separated by a 10 μm gap is the initial architecture of choice. The fabrication technique of this particular device is as follows: Electron beam evaporator (ULVAC EBX-14D) was used in order to deposit the gold electrodes on a (100) oriented Si wafer with a 200 nm SiO_2 layer grown using dry oxidation. A Ti layer (10 nm thick) was used to promote adhesion of the Au layer (100 nm thick) to the substrate. Both layers were grown using a deposition rate of 0.3 nm/s. Electrodes were patterned using AZ5214E photoresist (Microchemicals) in a standard UV photolithographic process, with the aid of a Neutronix Quintel NXQ 4006 mask aligner. Au layer was selectively etched using a solution made by Iodine (I_2) and Potassium Iodide (KI) in water, with an estimated etch rate of 0.2 nm/s. The underlying Ti layer was etched using a solution of Hydrofluoric Acid (HF) and Hydrogen Peroxide (H_2O_2) in water. The final step involves the dicing of the substrates using a diamond dicing saw, in order to obtain samples with an area of 5 mm x 7 mm, each with three identical Ti/Au electrodes. The electrodes have a width of 300 μm, and they are separated by a 10 μm gap. The final switching matrix is then deposited onto the planar device.

2.2.2 Planar Asymmetrical Device based on Ag and Pt electrodes

The planar asymmetrical device structure used in our case is not much different from the planar symmetrical case. In this particular architecture, we use 2 different electrodes. Instead of inert electrode (Au), we use an active as well as a passive electrode (Ag, Pt).

The use of a passive and an active electrode is the most common electrode design for normal RSDs [**3, 4**]. The presence of an active metal like Ag, Cu etc takes active part in the switching mechanism due to the REDOX process happening in the device when biased. In our study we have fabricated a planar device with Ag and Pt electrodes deposited on Si wafer with 10 μm gap between them. The fabrication techniques are mostly same as that of the planar symmetric

case, except for the Au electrodes, we have a Pt electrode (100 nm thick) deposited using a Kurt J. Lesker PVD 75 DC sputtering, at a deposition rate of 0.2 nm/s. A 20 nm thick Ta layer was used as the adhesive layer for Pt on Si. The electrode was patterned using lift off process. DMSO was used as the solvent. The Ag electrode (100 nm thick) was patterned using the same image reversal photoresist used for Pt and then 100 nm Ag was deposited using an Ulvac EBX-14D electron beam evaporator, at a deposition rate of 2.0 nm/s. A 20 nm thick titanium (Ti) adhesion layer was electron beam deposited before the Ag layer at a deposition rate of 0.3 nm/s. Lift-off in DMSO was the final patterning step. **Figure 2.1** provides the schematic representation of the planar device. During electrical characterization, the active bias will always be provided to Ag and Pt electrode will be grounded.

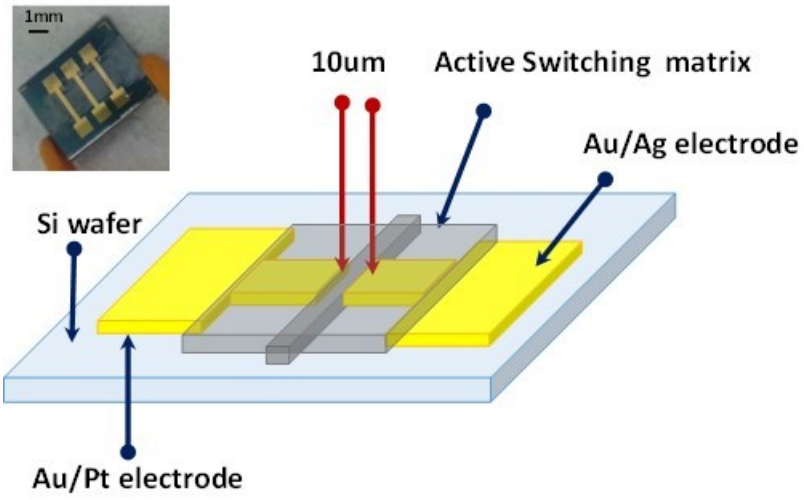

Figure 2.1: Schematic representation of the planar device. Inset shows the image of the real device with switching matrix deposited on the device **[1].**

2.2.3 Stacked Device

Device architecture plays an important role while it comes to scaling in practical circuit models. Since the active switching gap between the electrodes is much less in this particular case, stacked structure is preferred over planar architecture. In the present thesis work we have discussed mainly two stacked device structures. One has symmetrical Au electrodes while the other has Au and ITO as electrode.

2.2.3.1 Au/ITO based stacked device

The layered configuration set up is as follows: The bottom electrode (BE) comprises of a commercially bought glass substrate with an Indium Tin Oxide (ITO) coating. The active switching matrix is then deposited onto the ITO BE. Once the active switching matrix is deposited onto the ITO based BE, the Top electrode (TE) which is Au (100 nm) is deposited using a shadow mask. The TE was in the form of circular disks which had diameters varying from 1 mm to 4 mm. **Figure 2.2** provides the schematic representation of the stacked asymmetric device.

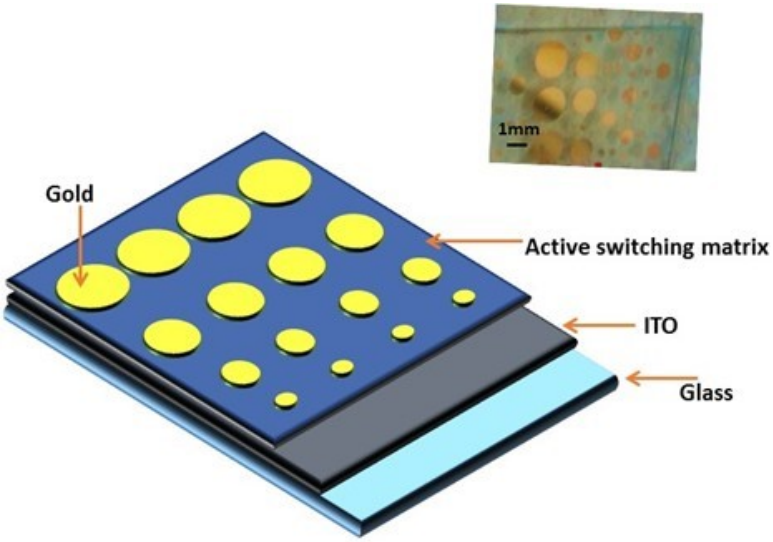

Figure 2.2: Schematic representation of Au/ITO based stacked device. Inset provides the real image of the stacked device.

2.2.3.2 Au/Au based stacked device:

The device design of the stacked symmetrical device is more or less similar to the stacked asymmetrical device. In this case the BE, that is Au is deposited onto a Si substrate with 100 nm thermal oxide. The BE was deposited by evaporation method (deposition rate of 0.1 nm/s) using a shadow mask. A dog bone structure was used for the electrode. The BE was 20nm in thickness. Before the Au layer deposition an adhesive layer of Ti (2nm) was deposited. After the BE deposition, we have our active switching matrix deposited which will be discussed in section **2.3.6**. The TE (20 nm of Au) is deposited again using the same shadow mask which was used for the BE using Evaporation. **Figure 2.3** provides the SEM image of the final device.

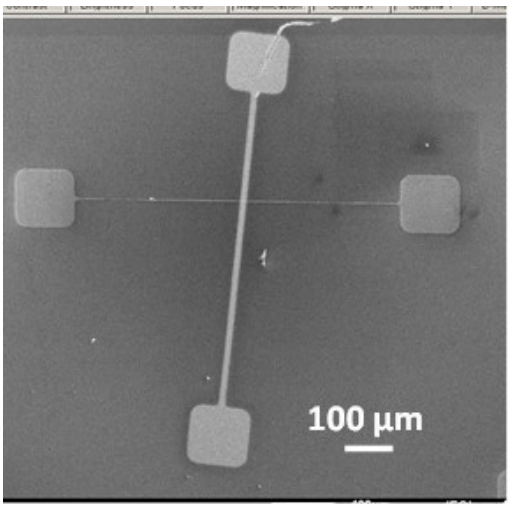

Figure 2.3: SEM image of BE deposited using dog bone shadow mask.

2.3 Polymer NC based Switching Matrix Preparation

The preparation of various polymer NCs plays an important role in the present work. Different polymer based matrices were synthesized along with Ag and Au NPs. The coming subsections provide a detailed synthesis method of all the switching matrices used throughout our research work.

2.3.1 Ex-Situ Ag based Switching matrix

The preparation of a polymer NC by means of adding already synthesized NPs into a polymer matrix provides an easy way of synthesizing a switching matrix.

The Ex-Situ Ag NP based switching matrix preparation is as follows: Here Ag NP solution is added directly to a polymer solution and mixed well inorder to obtain a good NP dispersion in the polymer matrix. In the present work, Poly vinylidene fluoride-hexafluoropropylene (PVDF-HFP) was used as the polymer matrix due to its high dielectric constant, good mechanical strength and due to its chemical stability **[5, 6]**. The presence of HFP in PVDF reduces its crystallinity, thus making it soluble in a wide range of solvents. The PVDF-HFP matrix acts as a quasi-solid medium for the silver NPs and silver ions supporting their movements when an electric field is applied. PVDF-HFP (10 wt. %) Kynar-Superflex 2500 (pellets) with 20 wt% of hexafluoropropylene and a density of 1.79 g cm^{-3} was dissolved in DMF (Dimethyl Formamide) by vigourous stirring for 20 to 30 minutes at 30°C. The final Ag NP suspension (Ag-NP Ethanol suspension has Ag content of 6.8 wt%, with an average NP diameter of about 40 nm which includes a PVP coating) was then added to the polymer solution such

that the final composition of Polymer to Ag NPs was 50/50. It has to be noted that in the present case we have also developed Ag NP and PVDF-HFP based switching matrix with DMSO (Dimethyl Sulfoxide) as solvent in the exact similar way as it was made with DMF. DMSO and DMF solvents didn't create difference in the electrical behaviour of the device. The switching matrix used DMSO as solvent when the switching matrix was deposited using inkjet printing method, while DMF was used during spin coating method. The Ag NP used in our experiments has an outer coating of PVP, which avoids the agglomeration of these NPs. **Figure 2.4** provides the TGA plot of the commercially bought Ag NPs. The protective PVP coating around the NP started to decompose from 250 °C up to 550 °C and a weight loss of 5% was observed.

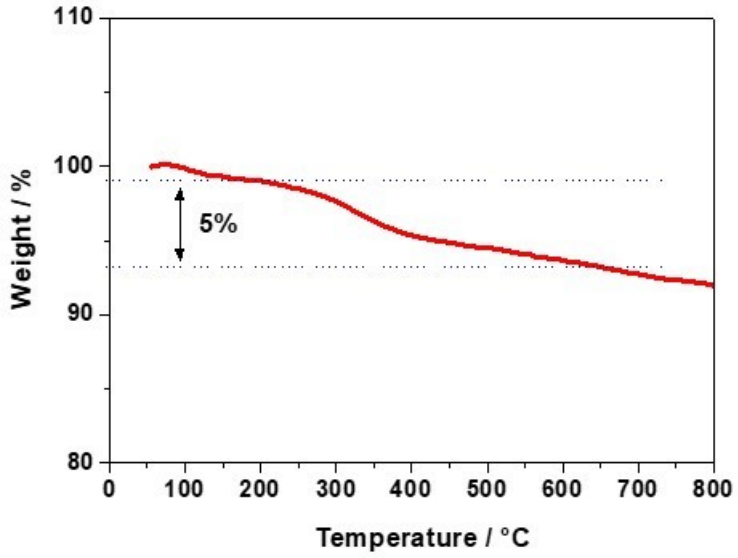

Figure 2.4: TGA analysis performed on Ag NP suspension.

The Ag NP suspension and Polymer solution was well sonicated for 30 minutes so that a well dispersed Ag NP polymer matrix was obtained. **Figure 2.5** provides the schematic representation of the Ag NP based switching matrix preparation. The most important fact about this switching matrix is that it is totally compatible with flexible substrates, which widens its range of applications; in fact, there is a great deal of microelectronic thrust that is focusing on the development of new materials, which can be cost effectively deposited with extreme ease on a variety of substrates like paper, fabrics and plastics **[7]**, making them attractive component for printed electronics.

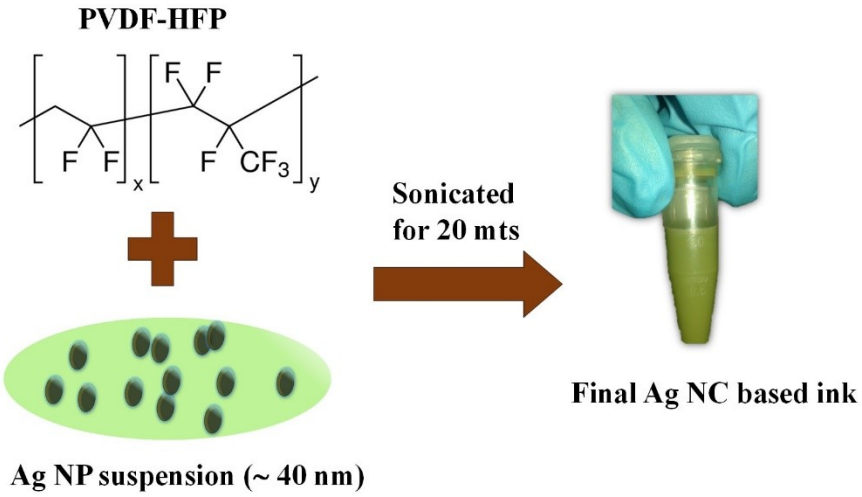

Figure 2.5: Schematic representation of the finally prepared Ag NP based switching matrix

Moreover, the formulation is processed at room temperature, which is one of the foremost properties that allows the material to be deposited on the cheapest flexible substrates, including paper. The achievable device uniformity **[8]**, the cheaper production method and the easy deposition technique along with the advantage of room temperature processing make these NCs preferred in the field of disposable devices [**9, 10**]**. Figure 2.6** provides the SEM image of the AG NP, PVDF-HFP based switching matrix.

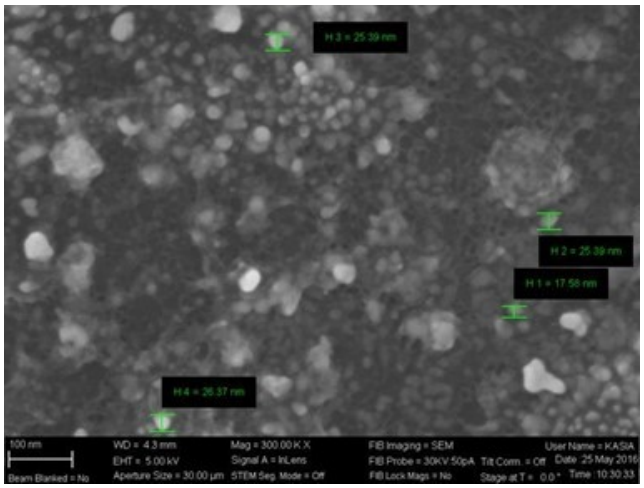

Figure 2.6: SEM image of the switching composite

The present Ex-situ Ag NP and PVDF-HFP based switching matrix was made to undergo an impedance measurement and was observed that (**Figure 2.7**) the matrix clearly had an increase in its conduction or a clear reduction in the matrix resistance with increase in frequency. This behaviour is something which is foreseen in resistive switching matrices.

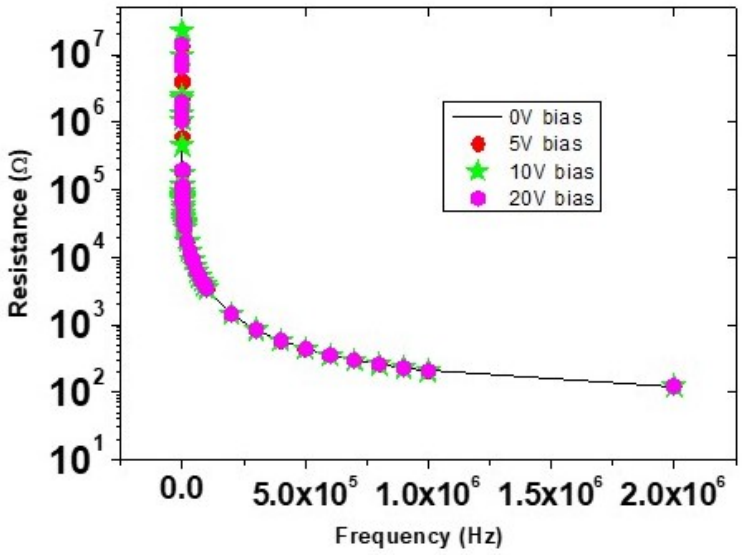

Figure 2.7: Impedance measure performed on the Ag NO and PVDF-HFP based switching matrix.

2.3.2 In-Situ Ag based Switching matrix

In the present research, we use a photochemical method for the preparation of metallic NPs. This reaction is mainly based on the reduction happening to the metal cation (M^{n+}). This direct photo reduction process helps in the formation of M^0 through the direct excitation of the metal source, usually a salt. In this case as we discuss about the synthesis of Ag NPs by the UV induced reduction process, we can generalize this by the below reaction:

$$Ag^+ + H_2O \xrightarrow{h\upsilon} Ag^0 + H^+ + HO^* \qquad (2.1)$$

These Ag atoms then aggregates and form Ag NPs.

$$nAg^0 \rightarrow Ag\ NP \qquad (2.2)$$

Here, the basic idea is to use the electrically passive polymer matrix as an active element for controlling the embedded NPs and thus the electronic

properties of the NC. A triple step method is employed for the synthesis process. First, a precursor of metal NPs (i.e., silver nitrate) is dispersed into the PVDF-HFP/DMF solution. Second, the system undergoes light exposure in the visible range to activate photo polymerization, generating the polymeric matrix and avoiding at the same time the precipitation of the silver phase. Finally, nucleation and growth of Ag NPs are driven at room temperature using a UV light source. The presence of DMF also plays an important role in the reduction of silver or gold salts.

The polymer matrix used in this case is same as the previous case. We use PVDF-HFP/DMF polymer solution. $AgNO_3$ is added to the PVDF-HFP solution ($AgNO_3$ is 5% with respect to PVDF-HFP) and sonicated for 20 minutes. This final mix of silver salt and polymer solution is then spin coated onto the ITO substrate. The device with the coated switching matrix is then exposed to UV radiation using an ultra violet lamp at 250 nm with light intensity of 10 mW/cm^2 for 60 mts. This one hour of UV exposure helps in the reduction of Ag^+ to Ag^0.

2.3.3 PVDF-HFP_$AgNO_3$_Ionic Liquid

The PVDF-HFP, $AgNO_3$ and Ionic Liquid (IL) based switching matrix is similar to the matrix explained in section **2.3.2**, except that here we don't perform any photo reduction process, also the presence of IL also plays a major role in the physical and chemical properties of the switching matrix [**11,1**]. ILs are molten salts at room temperature. The presence of IL helps in an increased ionic conductivity.

The preparation of the switching matrix is as follows: 10 wt. % of PVdF-HFP was dissolved in DMF and is well stirred for about 45 min at 60ºC. $AgNO_3$ is then added to the above polymer solution and sonicated for 20 minutes thus obtaining a clear solution. Finally Butyl-3-methylimidazolium bis(trifluoromethanesulfonyl)imide (BMI TFSI) is added to the above PVDF-HFP and $AgNO_3$ solution. The final composition (wt. %) of PVDF/$AgNO_3$/IL is 65/5/30. The importance of IL can be understood from the following DSC analysis.

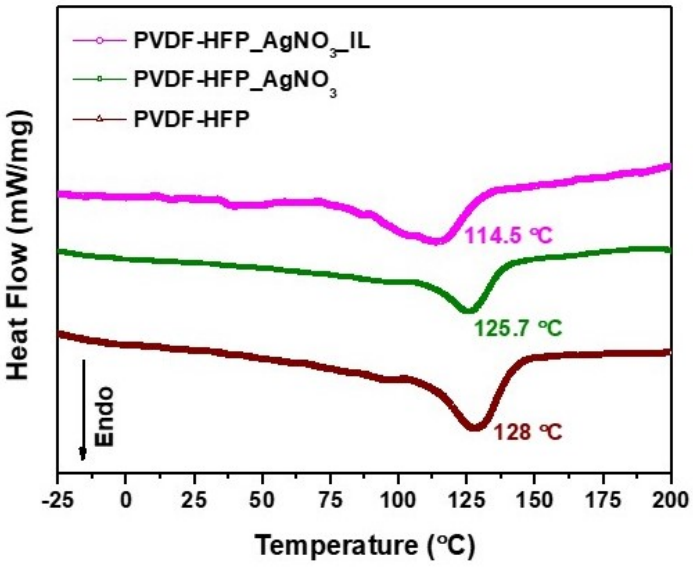

Figure 2.8: DSC thermograms of pure Poplymer (PVDF-HFP), PVDF-HFP_$AgNO_3$ and finally PVDF-HFP_$AgNO_3$_IL

As seen from **Figure 2.8**, the pure PVDF-HFP matrix has a melting peak around 128^0C. This peak reduces with the addition of $AgNO_3$. A further addition of IL to PVDF-HFP and $AgNO_3$ matrix led to a further reduction in the melting depth of the melting peak as well as a reduction in the melting peak value. The melting peak of the PVDF-HFP_$AgNO_3$_IL matrix broadened. Otherwise this change in the matrix with IL tells us that there was a plasticizing effect with the addition of IL into the polymer silver salt based switching matrix. By integrating the melting peaks of PVDF-HFP, PVDF-HFP_$AgNO_3$ and PVDF-HFP_$AgNO_3$_IL, it was observed that the area corresponding to the three matrices were 10.5 J/g, 4.935 J/g and 1.83 J/g respectively. This reduction in the area corresponding to PVDF-HFP_$AgNO_3$_IL indicates that presence of BMI-TFSI facilitates the polymer backbone softening, thus enhancing the segmental motion of the polymer chain thus making it less crystalline [**1**]. **Figure 2.9** provides the SEM images of the present switching matrix with IL.

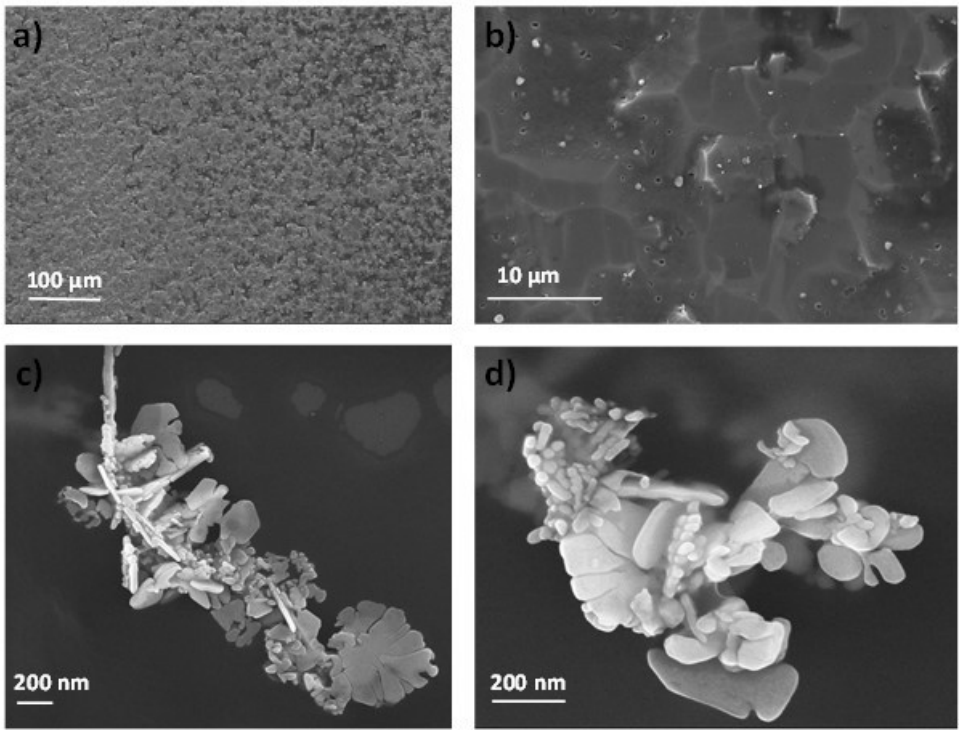

Figure 2.9: FESEM image of the PVDF-HFP_$AgNO_3$_IL matrix at different magnifications

Figure 2.10 provides the ATR FTIR plot of the PVDF-HFP_$AgNO_3$_IL switching matrix.

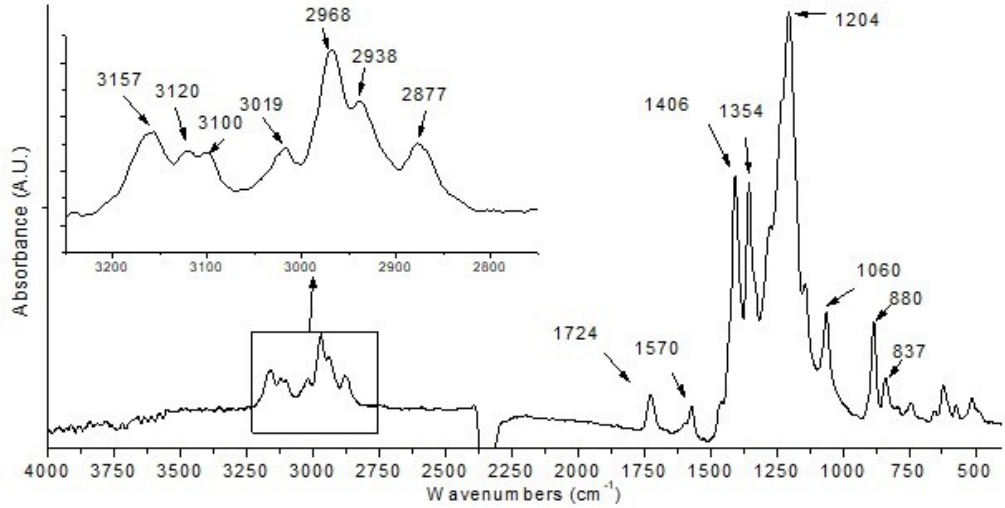

Figure 2.10: ATR FTIR spectra of PVDF-HFP_$AgNO_3$_IL

As seen from **figure 2.10**, we can see the main absorbance due to PVDF-HFP from bands: 1406 cm^{-1} for the vinylidene CH_2 wagging and CH_2 scissoring vibration while the wagging and rocking of the vinylidene bands are still at 880 and 837 cm^{-1}. The other bands are partially superimposed with the C-F vibrations of IL. 1354 cm^{-1} band 1204 and 1060 cm^{-1} are associated to the presence of C-F and SO_2 stretching of bis(trifluoromethanesulfonyl)imide. The absorbance in the 2800 to 3200 cm^{-1} region is mainly due to the 1-butyl-3-methyl imidazolium cation (BMIM). The butyl chain attached to the imidazolium ring originates peaks at 2968 and 2877 cm^{-1} the symmetric and antisymmetric stretching of CH_3 while the stretching antisymmetric of CH_2 is located at 2938 cm^{-1} the other peaks in the 3050-2800 cm^{-1} region are difficult to recognize unless the 3019 cm^{-1} peak that is due to the CH_2 antisymmetric stretching of PVDF-HFP. Bands above 3050 cm^{-1} are from the C-H vibrational modes of the imidazolium ring, peaks at 3120 and 3157 cm^{-1} are for antisymmetric and symmetric stretch vibrational modes of HC(4)-C(5)H of BMIM and the peak shown as the shoulder around 3100 cm^{-1} is assigned to the stretch vibrational mode of C(2)-H.3. Finally, in the 2000-1600 cm^{-1} region, two peaks are present. The first at 1570 cm^{-1} which is due to the C-C stretching of the BMIM ring. While the second at 1724 cm^{-1} which ^{is} probably due to the presence of DMF solvent impurities that are difficult to eliminate being miscible with the ionic liquid [**1**].

The viscosity of the present PVDF-HFP_$AgNO_3$_IL based switching matrix is 30 cP, which is an acceptable viscosity for inkjet printing in the case of heated print head, making this switching matrix suitable for flexible printed electronics.

2.3.4 PEO_$AgNO_3$_Ionic Liquid

The enhanced switching properties of polymer NC based switching matrices with the addition of IL led to the usage of different polymers and study of their switching behaviour. Poly (ethylene Oxide) PEO can be considered as an excellent candidate to realize an RSD due to its high solvating properties for a wide variety of salts through interaction of the ether oxygens with cations [**2, 12**].

2 wt% of PEO (average molecular weight of 1,000,000) solution in deionized water was prepared by vigorous stirring for 10 to 12 hours at 40 °C. $AgNO_3$ was then added to the PEO solution and sonicated for 20 minutes, obtaining a clear solution. BMIM-TFSI was then added directly and sonicated for 20 minutes. The final composition was 45/20/35 of PEO/$AgNO_3$/IL respectively. [The same matrix has also been prepared with DMF as solvent instead of deionized water for comparison studies.]

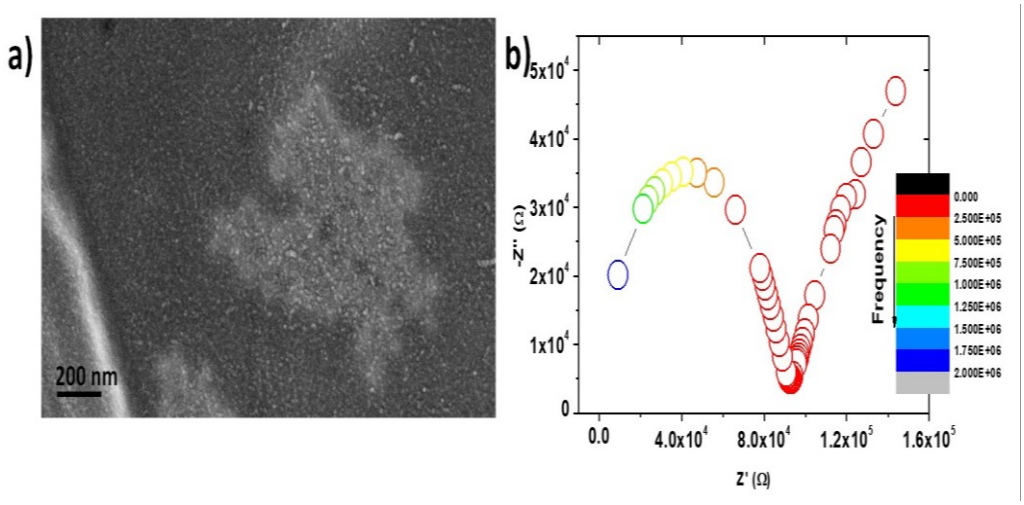

Figure 2.11: Switching matrix characterization. a) FESEM image of the PEO_ Ag NO_3_IL matrix. b) Nyquist response of PEO_AgNO3_IL matrix.

Figure 2.11a provides the SEM images of the PEO based switching matrix with IL. The impedance spectrum of the PEO_$AgNO_3$_IL based switching matrix (**Figure 2.11 b**) provides a clear difference between the low and high frequency region. The high frequency region visualizes a semicircular plot which can be ascribed to the bulk resistance of the matrix, while the spike at the lower frequency region can be attributed to the electrolyte. **Figure 2.12** provides the DSC analysis of the PEO_$Agno_3$_IL based matrix and PEO_$AgNO_3$ based switching matrix. This plot provides a clear evidence that the addition of IL has led to a reduction in the melting peak of PEO and IL based matrix, which further signifies the reduction in the crystallinity of the switching matrix.

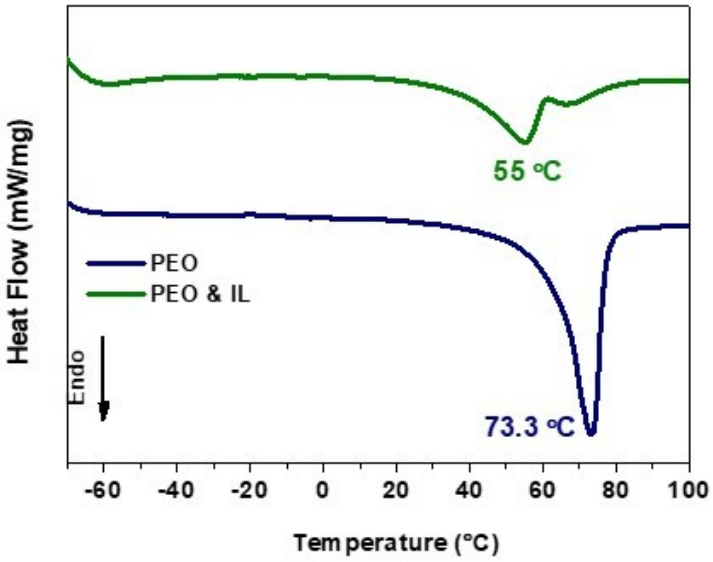

Figure 2.12: DSC thermograms of pure Polymer (PEO) and PEO_$AgNO_3$_IL matrices.

2.3.5 PMMA_$AgNO_3$_Ionic Liquid

The switching matrix based on Poly (methyl methacrylate) was synthesized similarly as that of PVDF-HFP. A solution of PMMA was prepared by solubilizing PMMA (10 wt. %) in DMF for 2 hours at 40^0C. $AgNO_3$ was then added to the above PMMA solution and sonicated for 20 minutes obtaining a clear solution. BMIM-TFSI was added directly to the above solutions and sonicated for 20 minutes. The exact composition of final PMMA/$AgNO_3$ / IL is 65/5/30.

2.3.6 PMMA. A2_Au NPs

The final Polymer based NC prepared in the current research includes PMMA A2, which is a commercially available positive photoresist. The present PMMA matrix (950 k molecular weight) is dissolved in Anisole (2wt% of PMMA in anisole).

The final switching matrix involves the initial deposition of PMMA A2 solution on Si wafer at a rotation speed of 6000RPM at 150°C which leads to a final PMMA thickness of about 35 nm. The deposited polymer matrix is then heated at 105^0C for about 1 to 2 minutes. After the heating process, Au NPs are deposited using E-beam evaporator at 0.1 nm/s. The deposited layer of Au is about 4 nm. Once the 4 nm Au layer is deposited on the 35 nm PMMA layer an intense heating process is performed at 110^0C for 6 hours. This 6 hours heating

process makes the Au NPs (Average diameter of 40 to 50 nm) to disperse in the PMMA layer. After the complete preparation of this switching matrix, the TE is deposited using evaporation method.

2.4 Switching Matrix Deposition Techniques

So far we have discussed about various switching matrices used. These matrices has to be deposited on to the RSD by means of some methods. Spin coating and Inkjet Printing are the 2 techniques used in our work.

2.4.1 Spin Coating

Spin coating is one of the easiest, cost effective and the fastest way to deposit a uniform and thin layer of film onto a flat substrate. Since this technique is one of the easiest and cost effective methods, we have used this deposition technique for all the above mentioned switching matrices.

All the matrices presented here have been deposited onto the devices by spin coating method. The spin speed used to deposit the matrix based on the matrix viscosity will control the film thickness. In the present work, matrices discussed from section **2.3.1** to **2.3.5** have been deposited at room temperature at a speed of 3000RPM for 30 seconds. This particular rotation speed at this particular time led to a film thickness of about 300 to 500nm. The polymer PMMA.A2 which is discussed in section **2.3.6** was deposited onto the substrate at 6000RPM for 60 seconds at 150 °C. This high speed led to a polymer film thickness of about 35 nm. Thus it's clear from the working of the spin coater that higher the spinning, lesser is the film thickness. Even though this deposition technique is easy and can be performed on almost all flat substrates, it's not a very uniform deposition technique.

2.4.2 Inkjet Printing

Inkjet printing is a technology considered suitable for printed electronics due to the wide range of materials that can be deposited onto a wide range of substrates on large scale. The major advantage of inkjet printing being the possibility to add functionalities on a substrate that already has electronic structures and devices fabricated using some other technologies.

The entire printing experiments were conducted using piezoelectric Inkjet printing method (JETLAB 4-XL). In this case the only switching matrix that has been deposited using ink jet printing is the one discussed in section **2.3.1** but with DMSO as solvent. The general working of a piezoelectric inkjet printer is as

follows: A piezoelectric material is present in the ink filled chamber behind the nozzle. When a voltage is applied, the piezoelectric material will change shape, generating a pressure on the ink or fluid causing the ink form a droplet and fall out from the nozzle. The applied pulse waveform controls the drop created and ejected from the nozzle. Pulse shape parameters, pulsing frequency, trigger source and trigger mode printing parameters are optomized for various inks [**13,14**]. **Figure 2.13** provides the waveform which was used to generate drops and the inset provides the view of the ejected ink drop.

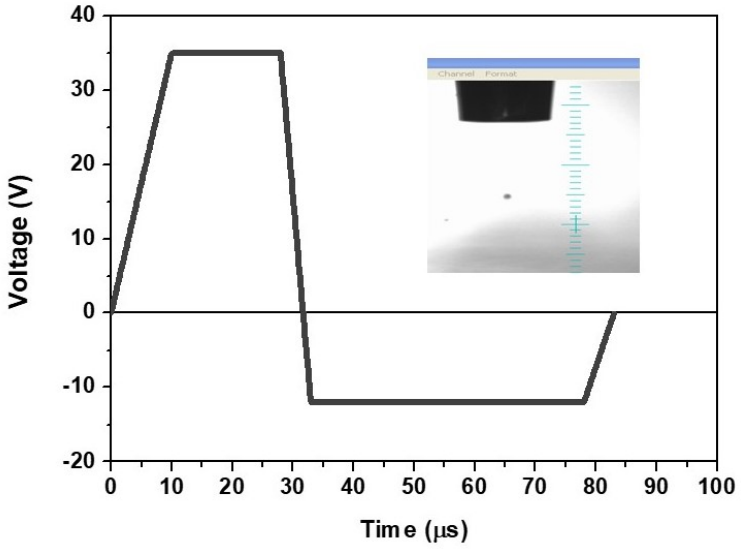

Figure 2.13: Voltage waveform applied to generate ink droplet. Inset provides the ink drop ejected from the nozzle

2.5 Characterization Techniques

A lot of characterization techniques have been used in the present research. Electrical, Optical and Physical characterizations are the most performed characterizations on the devices and the switching matrix.

Electrical characterization includes DC cyclings performed on the Devices, Pulse measurements and the temperature based measurements. Keithley 4200-SCS Semiconductor Characterization System and Keysight B-1500A semiconductor device parameter analyzer were used to perform the DC and pulse measurements. The characterization of the device was carried out using tungsten (W) micro probes, which were directly placed in contact with the electrodes in order to maintain electrical connection. The DC and pulse characterizations were carried out in air at room temperature. In the stacked case with asymmetrical

electrodes (Au/ITO), the electrodes were probed using a cylindrical structure (both diameter and height were 2 mm), which was kept in contact with the gold TE, and then the W needle was kept on the cylinder thus achieving connection with the system (inset **Figure 2.14**). The connection to the ITO BE was made directly through the W needle. In the stacked asymmetrical electrode configuration, the active bias was provided to ITO, while Au electrode was kept as the reference electrode (0 V). The electrical characterization was carried out in air at room temperature.

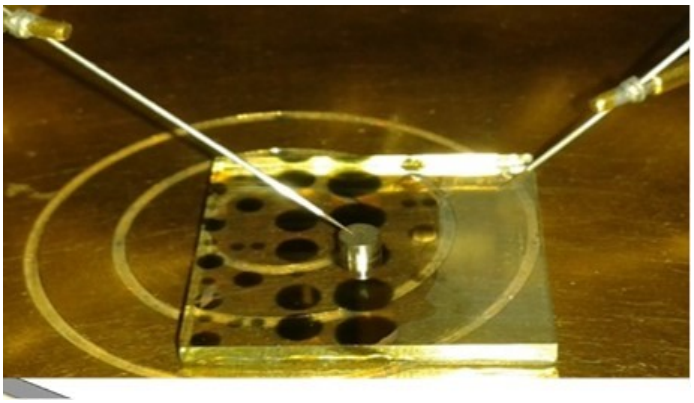

Figure 2.14: Probe set up for electrical measurement in stacked Asymmetrical device

The electrical measurement performed by varying the temperature was performed by using an H-50 Hall,Van-der Pauw controller (MMR-Technologies, INC) under vacuum. Temperature was controlled and stabilized by means of gaseous nitrogen extraction cryostat.

Field Emission Scanning Electron Microscopy (FESEM, ZEISS Dual Beam FESEM-FIB Auriga) equipped with an Energy Dispersive X-ray spectrometer (EDS, Inca XSight; Oxford Instruments) was used to perform the morphology and the compositional characterization of nanocomposite structures and the devices.

Optical microscopy image was taken on the sample before and after electrical characterization using Leica DFC295. Mat lab program was used in order to enhance the difference between the pristine sample (before electrical characterization) and the stressed one (after electrical characterization) [**9, 10**].

Differential Scanning Calorimetry (DSC) was carried out on all switching films. The results were acquired using DSC 204 F1 Phoenix® (Netzsch) instrument under a continuous nitrogen flow of 20 ml/minute. The samples were

cooled from room temperature to -70 °C and heated to a maximum of 250 °C at the rate of 10 °C per minute.

FT-IR transmittance spectra were collected on a Tensor 27 FTIR Spectrometer (Bruker). The samples were prepared by spin-coating the two formulations on a Si wafer using the same conditions of RSDs. The averaged signal was collected with a resolution of 2 cm^{-1} from 4000 to 600 cm^{-1}.

X-ray photoelectron spectroscopy (XPS) studies were carried out by a PHI 5000 Versaprobe scanning X-ray photoelectron spectrometer (monochromatic Al K-alpha X-ray source with 1486.6 eV energy, 15 kV voltage, and 1 mA anode current) in order to investigate surface chemical composition. A spot size of 50 μm was used to collect the photoelectron signal for both the high resolution (HR) and the survey spectra. All samples were analyzed using a combined electron and argon ion gun neutralizer system to reduce the charging effect during the measurements. Spectra were analyzed using Multipak 9.6 software.

2.6 References

1. Rajan, K.; Chiappone, A.; Perrone, D.; Bocchini, S.; Roppolo, I.; Bejtka, K.; Castellino, M.; Pirri, C. F.; Ricciardi, C.; Chiolerio, A. (2016). Ionic liquid-enhanced soft resistive switching devices. *RSC Advances*, 6, pages 94128-94138.

2. Rajan, K.; Bejtka, K.; Bocchini, S.; Perrone, D.; Chiappone, A.; Roppolo, I.; Pirri, C. F.; Ricciardi, C.; Chiolerio, A. (2017). Highly performing Ionic Liquid enriched hybrid RSDs. *Journal of Material Chemistry C*, 5, pages 6144-6155.

3. Ge, N.; Zhang, M. X.; Zhang, J.; Yang, J. J.; Li, Z.; Williams, R. S. (2014). Electrode-material dependent switching in TaO_x memristors. *Semiconductor Science and Technology*, 29, 104003.

4. Gale, E.; Pearson, D.; Kitson, S.; Adamatzky. A.; Costello, L. B. (2015). The effect of changing electrode metal on solution processed flexible titanium dioxide memristors. *Material Chemistry Physics*, 162, pages 20-30.

5. Wu, F.; Feng, T.; Bai, Y.; Wu, C.; Ye, L.; Feng, Z. (2009). Preparation and characterization of solid polymer electrolytes based on PHEMO and PVDF-HFP. *Solid State Ionics*, 180, pages 677-680.

6. Ataollahi, N.; Ahmad, A.; Hamzah, H.; Rahman, M. Y. A.; Mahamed, N. S. (2012). Preparation and characterization of PVDF-HFP/MG49 based polymer blend electrolyte, *International Journal of Electrochemical Science*, 7, pages 6693 – 6703.

7. Stoppa, M.; Chiolerio, A. (2014). Wearable electronics and smart textiles: a critical review, *Sensors*, 14, pages 11957-11992.

8. Hwan, Y. H.; Seo, J. S.; Yun, J. M.; Park, H. J.; Yang, S.; Park, S. H.; Bae, B. (2013). An 'aqueous route' for the fabrication of low-temperature-processable oxide flexible transparent thin-film transistors on plastic substrates. *NPG Asia Materials*e, e45.

9. Rajan, K.; Bocchini, S.; Chiappone, A.; Roppolo, I.; Perrone, D.; Bejtka, K.; Ricciardi, C.; Pirri, C. F.; Chiolerio, A. (2017). Spin-coated silver

nanocomposite resistive switching devices. *Microelectronic Engineering*, 168, pages 27-31.

10. Rajan, K.; Bocchini, S.; Chiappone, A.; Roppolo, I.; Perrone, D.; Castellino, M.; Bejtka, K.; Lorusso, M.; Ricciardi, C.; Pirri, C. F.; Chiolerio, A. (2017). WORM and bipolar inkjet printed resistive switching devices based on silver nanocomposites. *Flexible and Printed Electronics*, 2, 024002.

11. Fernicola, A.; Scrosati, B.; Ohno, H. (2006). Potentialities of ionic liquids as new electrolyte media in advanced electrochemical devices. Ionics, 12, pages 95-102.

12. Goreckit, W.; Jeannin, M.; Belorizky, E.; Roux, C.; Armand, M. (1995). Physical properties of solid polymer electrolyte PEO (LiTFSI) complexes. *Journal of Physics: Condensed Matter*, 7, pages 6823-6832.

13. Martin, G. D.; Hoath, S. D.; Hutchings, I. M. (2008). Inkjet Printing- the physics of manipulating liquid jets and drops Journal *of Physics Conference Series,* 105, 012001.

14. Wijshoff, H. (2010). The dynamics of piezo inkjet printhead operation. *Physics Reports,* 491, *pages* 77- 177.

Chapter 3

Metallic Ag NP based RSD

3.1 Introduction

Hybrid nanomaterials have gained widespread interest due to their novel properties in various fields of science including optoelectronics, anti-bacterial, medicine, environment applications etc. The current chapter deals with the role of Ag NPs in a polymer matrix to induce resistive switching.

The metallic NPs can be added into the polymer matrix either directly (ex-situ method), where commercial or separately prepared NPs are dispersed into the polymer matrix, or indirectly (in-situ method), where metallic particles are formed in the polymer matrix during their synthesis [**1**]. The preference for in-situ or ex-situ method depends on the particular application. The in-situ method controls the properties of the composite by controlling the reactions conditions and by choosing the appropriate route thus leading to a stable matrix [**2**]. Ex-situ based composite preparation on the other hand is less difficult when compared to in-situ. The incorporation of metallic NPs in an insulating matrix provides a conducting path between the electrodes when the concentration of particles is above the so-called percolation threshold [**3**]. We will see that by using a dissipative (hence not totally insulating) matrix enabling the establishment of a certain current, it is possible to induce atoms /ions to migrate and literally form aggregates of NPs that create filaments bridging opposite electrodes. Use of NPs in polymer NC is an interesting topic of research. The importance of NPs is connected with their scale, bringing surface tension and ionic forces to that level of importance that allows a play against gravity, giving stability to a suspension. But many other interesting

phenomena occur: collective electron resonances, the so-called plasma waves enabling surface plasmon resonance (SPR), and interactions with the electromagnetic field [**4,5**]; a huge enhancement of diffusivity of the surface atoms, enabling "melting" (sintering) at extremely low temperatures [**6**], and so on. In a world where nano engineered materials could have broad application, from the consumer electronics market, building industry, pharmaceutical and cosmetic products, to food and the environment, we can easily imagine that the role of NP synthesis and modification activities will be huge. The importance of Ag among other metallic NPs is worth mentioning. Ag is a noble metal, featuring undisputed advantages in terms of electrical conductivity, resistance to oxidation, and providing interesting plasmonic and antibacterial properties. It is difficult to imagine a future without the use of Ag, at least for certain critical systems that cannot lose efficiency. The market share will be reduced in favour of other nano engineered, less expensive materials, but it is not possible to avoid the use of metals to transport electricity without losses. Once again the prominence of Ag in hybrid NCs or metallic inks can be stated by its impressive properties like: optimal electron conductivity and a lower affinity for oxygen if compared to copper, it is 25 times more abundant than gold on Earth's crust, and hence is less expensive. Silver NPs and nanocomposites (NCs) possess interesting electrical, optical, and chemical properties used in catalysis, surface-enhanced Raman spectroscopy (SERS), nanoelectronics, photonics, and biological and physical sensing [**7-10**]. Shape and dimension of Ag NPs are easily controllable, resulting in tunable properties [**10**]. As mentioned earlier in this thesis, memory devices with organo metallic components have unique advantages over inorganic devices, including higher flexibility, low cost, 3D stacking capability, solution processibility etc. Part of the work described in this chapter has been previously published in "*Microelectronic Engineering, 168, 2017, (27-31)* and in *Flexible and Printed Electronics, 2, 2017, (024002)*."

3.2 Nanoparticle Synthesis Methods

Nanoparticles or nanocrystals can be fabricated using two different approaches: the first, known as "top-down", utilizes physical methods to reduce crystal size, while the other, the "bottom-up" approach, is based mainly on solution-phase chemistry and also named wet chemistry [**12, 13**]. Physical methods usually allow the production of a large quantity of nanocrystals, but is very difficult to control geometry or have a uniform size. In contrast, wet chemical synthesis allows the synthesis of nanocrystals with controlled particle size.

The properties of the metallic NPs incorporated in the polymer NC is very crucial since the size and shape of these NPs influence the NC. For these reasons wet chemical synthesis is generally preferred. In this context, a wide variety of wet-synthesis techniques have been proposed to produce metal nanocrystals and in particular Ag nanocrystals, including chemical reduction [**14-16**], electrochemical and photochemical reduction [**17-19**], sonochemistry, and heat evaporation [**20,21**]. The main method involves the bottom-up synthesis, starting from the silver salts and leading to final nanocrystal. Three distinct steps are involved in this process [**22**]: clusterization of few atoms or ions, formation of a seed through atom-by-atom addition to the initial nuclei, growth of seed (shape determined by the structure of the seed). In the case of Ag, the initial precursor is in +1 oxidation state (Ag^+), and thus during the reaction Ag^0 atoms are produces as metal nanocrystals. Silver salts are usually insoluble in any solvent, and thus the most used precursor for Ag nanocrystal production is silver nitrate ($AgNO_3$), which has good solubility in polar solvents. The preferential seed shapes from silver salt reduction are icosahedral and decahedral, thermodynamically favoured from the face-centred cubic lattice of metallic silver.

UV-induced synthesis of NPs is another important field wherein controlled growth of NPs can be achieved. Since the 19th century, silver salts, silver halides, have been used as photosensitive compounds for photography applications. In fact, their light exposure leads to the generation of metallic particles that were used in photography emulsion [**23**]. Thus, light radiation is a common way to synthesize silver colloids and NPs. Photoreduction occurs when photogenerated free electrons react with Ag^+ ions, forming the corresponding Ag^0 metal atom. Ag^+ ions in solution and efficient photogeneration are the main issues to control in order to have an effective production of Ag NPs. By changing precursors and electron donors, it is possible to control both the dimension and the shape of the NPs synthesized. One of the first syntheses of silver NPs in aqueous and alcohol solution was performed by Hada et al in the 1970s by ultraviolet (UV)-induced photoreduction using the photooxidation of water and alcohols under a deep-UV irradiation [**24**]. Nowadays, the most common used electron donors are aromatic ketones: they undergo cleavage under UV irradiation, producing radicals that induce reduction of silver [**25-27**].

3.3 Ex-Situ Ag Based RSD

Embedding highly conductive nanofillers in polymer is a common strategy for producing conducting polymer NCs. Silver conductive NCs were synthesized by

embedding silver NPs of different shapes in diverse matrices, such as high-density polyethylene [**28**], polymethyl methacrylate [**29**], polyvinyl alcohol [**30**], bisphenol F diglycidyl ether [**31**], polyvinylidene difluoride, and polydimethylsiloxane [**32**], but also in inks and conductive polymers, such as poly(3,4-ethylenedioxythiophene) [**33**].

The working mechanism of RSD based on ex-situ Ag NPs were studied. The active switching matrix in the present case is composed of ex-situ synthesized Ag NPs which is embedded in Polyvinylidene fluoride-hexafluoropropylene (PVDF-HFP). PVDF-HFP has a high dielectric constant, good mechanical strength and a high chemical stability [**34, 35**]. The presence of HFP in PVDF reduces its crystallinity, thus making it soluble in a wide range of solvents. The PVDF-HFP matrix acts as a quasi-solid medium for the silver ions, supporting their movements when an electric field is applied. The formulation is processed at room temperature, which is one of the foremost properties that allows the material to be deposited on the cheapest flexible substrates, including paper. The cheaper production method and the easy deposition technique along with the advantage of room temperature processing make these NCs very promising in the field of disposable devices.

3.3.1 Device Fabrication

The synthesis method of PVDF-HFP and Ag NP based switching matrix has been described in section **2.3.1**. The switching matrix synthesized by this direct solution method is deposited onto the planar symmetrical device (explained in section **2.2.1**) by means of 2 methods. Spin coating and InkJet printing.

3.3.1.1 RSD by Spin-Coat method

In the present case, the Ag NP based polymer switching matrix is spin coated onto the RSD at 3000RPM for 20 seconds. The coating process is performed at ambient temperature. The schematic representation of the figure is given in chapter 2 (**Figure 2.1)**. The simple two terminal Ex-Situ Ag NP and PVDF-HFP composite based RSD was initially made to undergo DC measurements which gave the most important information about the device like its forming, volatility, selectivity, working voltage range etc. **Figure 3.1** provides the initial forming which was observed in the device.

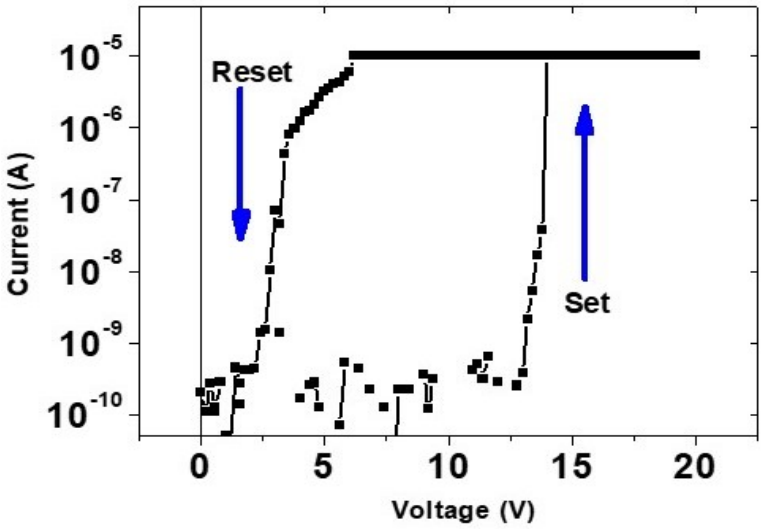

Figure 3.1: Initial electroforming process taking place at 13V [**38**].

The presence of an evident forming step (Transition from HRS to LRS) corresponds to a filament based switching in majority of the cases. Once the forming step is observed in the device, the further operating voltage range can be reduced (**Figure 3.2 a**). As explained in previous sections, the switching mechanism in our RSDs are explained by means of the formation of a metallic filament.

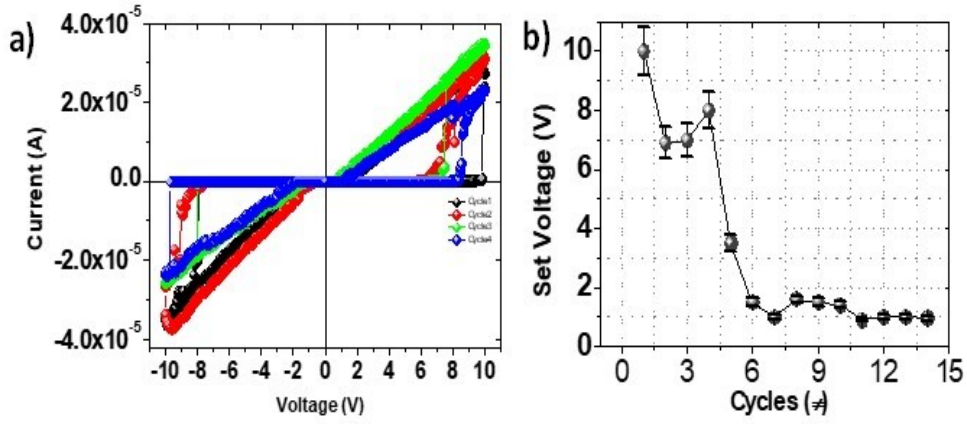

Figure 3.2: DC cycling after electroforming Process. a) Consecutive set process after electroforming. b) Variation in Set voltage with cycles

Initially, the pristine device is at its HRS. By the application of a forming field of 13 kV/cm, the device moves to its LRS. By providing such a high field the Ag NPs in the polymer switching matrix move in order to form a connected

filamentary path which bridges the Au electrodes. The usual forming voltage in stacked devices is much less compared to our case due to the much lower active switching gap seen in those devices. In the present case we have an active gap of 10 micro meter which makes the applied forming voltage also higher. Another reason for the increase in this voltage can be related to the outer shell PVP coating which is present on our Ag NPs. With a higher voltage, the PVP coating around the Ag NPs move and the particles move.

After the electroforming process, we observe the following set process takes place at a reduced field (9.8 KV/cm as in **figure 3.2**). This reduction in the set field can be explained by the already created conducting channel between the electrodes during forming process. The transition from LRS to HRS can be explained by the dissolution of the formed filament [**36**]. After the forming process, the filament penetrates into the polymer matrix creating a mechanical stress, which in turn creates a preferable channel or path between the electrodes even after the rupturing of the filament [**37**], thus the clear reduction in the set voltage with increased number of cycling can be observed in **figure 3.2 b**. It was found that the device behaviour had a strong dependence on the electrical characterization parameters set, especially on the current compliance level. Compliance current levels are generally set in order to ensure a safe operation of the device.

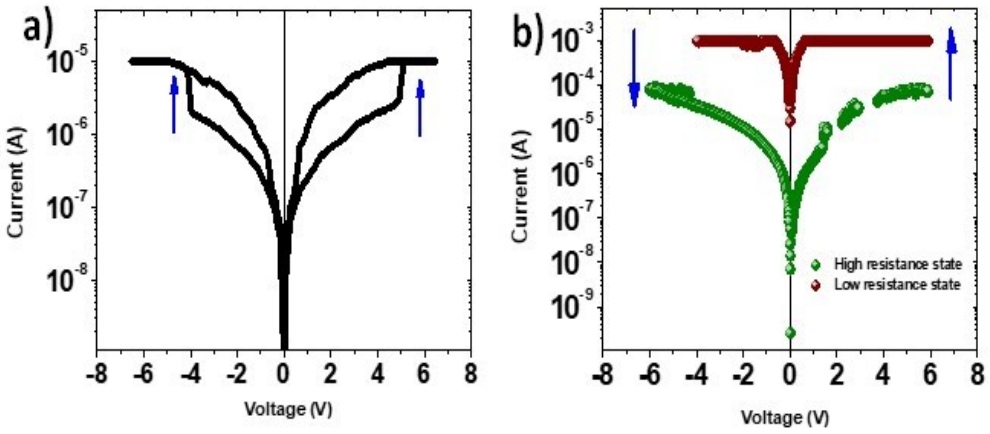

Figure 3.3: Electrical characterization performed on RSD. a) Cyclic IV performed on RSD in logarithmic scale at 10 µA current compliance. b) Cyclic IV performed on RSD in logarithmic scale at 1 mA current compliance **[38].**

The application of 10 µA compliance level was a reasonable current value that could be measured across the device by ensuring a continuous RS. It was

observed that in these operating conditions, the device behaved exactly like a random access memory (**figure 3.3 a**) in which the information was lost when the power was turned off. The device was set at 4.8 V, and then the device remained in its LRS until the voltage reached around 0.8 V. This behaviour continued in negative voltage range, where the device underwent a transition from HRS to LRS at around -4 V and back to HRS around -0.8 V. This volatile behaviour of the device can be explained by a non-continuous filament formed by the Ag NPs between the electrodes [**38**]. This volatile nature of the device can be attributed to the non-continuous filament formed between the electrodes. The On resistance in the volatile case is around 400 kΩ, which is more than the atomic point resistance (≈ 12.9 kΩ). Atomic point resistance is defined as the inverse of Quantum conductance (G0),

$$G0 = \frac{2e^2}{h} \approx 77\mu s \qquad (3.1)$$

In the above equation "h" corresponds to Planck's constant. Based on this Resistance based fact, we can infer one important point that if the On Resistance (R_{ON}) is above 12.9 kΩ, the RSD can be grouped under volatile memory device and the conduction can be attributed to tunnelling [**36**]. The reset process taking place in this case can be explained by the movement of the thermally induced Ag NPs from the non-continuous filament in order to attain its minimum interfacial energy [**39**]. **Figure 3.3 b** provides a non-volatile switching behaviour at a higher current compliance level of 1mA. As it can be observed, the device showed a non-volatile bipolar switching behaviour. The device was set at a voltage of around 6 V, and then maintained the On state until it reached the negative polarity. The device then moved to its HRS at around -4 V. The switching, in this case, can be explained by filamentary formation. The device, upon reaching its set voltage, led to Ag filament formation between the Ag NPs that were well dispersed in between the electrodes. This field induced filament was stable and remained between the electrodes even when the device moved through zero voltage. R_{ON} in this case is 4 kΩ, which is less than 12.9 kΩ. Thus according to the previous explanation, the non-volatility in this case can be explained by the value of R_{ON} which is less than the atomic point resistance. Based on the above obtained results we can state the finding by Liu et al [**36**], the conduction mechanism can be governed by tunnelling if $R_{ON} \geq 12.9$ kΩ and filamentary bridge state if $R_{ON} \leq 12.9$ kΩ. **Figure 3.4** provides the SEM and the optical microscope images of the switching gap of volatile and non-volatile case.

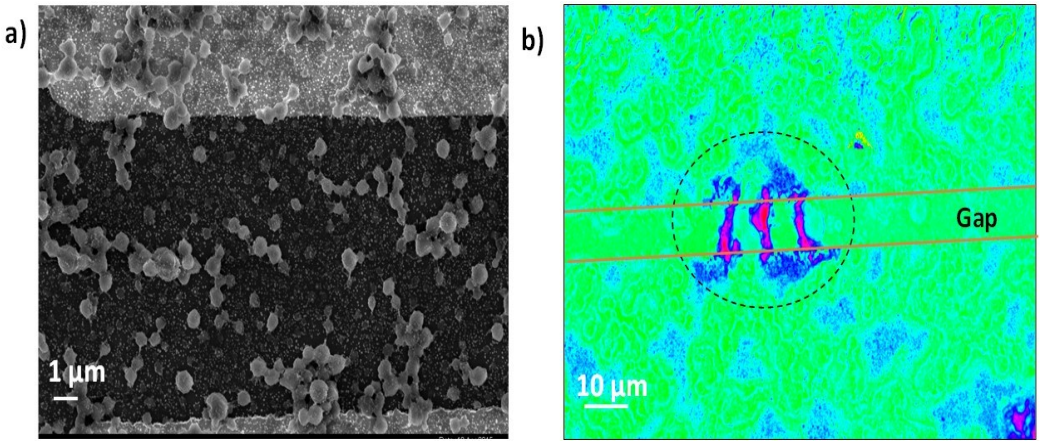

Figure 3.4: Optical characterization performed on the RSD a) FESEM image of the volatile characterized device b) Optical microscopy image of the characterized sample (non-volatile) after performing a mathematical algorithm to enhance the difference in the active gap before and after electrical characterization(The region between the orange lines constitute the active gap between the Au electrodes.) [**38**].

From the previous explanation, where the volatility of the device was explained by means of its $R_{ON,}$ the conduction mechanism was described by tunnelling. Thus considering **figure 3.4 a**, and the fact that the Ag NPs has clustered, we will explain the conduction mechanism in this case by tunnelling. Huang. X, et al [**40**] has conducted a similar study on Ag NP and PVDF based composite to assess the effect of tunnelling on conduction. Tunnelling model was used to explain the conduction [**41**].

Interparticle tunnelling conductivity σ_{tun} can be given as follows:

$$\sigma_{tun} \propto \exp\left(-\frac{l-2b}{d}\right) \qquad (3.2)$$

Where l is the average distance between the centres of the NPs, b is the average radius of the particles and d denotes the typical tunnelling range. It can be noted from the above equation that, as the interparticle distance increases, the conductivity decreases and vice versa. And hence the current in the LRS can be attributed due to tunnelling current through the unstable silver filament formed between the clusters of Ag NP. Now the reverse switching process (LRS to HRS) can be explained by the fact that as the applied electric field between the electrodes decreases, a thermally induced diffusion of Ag NPs takes place in order to diffuse to its minimum energy position near the terminals, which leads to a rearrangement of the conductive filament which finally leads to the movement of the device back to its initial HRS [**42**]. **Figure 3.4 b** represents the optical

microscope image of the non-volatile device which was taken after characterization. This particular image has been subjected to a mathematical algorithm to enhance the differences between two registered shots taken before and after electrical characterization [**43, 44**]. The geometrical registration process allows to compensate for the eventual little misalignments of the two shots; a histogram correction and a conversion to double floating point numbers assigns numerical values to each pixel and allows to algebraically sum the frames. The false colour scale reports stronger differences in red (green means no variation), evidencing the agglomeration of material in three filaments, bridging the Au electrodes.

In order to clearly state the effect of the set compliance on the RSD behaviour, the device was made to operate at different compliance currents (**Figure 3.5**).

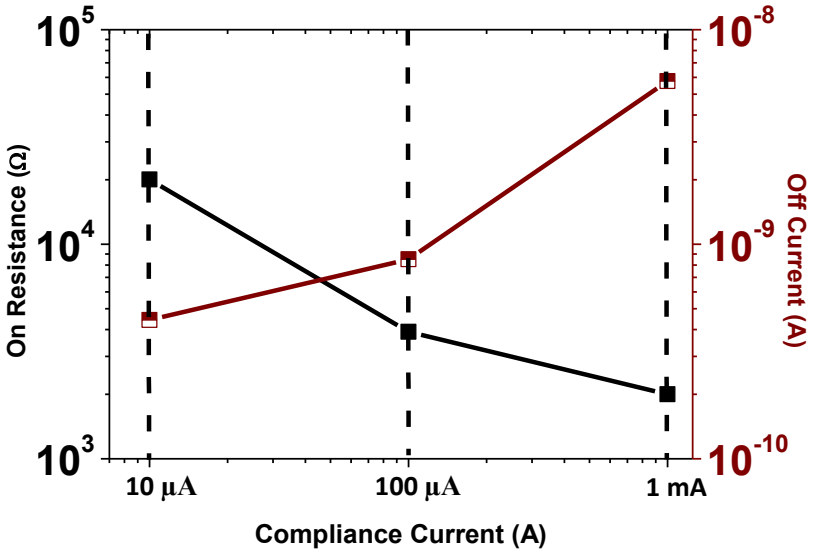

Figure 3.5: On Resistance and Off current plotted as a function of set Compliance current.

The device showed an increase in the Off state current with an increase in the set compliance, and a decrease in the On resistance with increasing set compliance. This relation is in accordance with the filamentary conduction model. As it can be seen from **figure 3.5** the Off current for compliances of 10 µA and 100 µA are not much different, this proves that there was no stable filament formation even with an increase in the compliance from 10 µA to 100 µA. Finally, with an increase in compliance to 1 mA, a stable and thick filament was formed, and thus, a higher reset or Off current was needed in order to break the formed filament. Thus we can generalise that a stable and thick filament leads to a

non-volatile device while a non-continuous not stable filament formed due to thermodynamically more reactive nature of the steady state nanoclusters leads to volatile nature of the device.

In order to check the stability of the non-volatile device, a pulse test was performed on the planar RSD. Pulse endurance test was performed on the sample by making the device undergo a set and reset process and thereafter probing it at a particular read voltage. The device was made to set by applying a voltage of +6 V and then read at +1 V. Similarly a reset voltage of –6 V was applied and was again probed at +1 V. **Figure 3.6** provides the result of the pulse endurance test performed on the device. The set, reset and the probing pulse had a time period of 500 µs. The device exhibited a very stable respone. An On/Off of about 65 was seen for about 60 cycles.

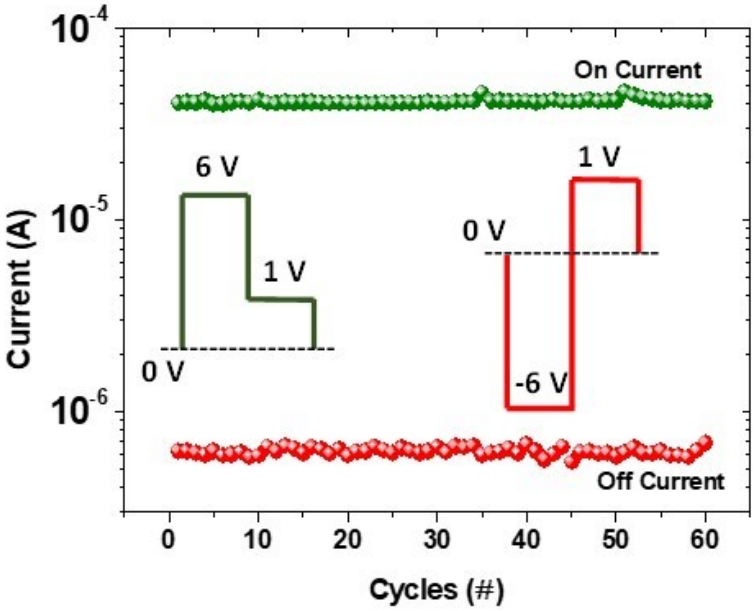

Figure 3.6: Pulse characterization performed on the non-volatile device.

The pulse endurance in this case is not high enough to consider a practical device. This is due to the planar structure with large switching gap (10 µm) of the device with symmetrical electrodes it has. Thus the spin coated RSD that is being presented here shows both volatile as well as non-volatile behaviour based on the current compliance set. A volatile switching behaviour can be related to short-term memory or working memory and a non-volatile switching behaviour can be related to long term memory in which the brain stores and retrieves information when needed.

The spin coated Polymer NC was actually found to be a bit non uniform in terms of its deposition thickness (**Figure 3.7**). Hence inkjet printing was the next technique used to deposit the switching matrix onto the planar RSD.

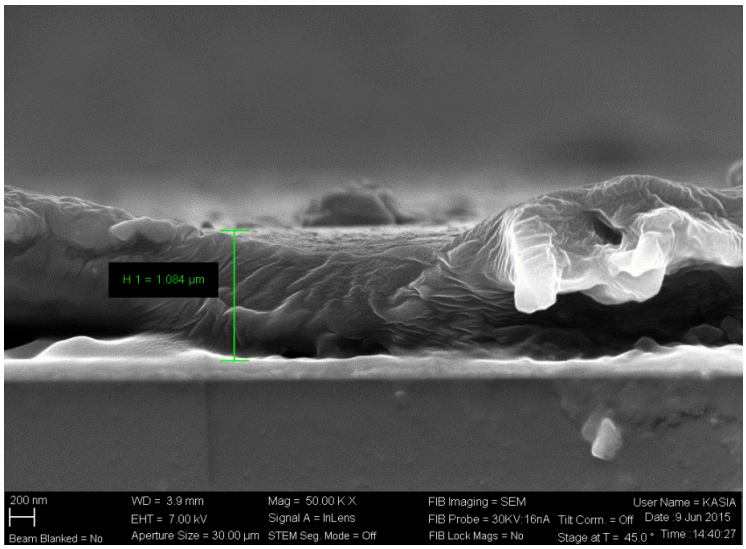

Figure 3.7: SEM image of the spin coated Ag and PVDF-HFP based switching matrix (side view) on the RSD

3.3.1.2 RSD by Ink-Jet printing method

As mentioned in section **2.4.2**, inkjet printing is a more sophisticated technology used to deposit materials onto a substrate. The printer used in our case is a piezoelectric inkjet printer whose general working mechanism has been explained in Chapter 2, Section **2.4.2**.

The printer used for our experiments is a Drop On Demand (DOD) inkjet printing system. The system is equipped with independent heaters for the printing, nozzle and the substrate. The piezoelectric nozzle is made of silica glass, with an orifice diameter of 60 µm. Printing was carried out at room temperature, the ink was stable at this temperature. The printed device was then dried at 35^0C in air for about 15 to 20 minutes. The ink used for printing is the Ag NP and PVDF-HFP based switching matrix. It was found that this switching matrix served as a very good ink with a viscosity of 8.5 cP which is usually a preferred value for piezoelectric inkjet printers [**13**]. As seen from **figure 3.8**, the present Ag NP and PVDF-HFP based ink exhibited a Newtonian fluid characteristic indicating a good stability under shear stress.

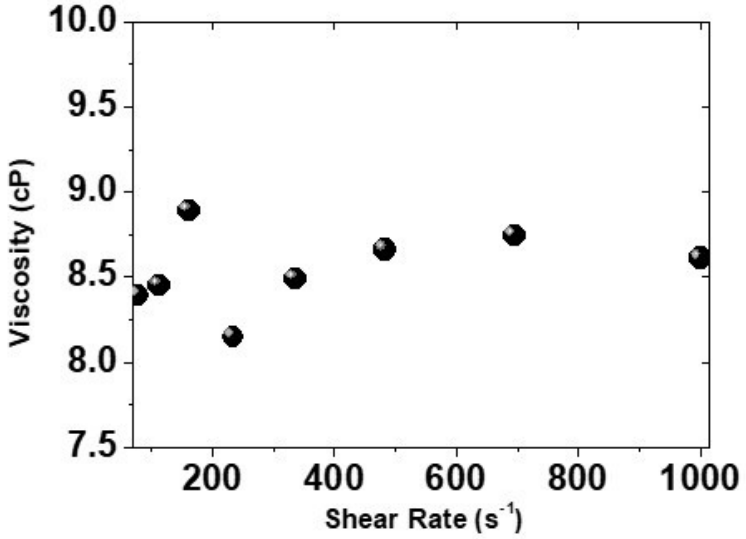

Figure 3.8: Viscosity measurement carried out on the Ag NP and PVDF-HFP based ink

In order to analyse the mechanics of the drop formation, the Z number was calculated using below equation:

$$Z = \frac{(d*p*S)^{0.5}}{V} \qquad (3.3)$$

Where, d, p, s and V are the orifice diameter, density of the liquid, surface tension and the viscosity respectively. The values corresponding to *d*, *p*, *S* and *V* are 0.000060 m, 1330 kg/m^3, 0.03512 N/m and 0.0086 Pa.s which leads to the final Z value of 6. The general acceptable Z value for DOD printing systems are greater than 2. Thus the Ag NC based switching ink can be considered apt for the piezoelectric inkjet systems. **Figure 3.9** shows a pictorial representation of the inkjet printed sample. Two different printing techniques were used in order to observe, if any, eventual effects were seen in the switching behaviour. Drop on position (DOP) and Print On Fly (POF) were the two techniques used. Both techniques are based on the same DOD principle, where a small volume of ink is ejected from the nozzle by applying a pressure pulse to the liquid ink in the channel [**45**]. DOP features a jetting performed dropwise onto a desired region offering the user a complete control over the number of drops and the exact location where the print has to be done (**Figure 3.9 a**). POF method on the contrary when executed, the pattern is printed on the sample in a continuous manner until the set pattern is complete (**Figure 3.9 b)**. In this type of printing,

pressure waves are created within the pressurized ink reservoir in response to continuous application of a periodically pulsed voltage stimulus. Thus as in the case of DOP, pressurization of the reservoir ensures a continuous jetting of the ink passing through the nozzle [**46**]. The major difference between these two modes of printing is that during a DOP job, both the print head and the stage are stationary while jetting. POF on the contrary involves the movement of the stage that moves continuously as a micro-drop is ejected at each array element [**47**].

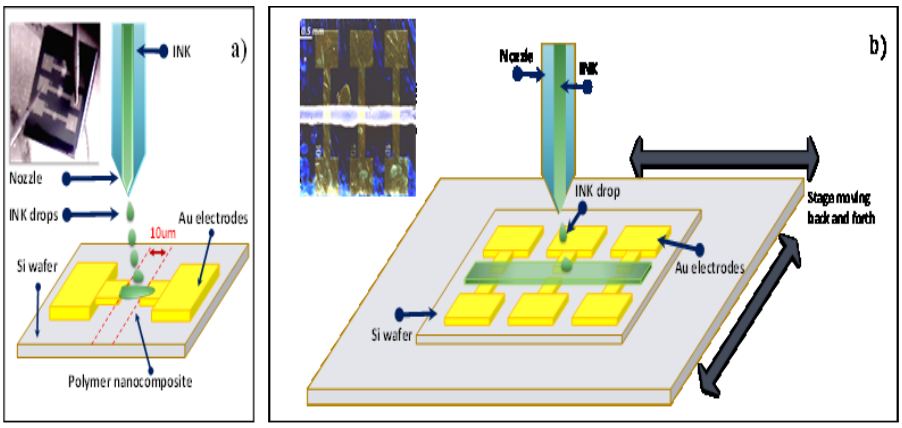

Figure 3.9: Schematic representation of the ink jet printed planar device using different techniques a) polymer NC being inkjet printed using DOP mode, inset: physical device after polymer NC printing and b) polymer NC being inkjet printed in POF mode, inset: physical device after Ag NC printing.

The device which was printed using the drop on position (DOP) technique will be mentioned as DOP RSD, and the other sample on which print on fly (POF) technique was used will be mentioned POF RSD. In the following section the electrical behaviour of DOP and POF RSD will be explained.

DOP RSD

As mentioned earlier, this technique involves the ejection of fixed number of ink drops at a desired position. A fixed amount of drops were ejected from the nozzle of the printhead onto the resistive switching active gap (between the gold electrodes).

The droplet density was set at 90 drops/mm^2 in the DOP RSD. Cyclic I-V measurements were performed on the sample in order to understand the switching behaviour. **Figure 3.10 a** illustrates the forming of the RSD. Application of an initial set or electroforming field of 32.5 kV/cm was needed to bring the pristine device to LRS. The application of such a high field favoured the movement of the

silver NPs that were dispersed into the polymer matrix, in order to make an electrical connection between the gold electrodes. As per the previous explanations regarding the dependence of electrical parameters and the device behaviour, in the present case as it can be seen from **figure 3.10 b,** at lower compliance the device behaved exactly as a random access memory in which the information was lost when the power was switched off. This diode like behaviour exhibited by the device (Volatile) had a set process around 1.2 kV/cm due to the formation of a non-continuous field induced silver filament between the electrodes. The reset process could be attributed to the destruction in the earlier conductive path, due to a thermally induced movement of silver atoms.

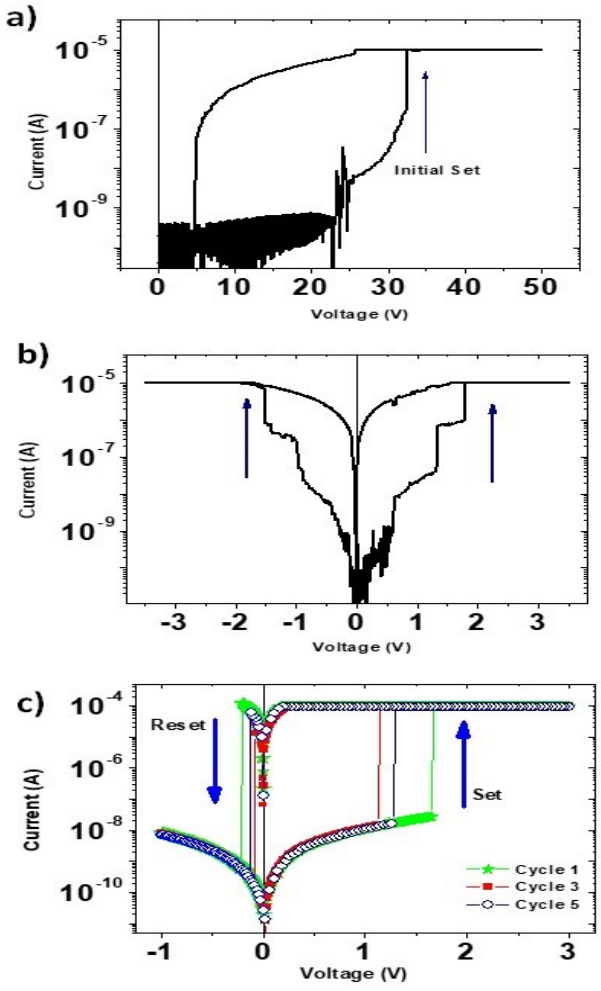

Figure 3.10: Electrical characterization performed on DOP RSD a) Initial electroforming at 32.5 V. b) Cyclic I-V performed on DOP in logarithmic scale at 10 µA set and reset current compliance. c) Cyclic I-V performed on DOP in logarithmic scale at 100 µA set compliance and 1mA reset compliance **[48].**

Despite the fact that the device was volatile, it can be observed from **Figure 3.10 b** that it maintained a rectifying ratio of 10^3 during the cyclic I-V characterization. The set process or the forming process can be induced by a high field activated process, while the reset can be attributed to high temperature (Joule heating). A further increase in set and reset compliance to 100 μA and 1 mA respectively, led to a complete change in the switching behaviour. **Figure 3.10 c** displays the I-V curve obtained after the cyclic I-V characterization performed on the sample at higher compliance. As it can be seen, the device showed a non-volatile bipolar switching behaviour. The device was set at a voltage of around 1.6 V, and then returned to HRS around -0.2 V. The device maintained a high On/Off current ratio of the order of 10^4 during the cyclic I-V characterization. The set process can be explained by the formation of a field induced Ag filament along the Ag clusters between the electrodes. A cyclic endurance test was performed on the sample (**Figure 3.11**) by probing the device at 0.5 V after setting and resetting the device at +2V and -2V respectively. The set, read and write pulses were 30 ms long. The device exhibited an average set resistance state of about 10^6 Ω and a reset resistance state of 10^8 Ω. Thus maintaining an R_{Off}/R_{On} of about 10^2 for about 45 cycles. The On and Off resistance values of pulse measurement cannot be compared to the cyclic IV measurements. Because in pulse mode the measurement is performed in dynamic regime (pulse period of 30 ms) which introduces an inductive effect, leading to a higher set and reset resistance.

Figure 3.12 a displays the silver NPs dispersed in the PVDF-HFP matrix between the Au electrodes of an electrically characterized sample. As it can be seen the silver cluster creates a conductive path between the Au electrodes. **Figure 3.12 b** represents the differential optical microscope image of the same sample which is being characterized.

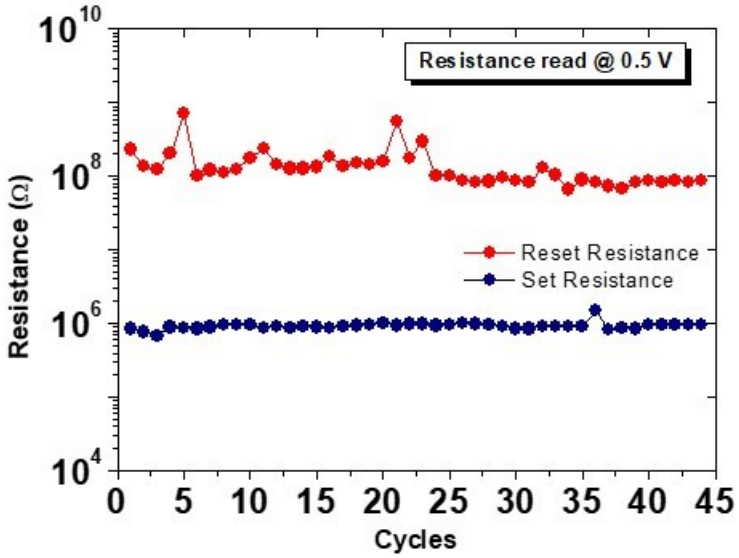

Figure 3.11: Pulse characterization performed on the non-volatile device.

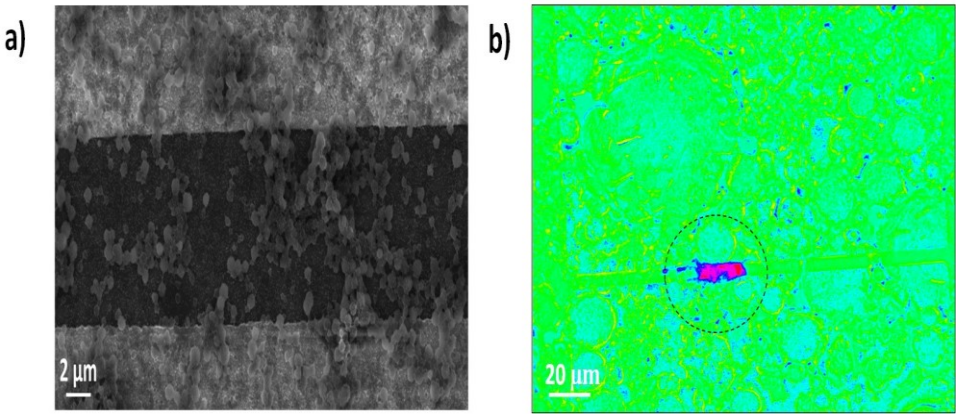

Figure 3.12: optical characterization performed on DOP RSD a) FESEM image of the device with active switching matrix inkjet printed between the gold electrodes, after electrical characterization b) Optical microscopy image of the characterized sample after false colour mapping **[48].**

The Ag NP and PVDF-HFP based ink was found to be affected by ageing. XPS measurement performed on a 6 month old device showed that the Ag was oxidised which led to an inferior performance of the RSD. **Figure 3.13** provides the peaks corresponding to Ag $3d_{5/2}$ and Ag $3d_{3/2}$, the doublets corresponding to 3d orbital. The chemical positioning of the peaks corresponding to Ag metal and AgO along with the rough estimate of the area in which they are present are provided in the XPS plot. As it can be seen, only 87.8% of metallic silver was present on the surface while remaining 12.2% was in its oxidized state. This

oxidation effect on the Ag NP led to a drastic change in the device electrical behaviour. The oxidation effect on the silver NPs led to an addition to the resistance of the RSD (Inset **Figure 3.13**) and a higher electric field of nearly 8 kV/cm, which is 6 times higher than the field was needed for the switching.

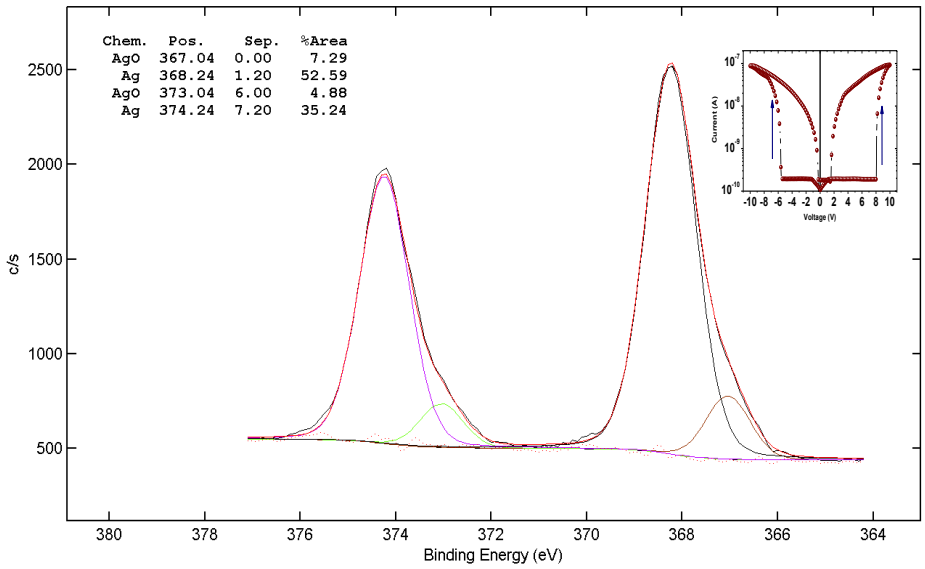

Figure 3.13: High-Resolution survey on Ag^{3d} spectrum of the aged DOP RSD. Inset provides the electrical characterization result carried out on the aged device

POF RSD

POF printing technique is defined by setting a printing pattern, and once the print command is executed, the set pattern is printed on the substrate under continuous droplet generation. In our work we have printed several patterns and one of the best results were obtained by printing a rectangular array of 6.5×0.5 mm (Inset of **Figure 3.9 b**). The array was printed such that 93 drops were ejected on a single line. A total of 558 drops were ejected as 6 lines were printed in the rectangular array. Thus in the POF case, we can generalise the presence of 172 drops/mm^2 which is twice as that in DOP RSD. This kind of printing resulted in a Write Once Read Many (WORM) type of RSD [**49**], where once the device was switched on, it maintained the ON state even after the reduction of the applied field. **Figure 3.14 a** shows the high field transition of the device from HRS to LRS. It can also be noted from **figure 3.14 b**, that in the initial voltage sweep from 0 V to higher positive voltage, the device was found to be at HRS, but as the voltage reached 25 V, there was a further decrease in the current level, which was maintained till 45V, and then the entire device took its transition to LRS around

50 V. This instability in the HRS can be explained by the complexity in the available conductive paths between the electrodes. Once the device reached its LRS, it maintained its high conducting state until it reached a lower positive voltage where it again had a transition to HRS. This state was continued until -15 V was reached, where the device made its final transition to LRS. The device then had no further transitions. An LRS was maintained for further applied fields.

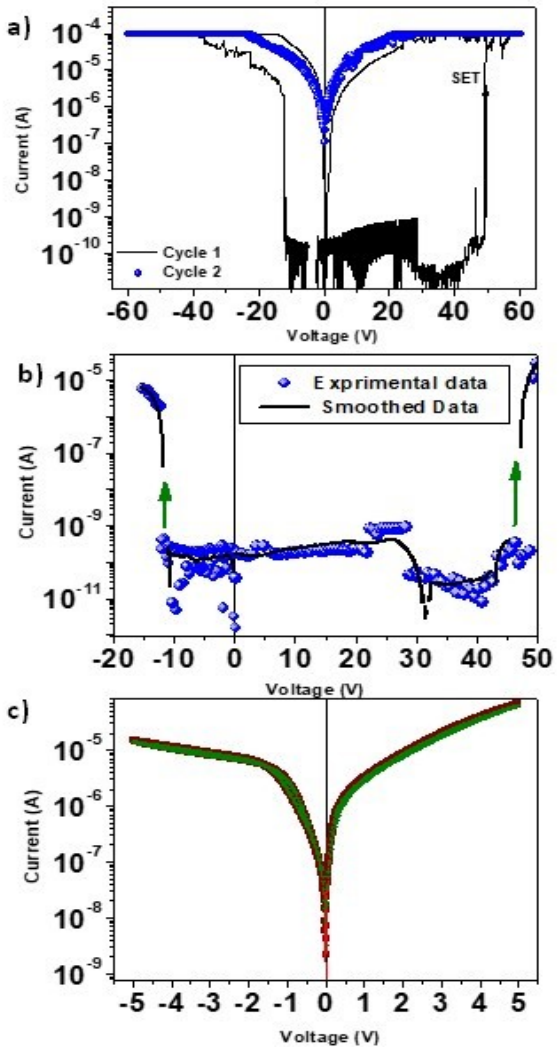

Figure 3.14: Electrical characterization performed on POF RSD a) Initial Cyclic I-V measurement on the device. b) Plot showing the HRS of the first cycle in both polarities (continuous line showing smoothing by means of Savitzky-Golay filter). c) I-V measurement carried out at reduced voltage range

To confirm the WORM behaviour, the voltage range was further decreased (**figure 3.14 c**), and it was observed that the device maintained its LRS. This permanent On state of the device can be explained by the formation of multiple conducting filaments or a highly conducting percolative path. While in the DOP RSD, limited filaments in the order of 1 or 2 gave rise to the conduction. The ageing effect was tested in this case. It was observed that initially the switching gap of the RSD was undisturbed (**Figure 3.15 a**). After electrical characterization which was performed at high fields and the device unlike other POF RSD didn't exhibit WORM behaviour (**Figure 3.15 b**), it was seen that the electrode was displaced. As it can be seen from **figure 3.15 c**, the Au was displaced from the edge of the electrodes, thus increasing the effective switching gap. This migration of Au is induced by electro migration happening due to the presence of high field which is stressing the device each and every time the cycling voltage is applied. This destruction in the electrodes happen only with ageing and application of high field in order to switch the device.

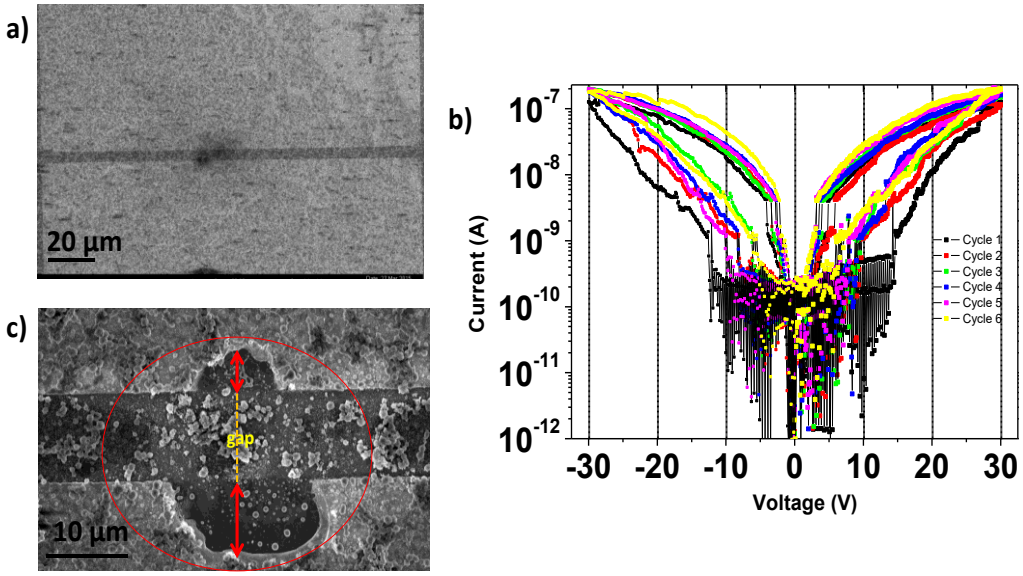

Figure 3.15: Tests performed on aged POF RSD a) SEM image before characterization b) Electrical characterization performed on the aged device. c) SEM imaging performed after characterization

The difference in switching behaviour observed in DOP RSD and POF RSD can be explained by means of a simple schematic representation (**Figure 3.16**).

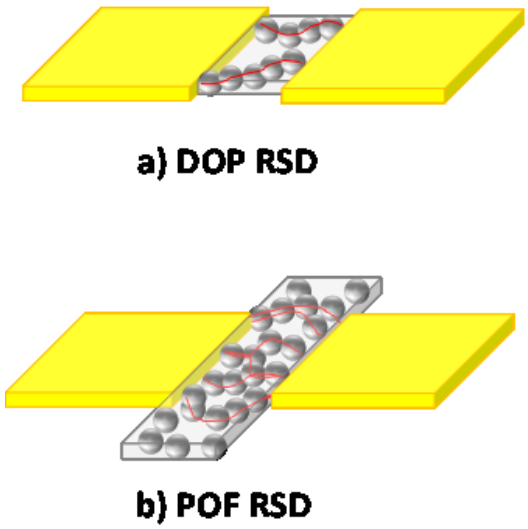

Figure 3.16: Schematic representation of the active gap between the electrodes of a) DOP RSD and b) POF RSD **[48].**

As seen from **figure 3.16 a**, the number of conductive paths in the case of DOP RSD is much less than in the case of POF RSD. The probability of having multiple conductive paths in POF RSD is high (**Figure 3.16 b**). This causes a higher electroforming voltage in the case of POF RSD. In POF RSD as it can be seen from **figure 3.16 b**, there can be conductive filaments not just in the active switching gap, but also due to complex fractal dendritic geometries followed by NPs throughout the printed matrix. This was observed in many similar systems [**3**].

We can generalize the resistive switching (regardless of the switching matrix deposition technique) that we saw in all these cases using Ag NPs and PVDF-HFP as field induced filamentary process. By using a planar device structure, the set field applied is high since the conductive filament has to cover a larger distance. **Figure 3.17** provides the schematic representation of the field induced switching mechanism of the RSD. The pristine state of the device has the switching matrix in which the Ag NPs are dispersed in the polymer matrix. The pristine state of the device is in its HRS. Once a particular set threshold field is applied the dispersed Ag NPs move thus causing a metallic filament like connection which bridges the adjacent NP clusters, leading to a percolative network thus reducing the bulk resistivity of the device [**42**].

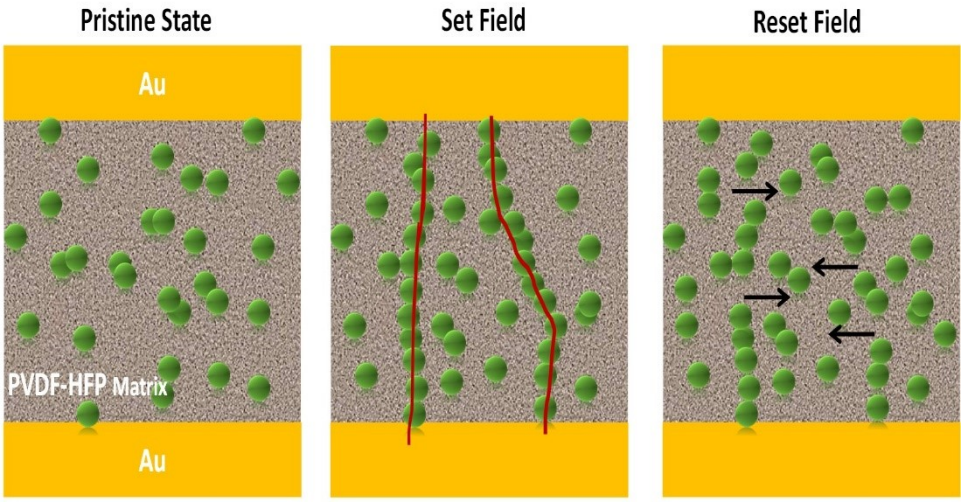

Figure 3.17: Schematic representation of field induced filament formation and destruction in Ex-Situ based RSD. Green circles represents the Ag NPs

Once the field reaches its reset threshold, the NPs present in the connected filament moves due to thermal disordering and leads to the rupturing of the filament and leads to its initial HRS. The transition of the device from LRS to HRS in the case of volatile device (Low compliance) can be explained as follows: As the field decreases and it goes to 0, the temperature drops as well as the NPs slowly starts to diffuse to its minimum energy position near the terminals. Finally most of the NPs might have merged to larger clusters signifying the effect of Ostwald ripening or in other words to minimize their interfacial energy [**50**]. While with higher compliance, the formed filament is strong enough that the NPs remain connected even at 0 bias. The device moves to HRS only when the field reaches a reset threshold in opposite polarity during which the NPs diffuse from their connected path due to thermal disordering.

From the experiments conducted on EX-Situ Ag NPs and PVDF-HFP based switching matrix, we can summarize that the switching matrix when used on planar symmetrical device led to resistive switching which strongly depends on electrical parameters set. The mechanism behind the switching was found to be filamentary which was supported by the FESEM imaging and the compliance dependence switching. The device performance (endurance) was not commendable due to the fast oxidising nature of the Ag NPs present in the switching matrix. The work was then carried forward by synthesizing the Ag NPs by In-Situ method

3.4 In-Situ Ag Based RSD

So far we have explained Ex-situ based RSD. A small part of my work was also made on developing In-situ based RSD. As mentioned previously, in Ex-situ synthesis the active fillers are directly added to the polymer matrix, while in In-situ method, the NPs are grown from the precursors which are embedded inside the polymer matrix. Even though the Ex-situ method has the advantage of better control over the NP size and distribution, In-situ method has the advantage of a better NP distribution within the matrix.

Here the In-situ growth of nanostructures is used to develop an innovative strategy for customizing the electric properties of the corresponding RSD NC material. As explained in chapter 2 section **2.3.2** we have synthesized a switching matrix in which the Ag NPs has been generated by photo curing process. The RSD used in this case is also different from the earlier discussed planar symmetrical devices. The stacked structure here allows to have a smaller active switching gap. The general switching behavior of the in-situ based RSD was studied is a brief manner.

DC analysis was performed on the stacked asymmetrical device (**Figure 2.2**) to study its switching characteristics. Active bias in this case was provided to ITO electrode (**Figure 2.14**). It was observed that the device exhibited a non-volatile resistive switching behavior.

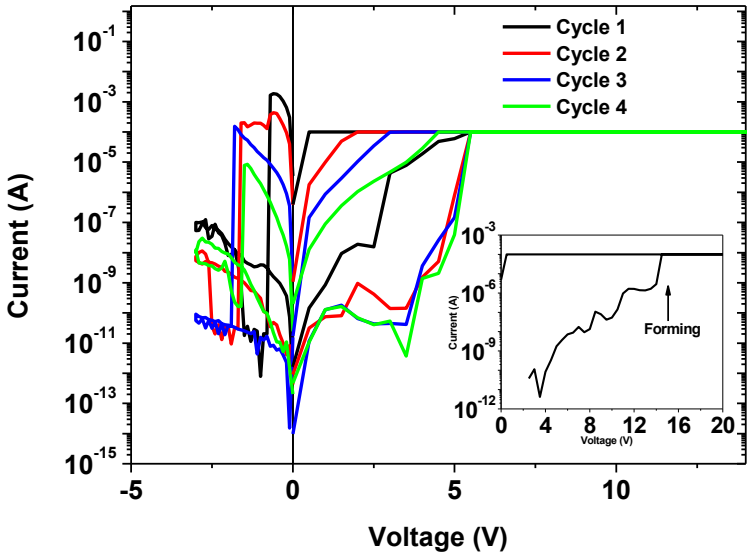

Figure 3.18**:** DC characterization performed on In-Situ based RSD. Inset provides the electroforming process.

As seen from inset of **figure 3.18** the device had its forming process at nearly 14V, and then there was a reduction in the following set process. The in-situ based device showed an On/Off of about 10^4 to 10^5. But this ratio was not stable. By increased number of switching cycles, the device was moving towards a low conducting state. And thus we saw a reduction in the On/Off. The switching mechanism in in-situ generated Ag NP composite based RSD can be explained as in previous Ex-situ case. Since the polymer matrix used in this case is similar as in previous Ex-situ case, and since we have the set case which reaches the compliance level, we can explain the switching in this case due to a field induced filamentary formation. The application of a set field causes the Ag NPs in the polymer matrix to move and form an interconnected network like path between the electrodes which causes the conduction. This leads to a strong and stable filament which can be ruptured or dissolved by the application of a reverse polarity. But with more cycling's, the conductive On-state prevails for longer time period and the filaments become more stable and robust, which makes the recovery of the insulating state or the HRS of the polymer NC not possible.

3.5 References

1. Roppolo, I.; Bozzo, A. D.; CAstellino, M.; Chiappone, A.; Perrone, D.; Bejtka, K.; Bocchini, S.; Chiolerio, A. (2016). Dual step irradiation process for in situ generation and patterning of silver nanoparticles in a photocured film. *RSC Advances*, 6, pages 14832-14843.

2. Ajayan, P. M.; Schadler, L. S.; Braun, P. V. (2003). Polymer based and polymer filled nanocomposites. Nanocomposite Science and Technology (P. 77-153) John Wiley & Sons.

3. Chiolerio, A.; Sangermano, M. (2012). In situ synthesis ofAg-acrylic nanocomposites: tomography based percolation model, irreversible photoinduced electromigration and reversible electromigration. *Mateials Science and Engineering B,* 177, pages 373-380.

4. Jain, P. K.; Huang, X.; Sayed, I. H.; Sayed, M. A. (2007). Review of some interesting surface plasmon resonance-enhanced properties of noble metal nanoparticles and their applications to biosystems. *Plasmonics*. 2, Pages 107–118.

5. Willets, K. A.; Van Duyne, R. P. (2007). Localized surface plasmon resonance spectroscopy and sensing. *Annual Review of Physical Chemistry,* 58, pages 267–297.

6. Qi, W. H.; Wang, M. P. (2004). Size and shape dependent melting temperature of metallic nanoparticles. *Materials Chemistry and Physics*, 88, pages 280–284.

7. Meng, X. K.; Tang, S. C.; Vongehr, S. (2010). A review on diverse silver nanostructures. *Journal of material science and Technology,* 26, pages 487–522.

8. Wiley, B.; Sun, Y.; Mayers, B.; Xia, Y. (2005). Shape-controlled synthesis of metal nanostructures: the case of silver. *Chemistry*. 11, Pages 454–463.

9. Jain, P. K.; Huang, X.; Sayed, I. H.; Sayed, M. A. (2008). Noble metals on the nanoscale: optical and photothermal properties and some applications in imaging, sensing, biology, and medicine. *Accounts of Chemical Research,* 41, pages 1578–1586.

10. Shen, X. S.; Wang, G. Z.; Hong, X.; Zhu, W. (2009). Nanospheres of silver nanoparticles: agglomeration, surface morphology control and application as SERS substrates. *Physical Chemistry Chemical Physics,* 11, pages 7450–7454.

11. Sau, T. K.; Rogach, A. L.; Jackel, F.; Klar, T. A.; Feldmann, J. (2010). Properties and applications of colloidal nonspherical noble metal nanoparticles. *Advanced Materials,* 22, pages 1805–1825.

12. Li, X. (2015). "Wet" chemical synthesis and manipulation of upconversion nanoparticles. *Photon Upconversion Nanomaterials*. (P. 21-71) Heidelberg: Springer.

13. Rajan, K.; Roppolo, I.; Chiappone, A.; Bocchini, S.; Perrone, D.; Chiolerio, A. (2016). Silver nanoparticle ink technology: state of the art. Nanotechnology Science and Applications, 9, pages 1-13.

14. Iravani, S. (2011). Green synthesis of metal nanoparticles using plants. *Green Chemistry,* 13, pages 2638–2650.

15. Guzmán, M. G.; Dille, J.; Godet, S. (2009). Synthesis of silver nanoparticles by chemical reduction method and their antibacterial activity. *International Journal of Chemical and Biomolecular Engineering,* 2, pages 105–111.

16. Chou. K. S.; Ren, C. Y. (2000). Synthesis of nanosized silver particles by chemical reduction method. *Materials Chemistry Physics,* 64, pages 241–246.

17. Liu, Y. C.; Lin, L. H. (2004). New pathway for the synthesis of ultrafine silver nanoparticles from bulk silver substrates in aqueous solutions by sonoelectrochemical methods. *Electrochemistry Communications,* 6, pages 1163–1168.

18. Sandmann, G.; Dietz, H.; Plieth, W. (2000). Preparation of silver nanoparticles on ITO surfaces by a double-pulse method. *Journal of Electroanalytical Chemistry*, 491, pages 78–86.

19. Mallick, K.; Witcomb, M. J.; Scurrell, M. S. (2005). Self-assembly of silver nanoparticles in a polymer solvent: formation of a nanochain

through nanoscale soldering. *Materials Chemistry Physics,* 90, pages 221–224.

20. Zhu, J.; Liu, S.; Palchik, O.; Koltyoin, Y.; Gedanken, A. (2000). Shape-controlled synthesis of silver nanoparticles by pulse sonoelectrochemical methods. *Langmuir*, 16, Pages 6396–6399.

21. Dong, C.; Zhang, X.; Cai, H.; Cao, C. (2014). Facile and one-step synthesis of monodisperse silver nanoparticles using gum acacia in aqueous solution. *Journal of Molecular Liquids,* 196, pages 135–141.

22. Xia, Y.; Xiong, Y.; Lim, B.; Skrabalak, S. E. (2009). Shape-controlled synthesis of metal nanocrystals: simple chemistry meets complex physics? *Angewantde Chemie International Edition,* 48, pages 60–103.

23. Barbieri, A.; Accorsi, G.; Armaroli, N. (2008). Luminescent complexes beyond the platinum group: the d^{10} avenue. *Chemical Communications,* 0, pages 2185–2193.

24. Hada, H.; Yonezava, Y.; Yoshida, A.; Kurakake, A. (1976). Photoreduction of silver ion in aqueous and alcoholic solutions. *Journal of Physical Chemistry,* 80, pages 2728–2731.

25. Sato, T.; Onaka, H.; Yonezava, Y. (1999). Sensitized photoreduction of silver ions in the presence of acetophenone. *Journal of Photochemistry and Photo Biology A: Chemistry*. 127, Pages 83–87.

26. Itakura, T.; Torigoe, K.; Esumi, K. (1995). Preparation and characterization of ultrafine metal particles in ethanol by UV irradiation using a photoinitiator. *Langmuir*. 11, Pages 4129–4134.

27. Esumi, K.; Matsumoto, T.; Seto, Y.; Yoshimura, T. (2005). Preparation of gold-, gold/silver-dendrimer nanocomposites in the presence of benzoin in ethanol by UV irradiation. *Journal of Colloid and Interface Science,* 284, pages 199–203.

28. Rybak, A.; Boiteux, G.; Melis, F.; Seytre, G. (2010). Conductive polymer composites based on metallic nanofiller as smart materials for current limiting devices. *Composite Science Technology,* 70, pages 410–416.

29. Kim, W. T.; Jung, J. H.; Kim, T. W.; Son, D. I. (2010). Current bistability and carrier transport mechanisms of organic bistable devices based on hybrid Ag nanoparticle-polymethyl methacrylate polymer nanocomposites. *Applied Physics Letter,* 96, pages 253301–253303.

30. Mahendia, S.; Tomar, A. K.; Kumar, S. (2010). Electrical conductivity and dielectric spectroscopic studies of PVA-Ag nanocomposite films. *Journal of Alloys and Compounds,* 508, pages 406–411.

31. Zhang, R.; Moon, K.; Lin, W.; Wong, C. P. (2010). Preparation of highly conductive polymer nanocomposites by low temperature sintering of silver nanoparticles. *Journal of Material Chemistry,* 20, pages 2018–2023.

32. Chun, K. Y.; Oh, Y.; Rho, J.; Ahn, J. H.; Kim, Y. J.; Choi, H. R.; Baik, S. (2010). Highly conductive, printable and stretchable composite films of carbon nanotubes and silver. *Nature Nanotechnology,* 5, pages853–857.

33. Pudas, M.; Hagberg, J; Leppavuori. (2004). Gravure offset printing of polymer inks for conductors. *Progress in Organic Coatings,* 49, pages 324–335.

34. Wu, F.; Feng, T.; Bai, Y.; Wu, C.; Ye, L.; Feng, Z. (2009). Preparation and characterization of solid polymer electrolytes based on PHEMO and PVDF-HFP. *Solid State Ionics*, 180, pages 677-680.

35. Ataollahi, N.; Ahmad, A.; Hamzah, H.; Rahman, M. Y. A.; Mohamed, N. S. (2012). Preparation and characterization of PVDF-HFP/MG49 based polymer blend electrolyte. *International journal of electrochemical science*, 7, pages 6693 – 6703.

36. Liu, D.; Wang, N.; Wang, G.; Shao, Z.; Zhu, X.; Zhang, C.; Cheng, H. (2013). Nonvolatile bipolar resistive switching in amorphous Sr-doped LaMnO3 thin film deposited by radio frequency magnetron sputtering. *Applied Physics Letter,* 102, *134105*.

37. Valov, I.; Waser, R.; Jameson, J. R.; Kozicki, M. N. (2011). Electrochemical metalization memories- Fundamentals, application prospects. *Nanotechology*, 22, 289502.

38. Rajan, K.; Bocchini, S.; Chiappone, A.; Roppolo, I.; Perrone, D.; Bejtka, K.; Ricciardi, C.; Pirri, C. F.; Chiolerio, (2017). Spin-coated silver nanocomposite resistive switching devices. *Microelectronic Engineering*, 168, pages 27-31.

39. Sandouk, E. J.; Gimzewski, J. K.; Steig, A. Z. (2015). Multistate resistive switching in silver nanoparticle films. *Science and Technology of Advanced Materials*, 16, pages 1-7.

40. Huang, X.; Jiang, P.; Xie, L. (2009). Ferroelectric polymer/silver nanocomposites with high dielectric constant and high thermal conductivity. *Applied Physics Letter*, 95, *242901*.

41. Rubin, Z.; Sunshine, S. A.; Heaney, M. B.; Bloom, I.; Balberg, I. (1999). Critical behaviour of the electrical transport properties in a tunnelling percolation system. *Physical Review B,* 59, 12196.

42. Mutiso, R. M.; Kikkawa, J. M.; Winey, K. I. (2012). Resistive switching in silver/Polystyrene/silver nano-gap devices. *Applied Physics Letter*, 103, 223302.

43. Chiolerio, A.; Allia, P. (2012). Towards a quantitative analysis of magnetic force microscopy data matrices. *Journal of Magnetism and Magnetic Materials,* 324, pages *2416*-2428.

44. Chiolerio, A.; Celasco, E.; Celegato, F.; Guastella, S.; Martino, P.; Allia, P.; Tiberto, P.; Pirri, C. F. (2008). Enhanced imaging of magnetic structures in micropatterned arrays of Co dots and antidots. *Journal of Magnetism and Magnetic Materials,* 320, pages 669-673.

45. Dong, H.; Carr, W. W. (2006). An experimental study of drop-on-demand formation *Physics of Fluids.* 18, 072102-16.

46. Zhang, Y.; Liu, C.; Whalley, D. C. (2009). Direct-Write Techniques for Maskless Production of Microelectronics: *A Review of Current State-of-the-art Technologies International conference on electronic packaging technology and high density packaging,* 09, Pages 497-*503.*

47. Holthoff, E. L.; Farrell, M. E.; Pellegrino, P. M. (2013). Standardized Sample Preparation Using a Drop-on-Demand Printing Platform. *Sensors,* 13, pages 5814-5825.

48. Rajan, K.; Bocchini, S.; Chiappone, A.; Roppolo, I.; Perrone, D.; Castellino, M.; Bejtka, K.; Lorusso, M.; Ricciardi, C.; Pirri, C. F.; Chiolerio, A. (2017). WORM and bipolar inkjet printed resistive switching devices based on silver nanocomposites. *Flexible and Printed Electronics*, 2, 024002.

49. Mo¨ller, S.; Perlov, C.; Jackson, W.; Taussig, C.; Forrest, S. R. (2003). A polymer/semiconductor write-once read-many-times memory *Nature,* 426, pages 166-169.

50. Wang, Z.; Joshi, S.; Savelev, S. E.; Jiang, H.; Midya, R.; Lin, P.; Hu, M.; Ge, N.; Strachan, J. P.; Li, Z.; Wu, Q.; Barnell, M.; Li, G. L.; Xin, H. L.; Williams, S. R.; Xia, Q.; Yang, J. J. (2017). Memristors with difusive dynamics as synaptic emulators for neuromrphic computing. *Nature Materials*, 16, pages 101-108.

Chapter 4

Ionic Liquid embedded Fluoro polymer composite based RSDs

4.1 Introduction

Metallic salts especially $AgNO_3$ are commonly used as precursor to many Ag compounds. The use of $AgNO_3$ instead of commercial Ag NPs makes the experimental process less expensive.

The presence of polymer and metal ions that can be easily reduced by applying a voltage is used as switching matrix in many case studies. In the recent research carried out, Ionic Liquid (IL) is incorporated in the polymer and $AgNO_3$ based switching matrix. IL increases the ionic conductivity by increasing the mobility of the metal ions. RSDs with presence of Silver salt and IL fall under REDOX based resistive switching memory [**1**]. IL are usually used as nonvolatile liquid electrolytes (liquids with low vapour pressure) in electrochemical applications [**2, 3**] due to their excellent electrochemical stability and high ionic mobility which makes them good electrolytes. Part of the work described in this chapter has been previously published in "*RSC Advances, 6, 2016, (94128).*"

4.2 Planar symmetrical device based on PVDF-HFP_$AgNO_3$_IL

The use of $AgNO_3$ as a precursor for the NP generation has been studied in Chapter 3, section **3.4**. While in this chapter we are not performing any direct

photo reduction process on the polymer switching matrix. The matrix used in this section is discussed in chapter 2**,** section **2.3.3**. In this subchapter we will discuss about the electrical behavior and mechanism of the planar symmetrical device (mentioned in chapter 2**,** section **2.2.1**).

The switching matrix was spin coated onto the device at ambient condition. Before discussing about the switching matrix with IL, a small test was also conducted where the matrix was composed just with PVDF-HFP and $AgNO_3$ (wt% of PVDf-HFP/$AgNO_3$ 95/5). This test was performed to clearly understand the importance of the addition of IL into our polymer NC based matrix.

The switching matrix based on PVDF-HFP_$AgNO_3$ was coated onto the planar symmetrical device and was electrically characterized. **Figure 4.1** provides the electrical characterization results. The pristine device was found to be at HRS. As it can be seen from **Figure 4.1a** the RSD had its initial transition from high resistance state (HRS) to low resistance state (LRS) at a negative voltage, around -25 V, which corresponds to about 25 kV/cm. The current limit has been clamped to 100 µA in both polarities to ensure the safe functioning of the device. The initial *set* process happening in the present case can be easily explained by a simple reaction where the Ag^+ ions are being reduced to Ag^0 atoms, which relates to the change in the resistance state of the device from high to low. Since we are not inducing the reduction of the Ag ions by any external means, the probable reaction happening here will be the direct oxidation of oxygen that replaces nitrate in the dissolution of $AgNO_3$ in PVDF-HFP. Thus, the total conduction current can be attributed to the contribution of 1) ionic conduction before switching and 2) filamentary electronic conduction after switching. The present RSD considered had a decrease in its switching voltage from -25 V to lower values, in the range of 20 V after the initial switching (**Figure 4.1 b**).This is because the forming process can be regarded as a soft breakdown happening in the switching matrix. This means that the process can be partly reversed by an electrical stimulus. Complex processes might take place during the breakdown like ionic and electronic process which are often mediated by Joule heating and thermal rearrangement. The device was always exhibiting a unipolar or Random Access Memory (RAM) behavior. This is obviously due to the creation of a thin and unstable filament which was not able to persist in the active switching gap when the power was switched off. This reasoning can be proven by 2 facts. One being, the ON resistance observed in **figure 4.1 b** exceeds 100 kΩ that is much higher than the resistance of a single atomic point (12.9 kΩ), leading to the assumption that the volatile behavior observed is due to a dominant electron tunneling process [**4**]. Secondly, **figure 4.1**

c provides the FESEM image of the active gap after characterization. As seen, the Ag NPs are homogeneously distributed within the matrix, between the gold electrodes, and that there is no evidence of filament formation between the electrodes after cyclic I-V characterization.

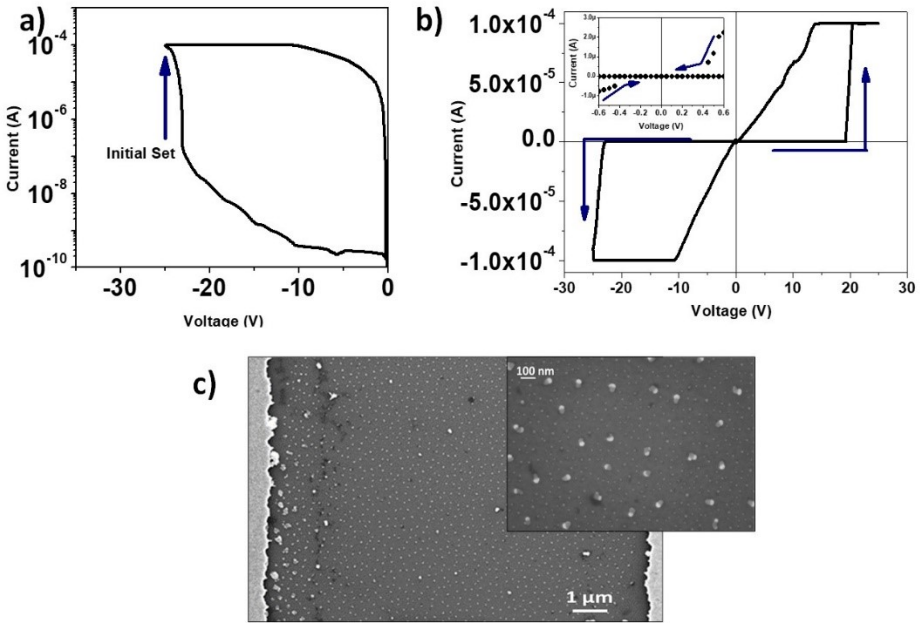

Figure 4.1: Electrical characterization performed on the planar symmetrical device. a) Initial set taking place at -25V. b) Complete cyclic IV measure. Inset provides Zoom near -0.6 to +0.6 V, to understand the transition from LRS to HRS in both polarities. c) FESEM image of the device with active switching matrix spin coated between the gold electrodes, after electrical characterization, inset: Magnified portion between the electrodes.

Since the present switching matrix was not able to induce a memory effect, nor was this matrix able to perform well as a unipolar device with a good endurance, the matrix was modified by adding IL into it. It was found that the addition of IL, made the electrical response more suitable for low-power electronic devices, leading to a sharp reduction in the forming and set voltage range which is fundamental for a better energy management. **Figure 2.8** in chapter 2 explains the effect of IL when added to the polymer and Silver salt matrix. IL helps in the plasticizing effect of the polymer matrix, which helps in a better ionic mobility. **Figure 4.2** provides the electrical characteristics of the planar symmetrical device with PVDF-HFP_$AgNO_3$_IL as switching matrix. It is interesting to note that the initial switching took place at -2.2 V which corresponds to a forming field of 2.2 kV/cm. As explained in previous chapter, the

total concentration of $AgNO_3$ is 5wt. % of the total switching matrix. As this content is further increased we will have a further decrease in the initial set field to 1.25 kV/cm and 0.6 kV/cm (**Inset Figure 4.2 b**). But the increase in the concentration of $AgNO_3$ leads to a more conducting behavior of the device rather than a switching behavior. Thus the present concentration of 65/5/30 wt. % of Polymer/$AgNO_3$/IL is found to be the best measures of the constituents in the switching matrix. Thus the set field of 2.2 kV/cm can be considered as the general set field in our device. This value is 10 times lower than the switching field in the initial case without IL (**Figure 4.1a**). This 10 fold reduction can be explained solely by the presence of IL. IL reduced the crystallinity of the polymer NC switching matrix thus reducing dipole-dipole interactions, finally disrupting the transient cross-linkage bonds among the polymer matrix [**5**].

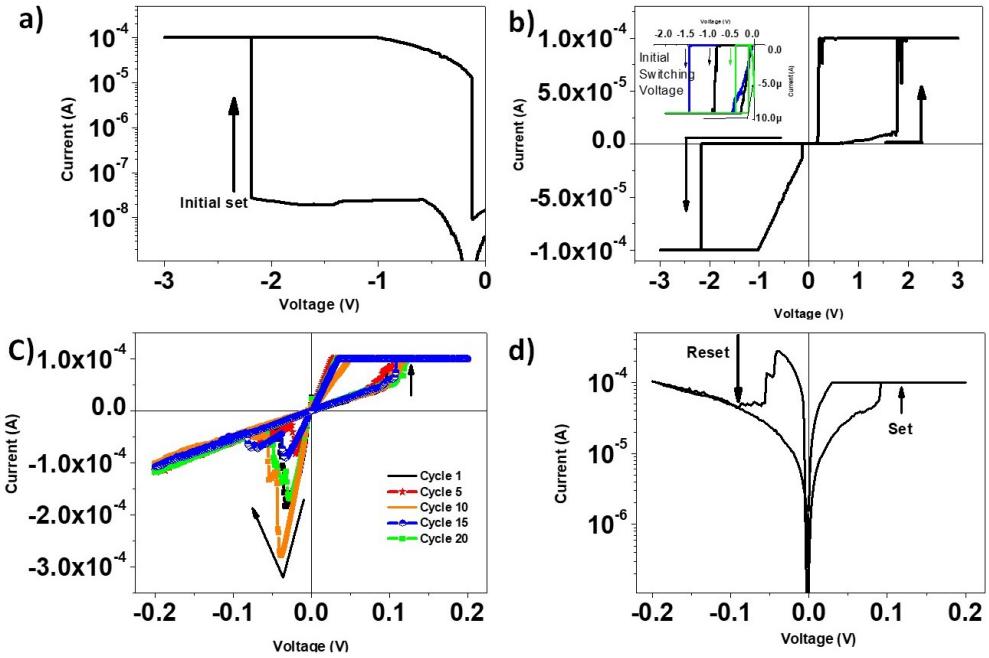

Figure 4.2: Electrical characterization performed on the planar symmetrical device with PVDF-HFP_$AgNO_3$_IL as switching matrix. a) Initial set taking place at -2.2V. b) Complete cyclic IV measure with 100µA compliance. Inset shows the further reduction of initial set with increase in $AgNO_3$ concentration c) Cyclic IV measure at higher reset compliance. d) Behavior of a single cycle at 1mA reset compliance

Once the initial forming was observed in the device, the optimal voltage range was examined, allowing to have a stable and repeatable switching. I-V characterization was performed between the voltage range of +0.2 V and -0.2 V. **Figure 4.2 c** displays the non-volatile switching behavior of the device. The set

states were always stable and the threshold voltage corresponding to set was near 0.1V; while the reset states had slight variations, the reset threshold was in the range of -0.05 V. The different reset compliance, coupled with the optimised voltage bias range and the pre-electrical treatment, changed the memory state of the RSD from volatile to non-volatile. The stability of the filament can be explained by the resistance level observed. The HRS which is ≈ 2KΩ (**Figure 4.2 d**), is lower than the LRS in **figure 4.2 a** (≥ 10 kΩ). The formation of a stable and continuous filament now enabled the device to set at a much smaller threshold voltage (0.1 V) as in **figure 4.2 d**. The increase of reset compliance along with the reduction in voltage range led to the destruction of the formed filament when it reached a negative threshold voltage of -0.05 V. Since the voltage was swept only till -0.2 V, there was no further filament formation, which made the device remain in its HRS until it reached its positive set threshold. Thus, maintaining its HRS until the device reached a positive set threshold. The higher ionic conduction provided by the IL based switching matrix when compared to the initial matrix can also be stated right by the impedance result obtained from the 2 matrices. **Figure 4.3** provides the Nyquist plot obtained from the impedance spectra analyzed in the frequency range [1 kHz, 10 MHz]. The figure provides a limited range of the impedance spectra in order to understand the difference in behavior of PVDF-HFP_$AgNO_3$ (Matrix1) and PVDF-HFP_$AgNO_3$_IL (Matrix2) based switching matrices. Data points corresponding to Matrix1 showed an impedance behavior that was dominated by simple diffusion processes. Matrix2 behavior, on the contrary, was more complex: in the low-frequency regime, a negative differential resistance was seen which took place from 10 down to 1 kHz, while in the high-frequency regime the behavior recovered the same features of the device with Matrix1. Thus, the data corresponding to Matrix2 was in support of a higher ionic conduction [**4**].

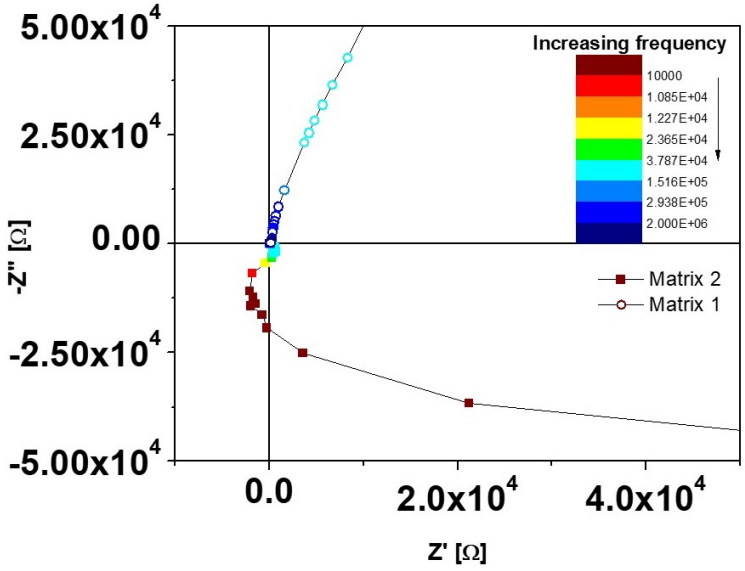

Figure 4.3: Nyquist response of the Matrix 1 and Matrix 2 analyzed from 1 kHz to 10 MHz **[4]**.

Figure 4.4 provides the SEM images where a clear evidence of the percolative conducting path made by the polymer NC (PVDF-HFP_$AgNO_3$_IL) between the electrodes is given.

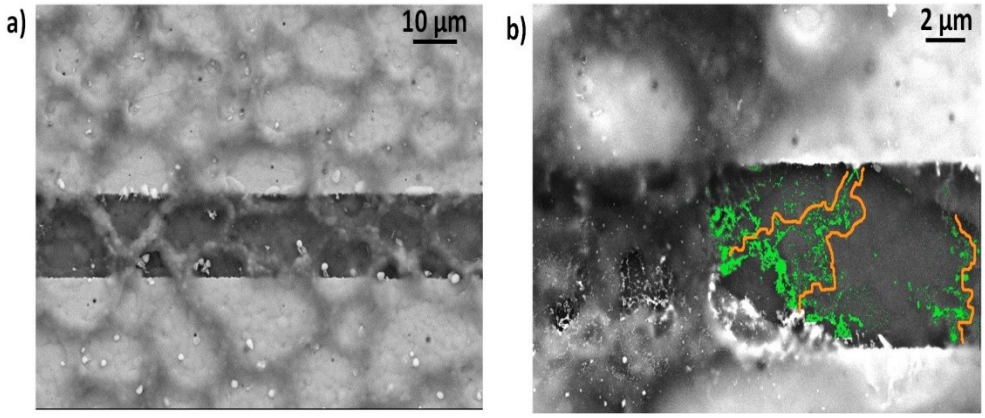

Figure 4.4: FESEM image of the characterized sample. a) Image of the switching gap with spin coated PVDF-HFP_$AgNO_3$and IL after electrical characterization. b) Magnified portion between the electrodes with percolation paths (evidenced by orange hand drawn lines) and Ag NPs (coloured in green) that bridge the two electrodes **[4].**

As it can be seen from **figure 4.4a** that a self-established network is found between the gold electrodes, suggesting the potentiality of our system to realize artificial neuron networks. This peculiar morphology is due to the shrinkage

during drying and the partial demixing of the polymer and silver salt. **Figure 4.4 b** provides a clear visualization of the dendritic growth of silver NP filaments (evidenced manually in green) between the gold electrodes, three of which are percolating and connecting opposite electrodes (orange lines manually drawn close to those NPs which were seen in contact from highly magnified FESEM images). The formation of dendritic filaments can be related to diffusion-limited aggregation of the Ag ions. A similar work has been carried out by Krishnan et al [**1, 6**], where a similar planar device was fabricated with symmetric Platinum electrodes and Ag-PEO was used as the polymer composite. To understand the retention of this device, a constant read voltage (0.05V) was probed at set and reset conditions. As observed from **figure 4.5**, the device maintained constant set resistance level for more than 6000 s. The set resistance was maintained at 500 Ω. The reset state was unstable till 1500 s. Later it turned stable and the device maintained this level till 6000s. The average reset resistance measured by the device during the retention test was about 7 kΩ. The test was interrupted and restarted in order to confirm non-volatility. It can be seen that the resistance values before and after the interruption (at 3.6 ks for the set state marked with red ellipse and 3.2 ks for the reset state which is marked with black ellipse in **figure 4.5**) recovered the previous resistance value. This confirmed the non-volatility of the device.

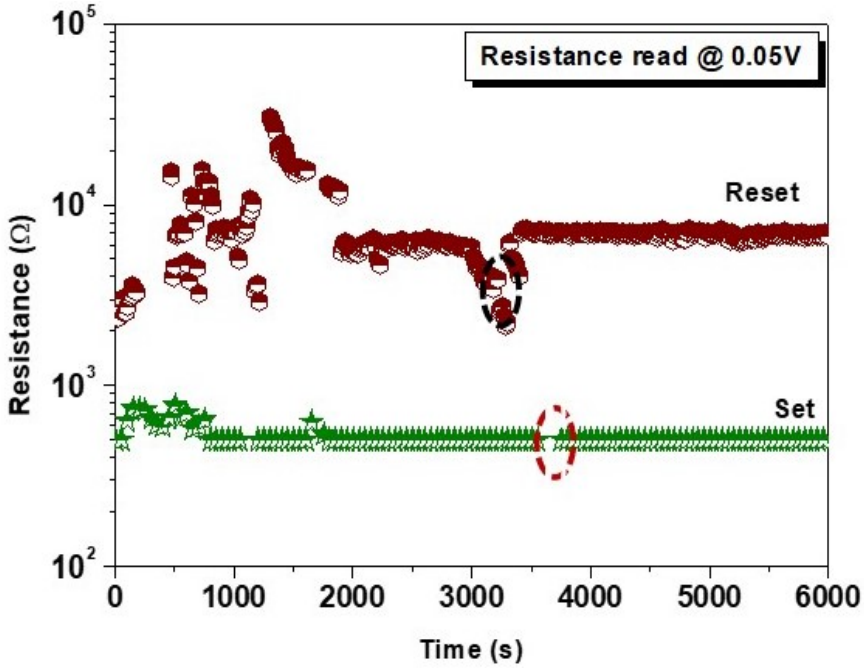

Figure 4.5: Retention characteristics of the device read at 0.05V.

As seen from the switching matrix based on EX-Situ Ag NPs, how it was affected by ageing due to the oxidation of Ag NPs, here an XPS was performed in order to understand the surface chemistry of the device. Since the switching matrix in planar device is more exposed to atmosphere we have a high chance of metallic oxidation. To clearly understand the effect of ageing , XPS was performed on 1) fresh planar device with PVDF-HFP_$AgNO_3$_IL deposited (but not tested)[Fresh: not tested], 2) electrically characterized planar device [Not Aged], 3) one month old characterized planar device [Aged] and 4) commercially available $AgNO_3$ powder for reference [Commercial $AgNO_3$]. **Figure 4.6** provides the XPS plot. The presence of C, O, N, Ag, F and some impurities due to precursor residues (Si and Cl) can be clearly understood from the survey spectra (**Figure 4.6 a**). To understand if Nitrogen was still bonded to Ag, N1 peaks were checked (**figure 4.6 b**). The three devices showed signals made up by two bands at ~399 and ~401 eV respectively due to C-NH_2 and C-NH_3, found in IL. No peaks were detected for typical nitrate chemical shift, which should be located at binding energy higher than 403 eV. While in the commercial AgNO3 powder, N1s signal features two separated peaks at 403 and 406.4 eV, which are due to nitrates **[7]**. **Figure 4.6 c** shows the Ag3d doublet core-level emission collected from the three devices. As it can be seen in the fresh sample, that has not been electrically characterized, the peak is made up of two bands: the first one at 367.8 eV (40.4%) and the second at 368.5 eV (59.6%).

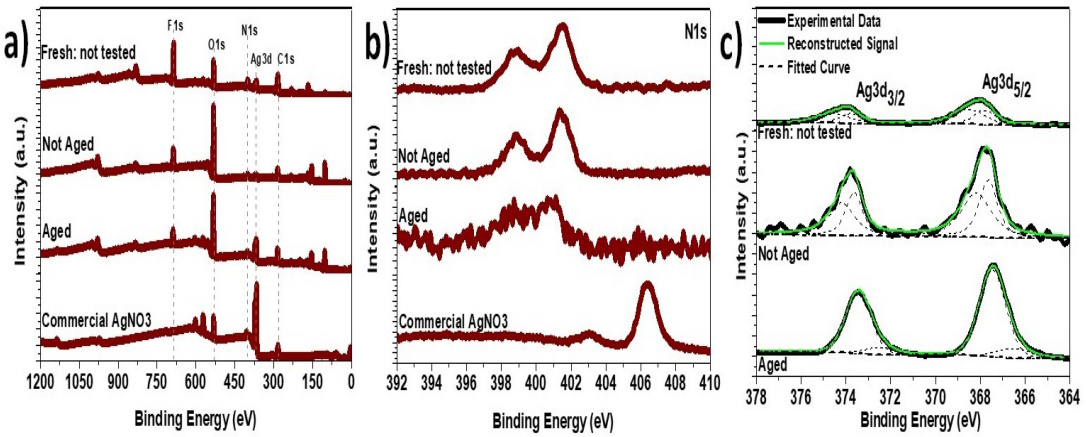

Figure 4.6: X-ray photoelectron spectra collected from NC based RSD prepared with PVDF-HFP_$AgNO_3$_IL on planar device. a) Survey Spectra. b) High Resolution (HR) spectra for N1s. c) HR spectra for Ag3d peaks (experimental data denoted by black lines, fitting curves denoted by dashed black line and reconstructed signal denoted by green line). The analyses are made on fresh untested sample (Fresh: not tested), sample after electrical characterization (Not Aged), on a one-month-aged sample submitted to

electrical characterization (Aged), which was kept at ambient conditions, and finally on commercial $AgNO_3$ powder (a and b graphs only).

The first value is typical of Ag_2O [**8**], while the second, which is shifted towards higher binding energies respect to reference value for metallic Ag (368.2 eV), has been assigned to Ag metal NPs [**9**]; which means that during the deposition the Ag was partially reduced, forming metal NPs with a thin layer of silver oxide on the surface. The sample after electrical characterization (not aged) presents the same peak for the Ag_2O (44.2%) chemical shift, while the peak at higher energy is located at 368.2 eV (55.8%), which is the Ag metal foil reference value. Thus it can be stated that electrical characterization changed the state of the Ag filler. The latter graph in **Figure 4.6 c** is related to the one-month-old tested sample (Aged). In this case, the $Ag3d_{5/2}$ peak is composed of two curves which are at 366.5 eV (8.3%) and 367.4 eV (91.7%). The first value is not common for Ag, since it is at very low binding energy. Thomas et al. [**10**] explained this chemical shift with the exposure of the composites to the ambient air, taking origin from Ag_2O. The peak at higher energy, in this case, is due to AgO [**10**]. So, we can state that the sample which was left for one month at ambient conditions (Aged) had gone through an ageing process which thickened the oxide layer, since no Ag metal component is present in the peak deconvolution.

4.3 Planar Asymmetrical device based on PVDF-HFP_$AgNO_3$_IL.

So far we have just been using planar symmetrical and stacked asymmetrical device. In the present section we will be using planar asymmetrical device (Section **2.2.2**). The electrode structure is same as that of the planar symmetrical case, just with the exception that instead of Au electrodes we use Ag and Pt electrodes. Ag being an active metal and Pt being a passive metal, the combination of these two metals in RSDs are well appreciated.

The switching matrix here which is PVDF-HFP_$AgNO_3$_IL is spincoated onto the device under ambient conditions. As seen from **figure 4.7** the device exhibits excellent switching behavior. The electroforming process, in which the device moves from its pristine HRS to LRS usually takes place at a higher voltage bias when compared to set voltage. In the present case, it was found to be around 2.29 V (**Figure 4.7 a**) which corresponds to an electric field of 2.29 kV/cm. **Figure 4.7 b** shows the consecutive switching cycles after the electroforming process. As it can be noted from the figure, there is a clear reduction in the applied field. The overall switching voltage range has now been optimised to ± 0.5V.

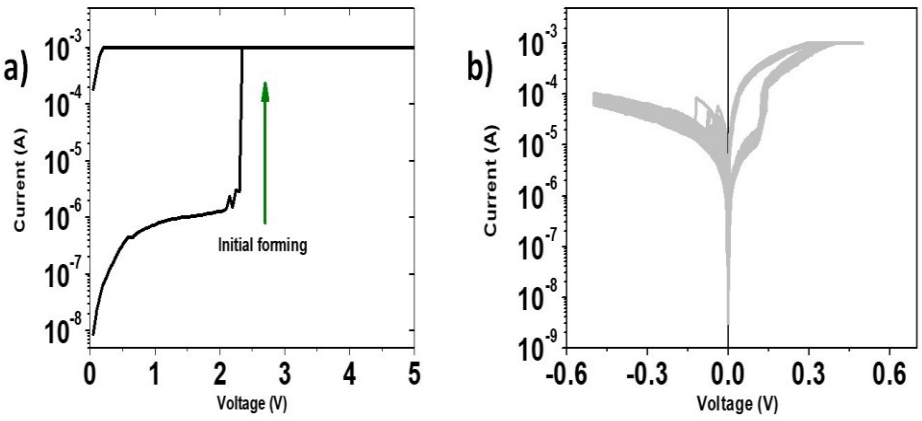

Figure 4.7: Electrical Characterization performed on planar asymmetrical device with PVDF-HFP_$AgNO_3$_IL as switching matrix. a) Initial electroforming taking place at 2.29 V. b) Cyclic IV behaviour after forming.

The device exhibits a continuous switching of 1100 cycles with a very small On/Off of 10. These many large number of cycles has been obtained mainly because of the use of asymmetric electrodes. Here along with the contribution from the Ag^+ ions and atoms in the switching matrix, the metal cations that are ejected from the anode also plays an important role in switching. With the application of active bias, metal cations (Ag^+ ions in this case) migrate to the counter electrode, where they are reduced by the electrons flowing from the cathode. The precipitation of the active metals at the cathode leads to the growth of metal protrusion which reaches the anode to form a highly conductive filament between the electrodes which leads to a bistable state. Thus here we have combined effect of both Ag from the electrode as well as from the switching matrix while switching. More study on this device will be conducted in chapter 5 and 6 where the endurance, mechanism, and other physical and chemical aspects of the device will be explained in detail.

4.4 Stacked Asymmetrical device based on PVDF-HFP_$AgNO_3$_IL.

To understand the dependence of device structure on the switching behavior, a stacked structure was realized with the above used switching matrix. As mentioned in chapter 2, section **2.2.3.1**, the BE was ITO-made and the TE was fabricated in gold (4 mm diameter). The matrix was spin coated onto the BE and then TE was deposited. The thickness of the spin coated matrix was in the range of few 100s of nm. Active bias was provided to ITO.

The electrical characterization carried out on the device exhibited a bipolar nonvolatile switching behavior (**Figure 4.8**). The On resistance and Off resistance at a read voltage of -1 V is 50 kΩ and 7 MΩ respectively, thus exhibiting an On/Off of 150. As in the previous case, in the initial testing conditions, a compliance current level of 1 mA and 100 μ A was set in the negative and positive polarities respectively. In the earlier case, where same matrix was coated onto the planar device with symmetrical gold electrodes, different switching mechanisms were observed according to the electrical parameters set, especially, the compliance current.

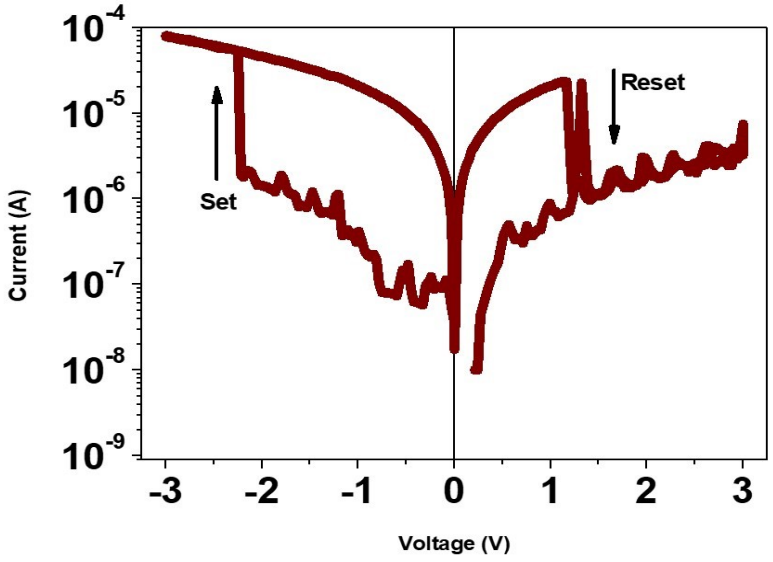

Figure 4.8: General IV behavior of the stacked device.

In the stacked device, the compliance levels dint effect the switching behavior. The device always exhibited nonvolatile switching behavior. Unlike other cases, where the set voltage reduced drastically after the forming, here we don't observe that phenomena. Thus the switching in this case can be explained by means other than filamentary conduction. Switching in this case can be explained by charge confinement within the NPs: initially, the charge gets trapped in the NPs and as the applied field is increased and reaches a certain set threshold (-1.7 kV/cm), the conductivity of the polymer NC is dramatically increased due to the easy movement of the charge through the polymer matrix which leads to the On state of the device. This state is maintained, until the applied field reaches a particular reset threshold (1.6 kV/cm), at which point the charges gets de-trapped thus making the device move back to its initial HRS [**4, 11**]. In order to understand the

switching stability of the stacked device, a pulse test was performed where the device was probed at 1V after setting and resetting the device -5V and 2V respectively. **Figure 4.9a** provides the input pulse and **figure 4.9 b** provides the output. As it can be seen, device read almost constant values for about 70 cycles. An average set current of about 250 µA and average reset current of about 2 µA was read at 1V, thus maintaining an On/Off of 100. The HRS showed a slight drift in the current with an increase in cycles: this is because the device had a tendency to move to a permanent On state as the cycles proceeded, and thus the current in HRS was slightly increasing. This case, where the stacked structure is considered, explains the fact that device engineering controls the device properties.

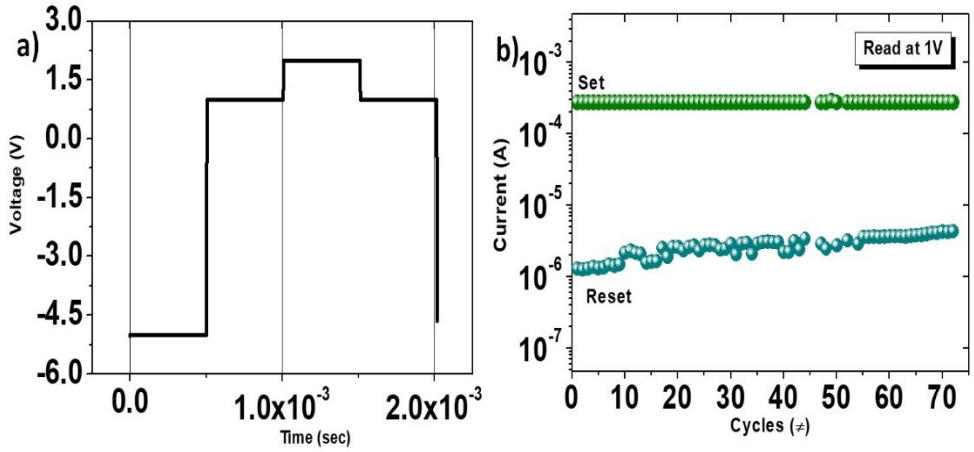

Figure 4.9: Pulse test carried on the stacked device. a) Input pulse signal applied. b) Output obtained

The present switching matrix based on PVDF-HFP, $AgNO_3$ and IL proves to be an excellent switching matrix. The presence of IL in the matrix makes this polymer NC a better switching candidate than the one explained in chapter 3. The device dependence is a major factor in this. As seen from the switching behaviors, the planar device with asymmetrical electrodes shows the highest number of switching cycles. The importance of IL now makes it an unavoidable ingredient in the coming switching devices **[4]**.

4.5 References

1. Krishnan K.; Tsuruoka, T.; Mannequin, C.; Aono, M. (2016). Mechanism for Conducting Filament Growth in Self Assembled Polymer Thin Films foe Redox-Based Atomic Switches. *Advanced Materials*, 28, pages 640-648.

2. Subburaj, T.; Jo, Y. N.; Lee, C. W. (2014). Effect of monocationic ionic liquids as electrolyte additives on the electrochemical and thermal properties of Li-ion batteries. *Current Applied Physics*, 14, pages 1022-1027.

3. Bandara, T.M.W.J.; Mellander, B. E. (2011). Evaluation of Mobility, Diffusion Coefficient and Density of Charge Carriers in Ionic Liquids and Novel Electrolytes Based on a New Model for Dielectric Response, Ionic Liquids: Theory, Properties, New Approaches (P. 384-406), InTech, DOI: 10.5772/15183.

4. Rajan, K.; Chiappone, A.; Perrone, D.; Bocchini, S.; Roppolo, I.; Bejtka, K.; CAstellino, M.; Pirri, C. F.; Ricciardi, C.; Chiolerio, A. (2016). Ionic liquid-enhanced soft resistive switching devices. *RSC Advances*, 6, pages 94128-94138.

5. Ramesh, S.; Liew, C. W.; Ramesh, K. (2011). Evaluation and investigation on the effect of ionic liquid onto PMMA-PVC gel polymer blend electrolytes. *Journal of Noncrystalline Solids*, 357, pages 2132-2138.

6. Krishnan, K.; Aono, M.; Tsuruoka, T. (2016). Kinetic factors determining conducting filament formation in solid polymer electrolyte based planar devices. *Nanoscale*, 8, pages 13976-13984.

7. Chiarotto, I.; Feroci, M.; Forte, G.; Inesi, A. (2015). Stability of electrogenerated 1-butyl-3-methylimidazol-2-ylidene in DMF. Part 2. Role of acid substrates. *Electrochimica Acta*, 176, pages 627-635.

8. Busby, Y.; PIreaux, J. J. (2014). Metal nanoparticle size distribution in hybrid organic/inorganic films determined by high resolution X-ray photoelectron spectroscopy. *Journal of Electron Spectroscopy and Related Phenomena*, 192, Pages 13-18.

9. Shin, H. S.; Choi, H. C.; Jung, Y.; Kim, S. B.; Song, H. J.; Shin, H. J. (2004). Chemical and size effects of nanocomposites of silver and polyvinylpyrolidone determined by X-ray photoemission spectroscopy. *Chemical Physics Letters*, 383, pages 418–422.

10. Thomas, S.; Nair, S. K.; Jamal, E. M.; Harthi, S. H.; Varma, M. R.; Anantharaman, M. R. (2008). Size dependent surface plasmon resonance in silver silica nanocomposites. *Nanotechnology*, 19, 075710.

11. Wang, Y.; Yan, X.; Dong, R. (2014). Organic memristive devices based on silver nanoparticles and DNA. *Organic Electronics*, 15, pages 3476-3481.

Chapter 5

PEO Based Smart Hybrid Devices

5.1 Introduction

The urge for developing an organo-metallic RSD is always at its peak due to the incredible features they exhibit like low cost, good retention time, processability, high endurance and mechanical flexibility, when coupled with polymeric or natural flexible substrates [**1**].

The polymer NC based switching devices that we have studied so far provide the perfect example for a cost effective and easily processable device fabrication technique. The performance of these devices may not be commendable in terms of its endurance or retention. PVDF-HFP which is a thermally stable polymer has been used in many applications including memory devices, Li batteries, fuel cells, solar cells etc [**2-6**]. PEO is another polymer matrix that is widely used as electrolyte in many applications like Li ion batteries, Dye sensitized solar cells etc like PVDF-HFP [**7-9**]. The characteristics of the polymer matrix play an important role in the transport of cations and anions in the switching matrix. PEO is well-known for its enhanced ionic conductivity. The self-assembled polymer structure in our RSD will have a great influence on the formation of conducting filaments as well as on the ion transport behavior [**7**]. In this chapter we will discuss the functionality and performance of PEO_$AgNO_3$_IL based planar RSD with electroanalytic methods and microscopy. Throughout the thesis, we have given importance for planar devices since the development of wearable, eventually printed, soft smart systems are more feasible with planar devices [**10-14**]. Part of

the work described in this chapter has been previously published in "*Journal Of Material Chemistry C, 5, 2017, (6144-6155).*"

5.2 PEO based planar symmetrical device

The PEO Polymer NC based switching matrix preparation has been discussed in chapter 2, section **2.3.4**. The PEO based matrix is spin coated onto the planar symmetrical device (Section **2.2.1**). Planar devices usually allows a straightforward implementation.

Figure 5.1 provides the results of the electrical characterization performed on the planar symmetrical device. The electroforming process took place at a voltage bias around -20 V (**Figure 5.1 a**) which corresponds to an electric field strength of 20 kV/cm. An electrically driven movement of Ag ions in the PEO matrix, forming a percolative path between the electrodes, finally leads to an increase in conduction of the device [**15**]. This is the reason behind forming process. A compliance was set to 1mA in both polarities after the electroforming process. **Figure 5.1 b** shows the subsequent set and reset after the forming. The overall working power has reduced as expected. Here we have a drastic reduction in the operating field. This can be attributed to the already created pre-channel for the formation of a metallic path between the electrodes [**16, 17**]. After the electroforming process, once the metallic filament penetrates into the switching matrix, a mechanical stress is created which in turn induces a preferable channel in the matrix which remains even after the rupturing of the filament. This channel then forms a physical template for the following switching events [**18**]. The switching from LRS to HRS is by the dissolution of the formed filament. As observed from **figure 5.1 c**, the set process took place at around 0.8 V and the reset at -0.6V. The On/Off of this system is quite low (2). As presented in **figure 5.1 d**, the On/Off throughout the 80 cycles is not quite stable. On current remains constant throughout the working cycles, while the Off current varies a lot throughout the working cycles.

To understand the difference in the switching gap before and after the switching process, FESEM imaging was performed on an untested sample and on an electrically characterized sample. **Figure 5.2** shows a clear difference between the tested and fresh devices. The active gap between the electrodes in the case of fresh device (**Figure 5.2 a**) shows no evident connections between the electrodes. After electrically characterizing the sample, there was a clear network-like connection between the electrodes (**Figure 5.2 b**). This connection network is evident in multiple points and can be ascribed to filament formed by the

movement of the silver ions. **Figure 5.2 b** has been subjected to a color enhancement to color the conducting network growing in the active gap between the electrodes.

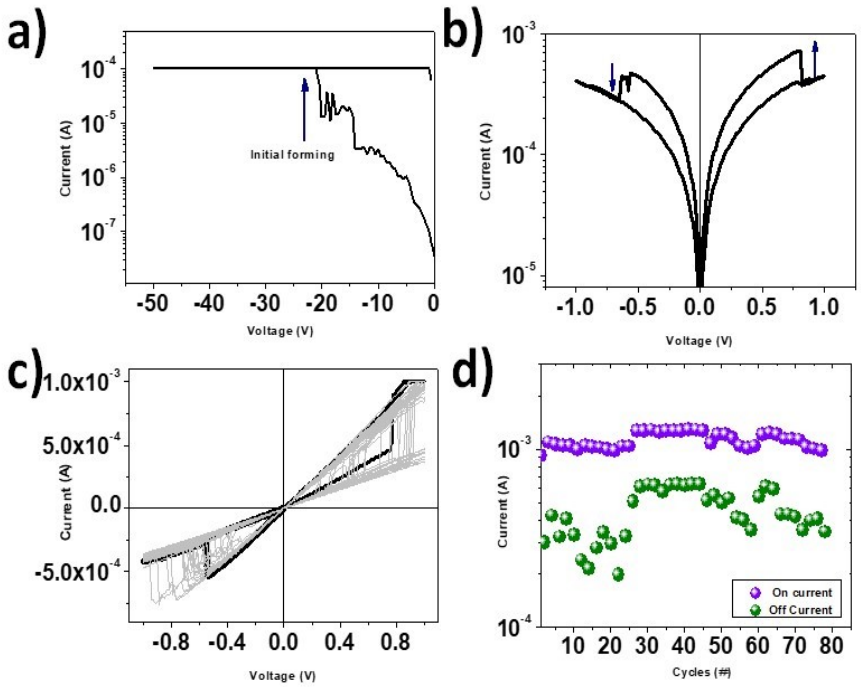

Figure 5.1: Electrical Characterization performed on PEO_AgNO3_IL based planar symmetrical device. a) Forming Process. b) Behaviour of individual cycle in logarithmic scale. c) Subsequent cycles after forming. d) On/Off current at a read voltage of 0.5V throughout continuous cyclic sweeps

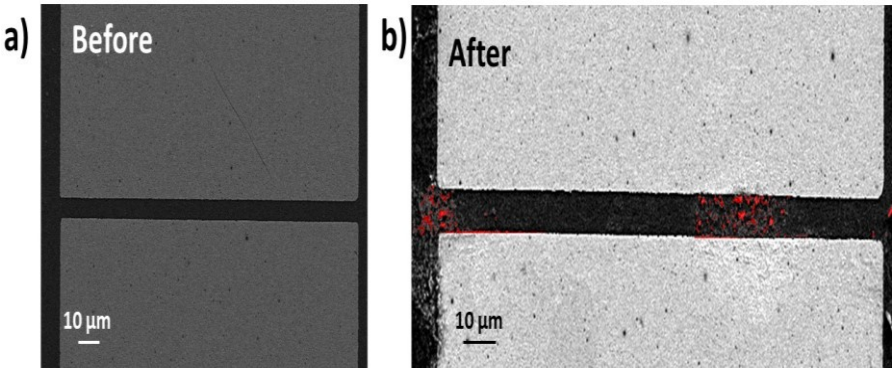

Figure 5.2: FESEM imaging on the RSD. a) Fresh device with switching matrix coated. b) Electrically characterized sample **[17].**

Generally, planar symmetric electrode structures compared to asymmetric ones are found to be less performing in terms of On/Off ratio and cyclability [7].

Thus we have used the same switching matrix on planar asymmetrical device with Ag and Pt electrodes.

5.3 PEO based planar Asymmetrical device

The performance of an RSD is highly associated to the electrode materials used [**19-21**]. In this regard, a planar asymmetric electrode structure was used to improve the properties especially in terms of its cyclability and On/Off ratio. An active and a passive material were used for the fabrication (Chapter 2 section **2.2.2**).

In the present case where planar asymmetrical electrode is used, 2 switching matrices with slight variation are made. The first one is the matrix which is discussed in section **5.2**, which involves PEO_$AgNO_3$_IL. The second one involves a matrix without $AgNO_3$. It has just PEO and IL. This PEO and IL matrix was tried in order to realize a complete ECM [**18, 22**] device in which the switching is caused by the movement of the injected metallic cations from the active towards the passive electrode where these cations get reduced thus forming a conducting filament.

5.3.1 Planar asymmetrical device based on PEO_$AgNO_3$_IL

The switching characteristics of the PEO_$AgNO_3$_IL on planar asymmetrical device is well studied in this section. **Figure 5.3** provides the electrical characterization results obtained from the device.

The device had its forming at 3.25 V (**Figure 5.3 a**) which corresponds to an electric field of 3.25 kV/cm. This forming field is four times lower than in the symmetrical case (**Figure 5.1 a**). The resistive switching in the symmetrical case was exclusively due to the action of the active switching matrix, while in the asymmetrical device, the silver electrode along with the Ag ions in the switching matrix have an active role in the switching of the resistance. The application of positive bias caused the electrically driven movement of the silver ions in the matrix and the oxidation of the edge of the silver electrode (active electrode) to Ag^+ [**18**]. After the initial cycling process, the device maintained a continuous resistive switching for the next 530 cycles (**Figure 5.3 b**). This so far is the highest number of reported cycles for a planar device with an active gap in the range of micrometers. Planar devices with micrometric gap tend to fail after 10's of cycles.

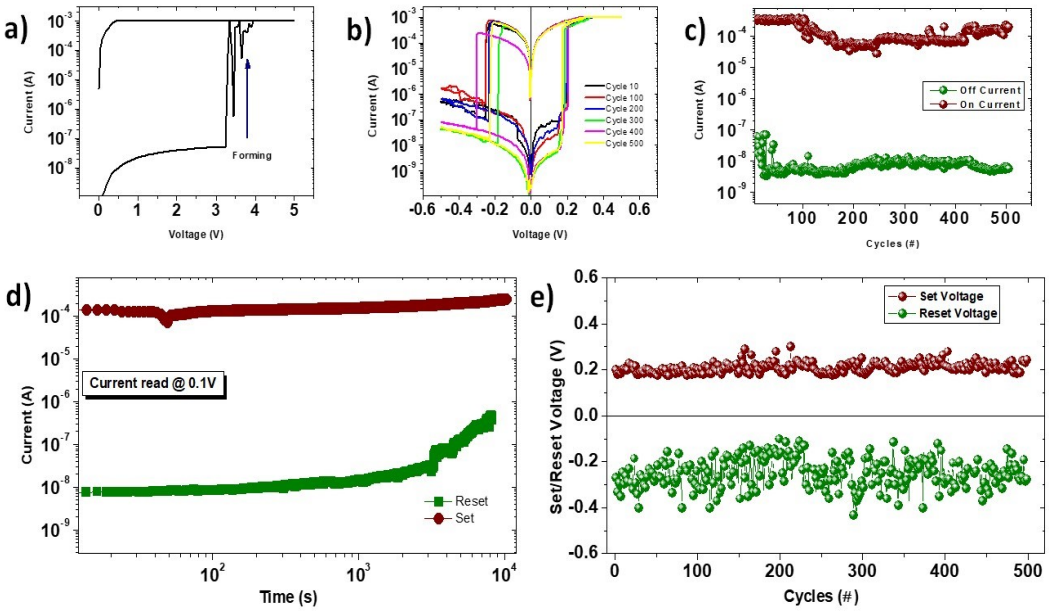

Figure 5.3: Electrical Characterization performed on PEO_$AgNO_3$_IL based planar asymmetrical device. a**)** Forming process. b**)** Continuous resistive switching taking place throughout the 500 working cycles. c**)** On and Off current read at 0.1V throughout continuous cyclic sweeps. d) Retention test carried out on the device. e) Set and reset voltage levels throughout the cyclic sweeps.

This is due to the degradation of the electrolyte matrix during switching, which often causes irreversible changes. With PEO based polymer switching matrix the long range Ag^+ transport can be hindered due to its limited amorphous phase. While in the present case, the device exhibits a good switching behaviour. The presence of IL can be the reason behind this upgraded performance. As mentioned in previous chapters, IL paves way for a facile path for the ionic movement and, moreover, it reduces the crystallinity of the polymer composite. This is the main reason for the large number of switching cycles in the present case. **Figure 5.3 c** illustrates the On and Off currents derived from the cyclic switching characteristics at a read voltage of 0.1 V. The ability of the device to maintain an On/Off of 10^4 throughout the working cycles makes this a promising hybrid device. Retention is an important factor to be considered while designing RSDs. The present device remained in its On state for almost 3 h, while the Off state was not as stable as the On state. After maintaining a certain reset current level for about 1 h, the reset current was slightly increasing (**Figure 5.3 d**). When considering a device for practical applications, other factors should also be considered such as variation in set and reset voltages during the cycling. As

observed from **Figure 5.3 e** the set voltage throughout the cycles remains the same, while a slight variation in the reset levels (voltage distributed between -0.1 and -0.4 V) can be seen, which could be mainly due to the structural instability of the formed filament in the switching matrix which is common in crystalline polymer matrices [**7,17,23**].

In order to confirm that the device switching is due to filamentary conduction and also to analyse if the formed filament is a metallic one, two different experiments were performed. Initially to confirm the filamentary conduction a compliance based test was performed. As it can be seen from **figure 5.4 a**, the On resistance of the device decreases with increasing compliance. This means that at higher compliance current, the filament that is formed is more thick and stable and thus a higher On current is produced and a higher off current is needed to break that filament. An electrical way of knowing the constituents of the formed filament is by conducting a temperature based electrical test, in which we can get an idea about the nature of the formed filament. As seen from **figure 5.4 b**, the increasing trend of the On resistance of the device with temperature explains that the device exhibits a metallic conduction till 300 K. An increasing weight of the ionic conduction channel [**24**] can be seen after 300 K which can be explained by the slight flattening of the curve.

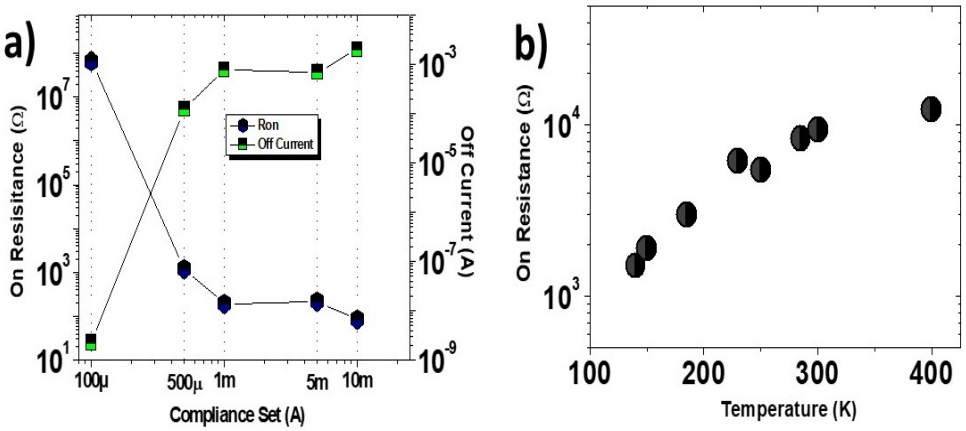

Figure 5.4: Electrical characterization carried out to study about the formed filament a) On Resistance and Off Current plotted as a function of Compliance current. b) On Resistance plotted as a function of Temperature.

FESEM and optical microscopy imaging were performed on the device before and after characterization to understand the difference in the active switching gap. The pristine device is always in its HRS and no evident conductive path between

the electrodes was present (**Figure 5.5 a**). After electrically characterizing the device and setting it, a clear filament-like pattern was present (**Figure 5.5 b**). **Figure 5.5 c** provides the corresponding FESEM image. A clear percolative path connecting the 2 electrodes can be present from the figure.

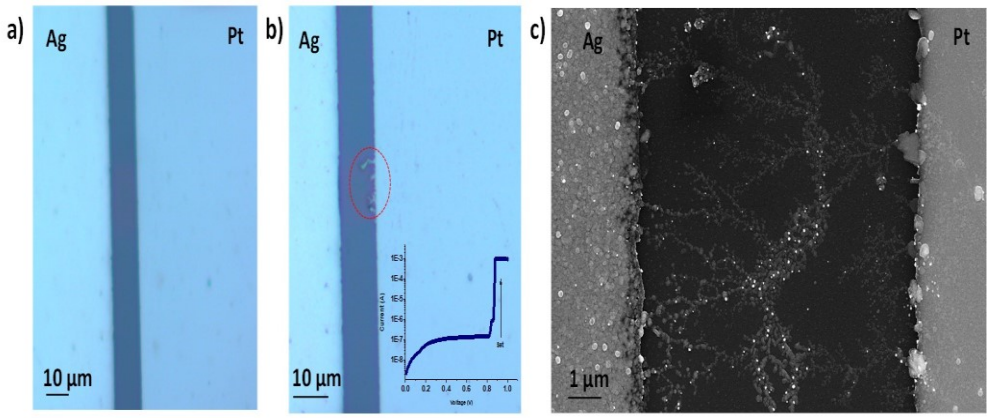

Figure 5.5: Optical microscopy and FESEM imaging performed on a single RSD. a) Optical micrograph of pristine device. b) Device imaged after switching on the device (inset shows the corresponding IV sweep). c) FESEM image corresponding to panel b **[17].**

FESEM imaging was performed on the samples which were electrically characterized for different number of switching cycle's in order to better understand about the filament formation. There was a significant difference in the active gap with an increasing number of characterization cycles. The pristine device shows a clear gap (**Figure 5.6 a**), while after 10 cycles the sample shows a gap with some connections between the electrodes (**Figure 5.6 b**). By increasing the number of cycles to 100, the active gap between the electrodes shows higher number of connections (**Figure 5.6 c**). Finally, the switching gap after 500 cycles of cyclic sweeping is also shown in **figure 5.6 d**. The conducting paths and the regions from where the silver ions were displaced are now obvious.

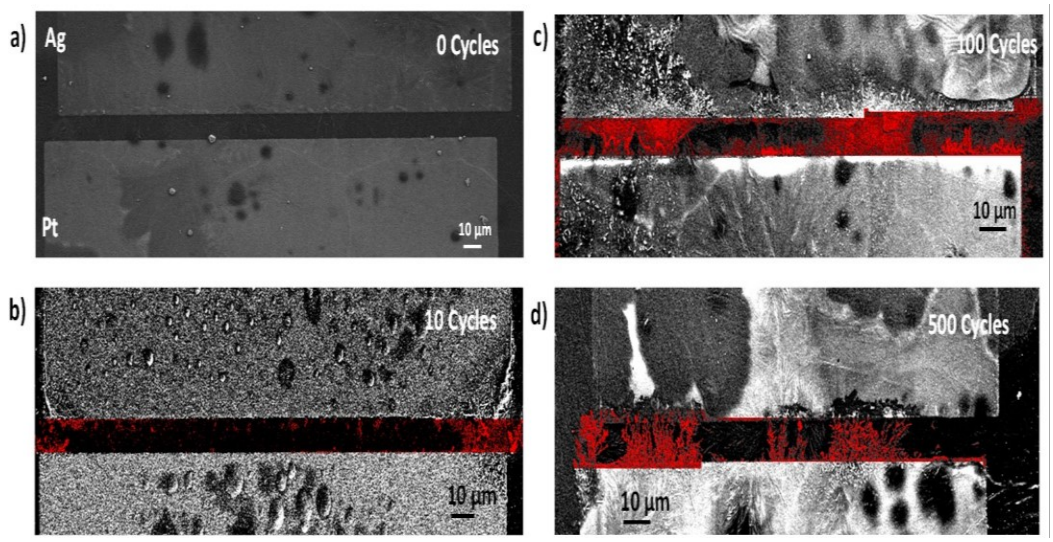

Figure 5.6: FESEM image of planar asymmetrical device showing the evolution of formed filament with an increase in number of cycles. a) RSD before electrical characterization. b) After 10 cycles of cyclic sweeps. c) 100 consecutive cyclic sweeps. d) 500 consecutive cyclic sweeps. (The red colored connections between the electrodes is by a mathematical algorithm performed to enhance the difference in the active gap after different number of cyclic sweeps) **[17].**

To understand the real time development of the filament due to silver ions diffusion, in situ electrical stress was made inside the PEO_$AgNO_3$_IL based switching matrix using Tungsten probes. A continuous cyclic sweep was applied from -10 V to 10 V. The formation and dissolution of a filamentary structure near the active probe which is marked in gray can be seen from **figure 5.7 (right panel)**. This image has been subjected to a mathematical algorithm to enhance the differences between the real FESEM images taken before and after stress (**Figure 5.7 left panel**). The eventual little misalignments of the two shots can be compensated by the geometrical registration process; a histogram correction and a conversion to double floating point numbers assigns numerical values to each pixel and allows to algebraically sum the frames. The false color scale reports stronger differences in yellow/orange evidencing the creation of the filament, and finally pink/magenta evidencing the annihilation of the filament [**17**]. Initially a cyclic bias was provided. As the voltage reached -10V, a clear filament was observed. This is due to the fact that at negative voltages, the Ag ions gets reduced forming silver atoms, thus forming a filament (**Figure 5.7 a**). As the voltage sweeps from -10V towards +2V, the filament dissolves (**Figure 5.7 b**). **Figure 5.7 c** corresponds to the further filament formation as the voltage sweeps

from the positive to negative voltage**.** The real switching mechanism from HRS to LRS and back to HRS will be explained in detail in section **5.4**.

As seen from **figure 5.3 b**, the device after setting, resets near -0.3V. And the process of switching On and Off is explained by the formation and dissolution of conducting filament. The reset process that happens in the negative polarity is actually not a straightforward process as it seems to be. This switching On and Off process that is happening in a particular memory window are the values that we have found after so many cycling's. Once the polarity of the active electrode (Ag), moves from positive to negative, there are three processes happening: 1) the oxidation reaction taking place on the formed filament, 2) joule heating effect which is one of the most important thermal effect leading to reset in most of RSDs, and 3) removal of the silver ions ($AgNO_3$) in the formed filament due to the effect of electric field.

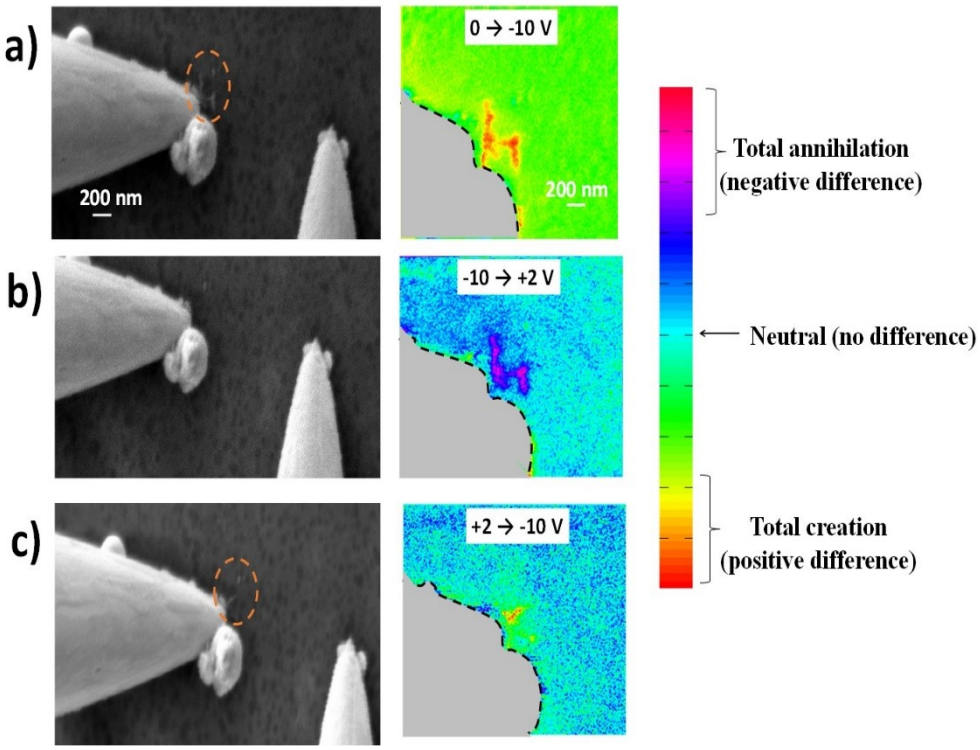

Figure 5.7: Real-time observation of the filament formation and annihilation. In the left we have the real FESEM images and the corresponding right side panels are the images that have been subjected to a mathematical algorithm to enhance the differences between the real FESEM images taken before and after stress (grey area corresponds to tungsten nano probe). a) Filament formation at set threshold. b) Filament dissolution at reset threshold c) Further filament formation.

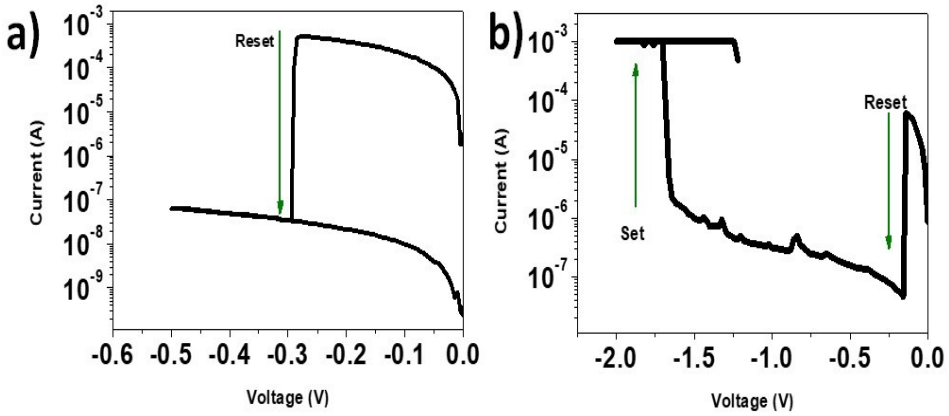

Figure 5.8: Cyclic curve showing reset process a) negative polarity cycled till -0.6V b) after further increasing the negative sweep voltage to -2V.

These combined effects cause a destruction in the earlier formed filament. This is the general case. Usually the cyclic voltage range of an electroformed device is optimised in order to maintain continuous switching cycles. This optimisation is very important especially in such cases where organic switching matrices are used. As seen from **figure 5.3 b**, the working voltage range of the device has been optimised in the range of +0.6 to -0.6V, in which case we have the set of the device in positive and reset in negative. As seen from **figure 5.8 a**, the device was at its LRS while passing from 0 to negative values. Ones the voltage reach -0.3 V, the device moves to HRS. As it can be observed from **figure 5.8 b**, when the negative voltage was increased from -0.6 V to -2 V the device again moves to LRS at around -1.6 V. This set process taking place at – 1.6 V can in no way be attributed to silver based filament conduction. Thus in this case where we see a set process taking place at higher negative voltage can be attributed to O_2 vacancies. We have a filament like connection formed by the oxygen vacancies which helps in the conduction. A similar observation has been made by Liu et al. [**25**], where both Copper nanobridge and oxygen vacancy filament were present when positive and negative forming voltages were applied to the Pt electrode respectively. Thus optimising the working voltage range is very important in RSDs.

5.3.2 Planar asymmetrical device based on PEO_IL

To further understand the ability of the PEO and IL matrix to enable the formation of a conductive filament without the contribution of Ag ions from the switching

matrix, another test was performed by spin coating just PEO and IL (50% each) on the planar asymmetric device.

This case where the switching matrix is just composed of PEO and IL, falls under the category of ECM. **Figure 5.9** provides the electrical characterization result performed on this device.

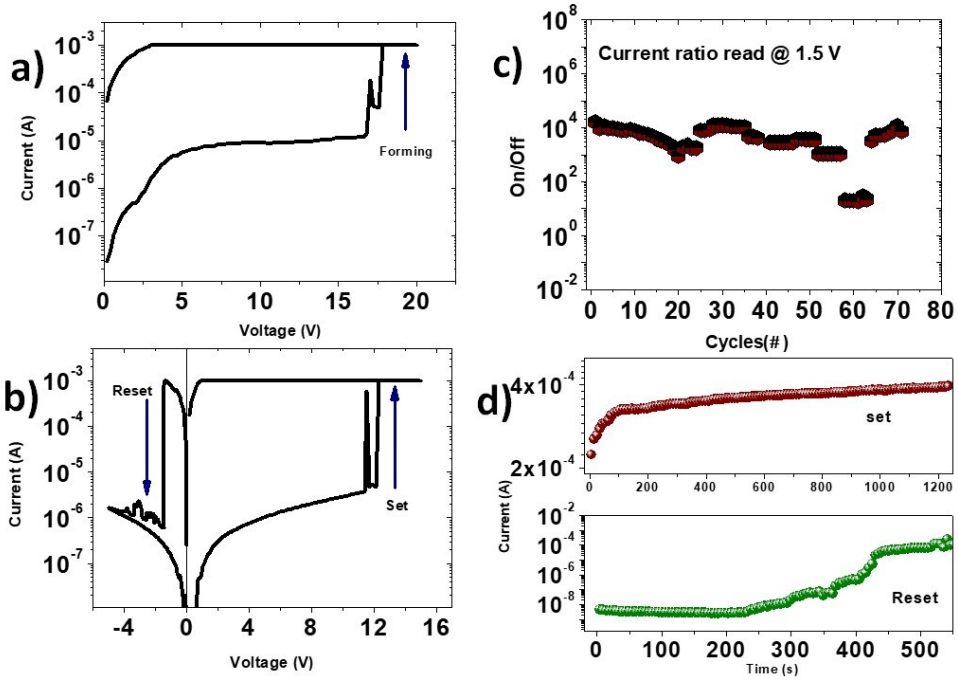

Figure 5.9: Electrical characterization performed on the planar asymmetric RSD with PEO_IL as switching matrix. a) Forming process b) IV behavior of a single cycle shown in logarithmic scale. c) On/Off current ratio read at 1.5 V throughout continuous cyclic sweeps. d) Retention test performed on the device.

The present device discussed had a forming at 16.7V which corresponds to a field of 16.7 kV/cm (**Figure 5.9 a**). This increase in the forming voltage compared to the case with PEO_$AgNO_3$_IL as switching matrix can be attributed to the fact that, here the switching is solely due to the movement of the oxidized Ag ions from the active Ag electrode. A comparatively higher field is needed to move the device from the Off to On state. The following switching after forming took place at a lower voltage around 12 V (**Figure 5.9 b**) and the reset took place around -1.5 V. **Figure 5.9 c** shows the On/Off current ratio read at 1.5 V throughout the 75 cycles. As it can be seen, the device does not maintain a constant ratio throughout. The ratio varies from 10^4 to 20. The lack of stability in this particular case cannot be explained in a systematic way, although the micrometric switching gap and the

absence of Ag salt can be a main reason. A retention test performed on the device showed that a constant set state was maintained for about 1000 s, while the reset state was quite unstable and the device maintained it's off state only for about 250 s, after which it moved to a high conducting state (**Figure 5.9 d**).

Figure 5.10a provides the FESEM image of the electrically characterized RSD with PEO and IL switching matrix. As seen, evident filaments are present between the electrodes. These filaments begin from the Pt electrode and move towards the counter Ag electrode. When the reset happens, they rupture or get disconnected from the upper side (from the Ag electrode).

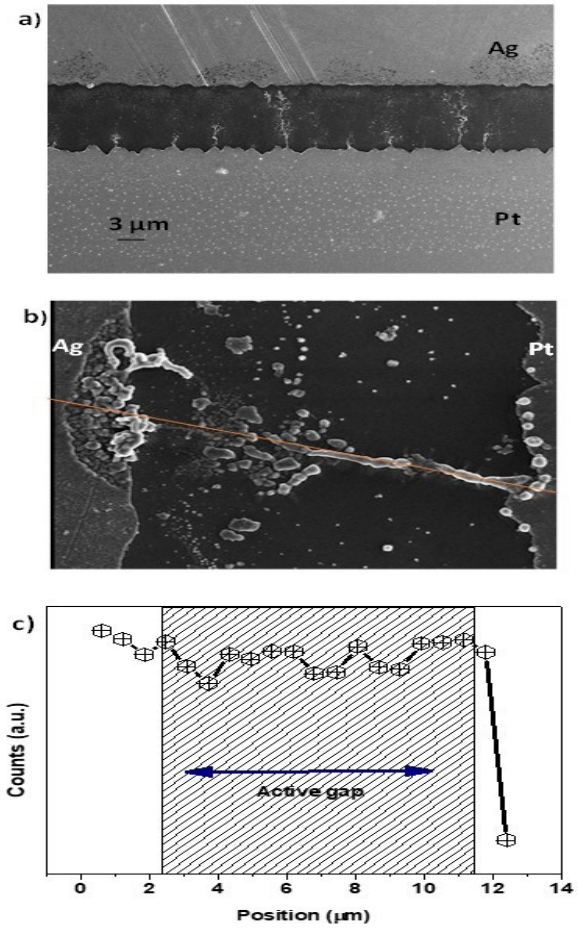

Figure 5.10: FESEM imaging and EDX carried on RSD with PEO and IL as switching matrix a) FESEM image of the asymmetrical RSD with the entire switching gap. b) Individual Silver filament between the electrodes. c) EDX line profile concerning the silver intensity in the active gap.

The observed filaments are thinner close to the inert electrode (Pt) and are broadening towards the active electrode (Ag). This is due to the fact that the optical lithography process induces the formation of random waviness along the electrodes. Locally, the geometrical inhomogeneities look like triangles that enhance the electric field and act to initiate the filament growth. This is an important intimation for future engineering of the electrodes, where we can completely control and initiate the filament growth. The small hole-like regions on the silver electrode confirm the movement of oxidized Ag ions from the Ag electrode [**17**]. EDX line measurement was performed to confirm the composition of the filament formed in the RSD with PEO and IL switching matrix. The filament formed in between the electrodes (**Figure 5.10 b**) can be confirmed to be silver conductive filament. The filament considered in **figure 5.10 b** is one among the filaments in **figure 5.10 a**. The line profile (**Figure 5.10 c**) confirms the presence of silver both in the gap and penetrated into the edge of the platinum electrode.

Thus considering the PEO based switching matrices in section **5.3.1** and **5.3.2**, we can state that in order to observe a continuous resistive switching in planar device architecture with an active gap distance of around tens of micrometers, it is always better to incorporate ionic liquid in the polymer matrix along with active metal ions or metal NPs. The effective cross section area of the Ag filament formed in the PEO and IL based matrix can be obtained using a simple model developed by Guo et al. [**26**]. F**igure 5.11 a** gives a schematic representation of the Ag filament growth. The Ag seed refers to the Ag ion which has migrated from the Ag electrode towards the Pt electrode and has got reduced. As seen from **figure 5.11 b**, the device is in its HRS till 250 seconds, and as time increases the current builds up indicating the growth of Ag filament induced by a constant voltage (3V in this case).

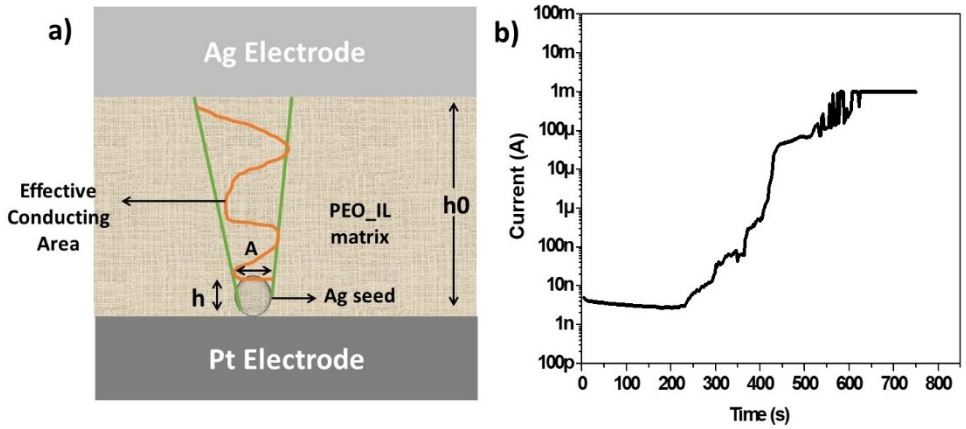

Figure 5.11: Represents the metallic Ag filament growth in PEO_IL matrix based RSD. a) Schematic representation of the Ag filament growth. b) Current-time plot of the RSD

Based on this, we can say that the volume of the Ag filament can be calculated from the charge that is under reduction

$$\int_0^h Adh = V0 \int_0^t I_{ion} dt \qquad (5.1)$$

Where t is the time until which the voltage is applied on the device, h is the effective length of the Ag seed, I_{ion} is the ionic current that passes through the PEO_IL matrix between the Ag seed and the Ag electrode with effective cross-section area A and effective length h0-h, V0 is the volume of the Ag metal reduced from Ag cations by 1 C charges. V0 can be written as

$$V0 = M/\rho e N_A \qquad (5.2)$$

Where M is the mole mass of Ag, ρ is the density of Ag, e is the electron charge and N_A is the Avogadro number.

Based on Ohms law, the ionic current I_{ion} can be written as

$$I_{ion} = U\sigma_{ion} \frac{A}{h0-h} \qquad (5.3)$$

Here U is the applied voltage on the device, σ_{ion} is the ionic conductance of the PEO_IL matrix.

The normalized growth rate of Ag filament can be written from Equations 5.1 and 5.3 as

$$\frac{h}{h0} = 1 - \sqrt{1 - 2\frac{U\sigma_{ion}V0}{h0^2}t} \qquad (5.4)$$

As mentioned earlier, once the applied bias exceeds a certain time, the current in the device increases enormously. This means that the filament now connects the bottom and the top electrode. Which means h/h0 = 1.

According to Ohms law, the effective cross section area of the formed filament from a current-time plot can be written as,

$$A = \frac{h0I}{U\sigma}\sqrt{1 - 2\frac{U\sigma_{ion}V0}{h0^2}t} \qquad (5.5)$$

Where σ is the overall conductance of the PEO_IL matrix (Which includes ionic as well as electronic conductance). *I* can be obtained from the current-time plot (**Figure 5.11 b**). The area that we are obtaining in this equation is an effective cross section area of the Ag dendrites with time. Thus by Substituting the values at time t= 450sec (device moves to LRS at this point) in (5.5), we obtain the effective area as 3 a.u.

5.4 Switching Mechanism of PEO based smart hybrid RSDs

So far we have seen a detailed electrical characterization and a basic idea on how the device works. In this section we see in detail the working mechanism of these devices.

We will see the working mechanism of the planar symmetrical device with PEO_$AgNO_3$_il as switching matrix. It should be noted that the same mechanism can also be explained for the working of PVDF-HFP_$AgNO_3$_IL based planar symmetrical device which has been explained in chapter 4, section **4.2**.

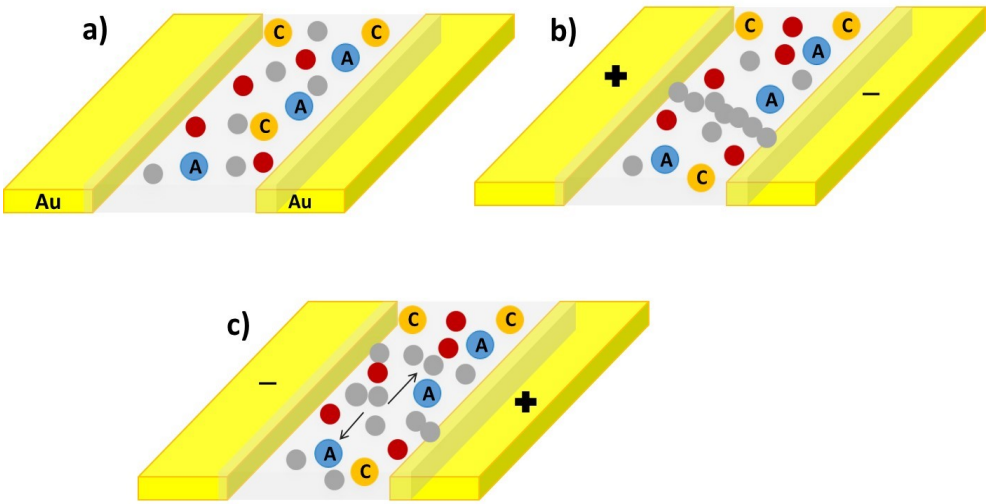

Figure 5.12: Schematic representation of the switching mechanism in planar symmetric device. a) Pristine device. b) Device in On state. c) Device in Off state. [Gray circles corresponds to Ag ions from the $AgNO_3$, Red circles corresponds to Nitrate ions, Circles with A and C corresponds to the anion and cation part of the IL. All these are dispersed in the polymer matrix]

Figure 5.12 provides the schematic representation of the working mechanism of the planar symmetrical devices with PEO_$AgNO_3$_IL as switching matrix. **Figure 5.12 a** represents the fresh untested device with the matrix spin coated on it. With the application of a positive bias (**Figure 5.12 b**), the silver ions move in the switching matrix leading to the growth of a silver filament, which causes the switching On of the device. The reversal of the bias leads to the dissolution of the formed filament, which brings to the Off state (**Figure 5.12 c**).

As mentioned earlier, in the case of asymmetrical device, the conduction mechanism is not exactly similar to the above case. Here along with the contribution of the metal ions from the matrix, the electrodes also play a major role in the switching of the device. **Figure 5.13** represents the schematic representation of the switching mechanism happening in PEO_$AgNO_3$_IL based planar asymmetrical device.

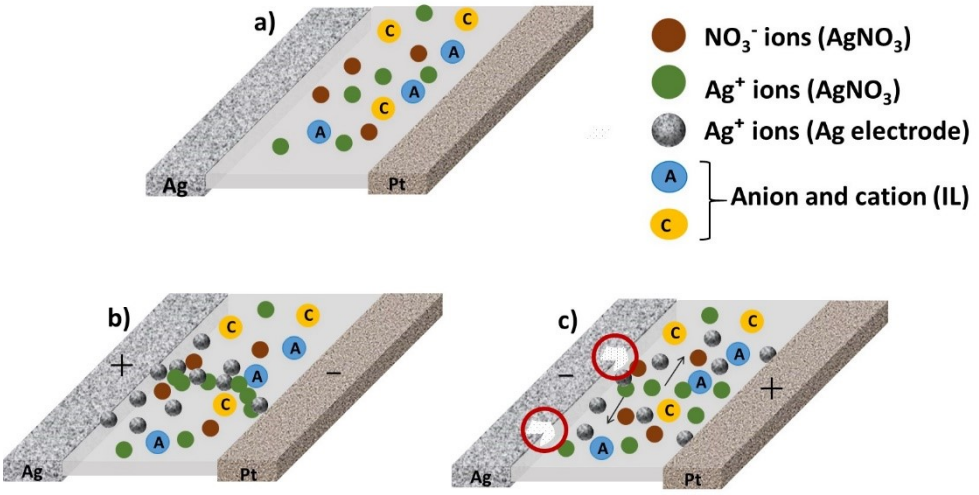

Figure 5.13: Schematic representation of the switching mechanism in planar asymmetric device. a) Pristine device. b) Device in On state. c) Device in Off state. [The red circle corresponds to the region on the Ag electrode from where the Ag ions have been oxidized and diffused into the switching matrix]

As it can be seen from **Figure 5.13 a,** in the pristine device the switching matrix (PEO_$AgNO_3$_IL) is spin coated on the planar gap. With the application of a positive bias (**Figure 5.13 b**), along with the Ag ions from $AgNO_3$, we can also see the silver ions from the silver anode oxidizing and moving into the matrix towards the platinum electrode. Thus, the combined effect of movement of silver ions in the matrix along with the oxidation reaction of the silver electrode causes the switch On of the device. With the reversal of bias (**Figure 5.13 c**), the opposite reaction takes place, which is the dissolution of the formed continuous path along with the formation of voids in the silver electrode (circle shown in red). This leads to the off state of the device. Once the active electrode polarity changes from positive to negative, there are 3 processes happening: 1) the oxidation, reaction taking place on the formed filament; 2) the joule heating effect, leading to reset in most of the RSDs [**24**]; and 3) the removal of the silver ions in the formed filament due to the effect of electric field. These combined effects cause a destruction in the earlier formed filament [**17**]. These explanations have also been validated by the FESEM images that we have obtained.

Finally the switching mechanism in the case of planar asymmetrical device with PEO_IL as matrix. In this case the switching is mediated only by the oxidized metal ions from the anode. **Figure 5.14** shows the schematic representation of the switching mechanism in this case. **Figure 5.14 a** represents the untested device.

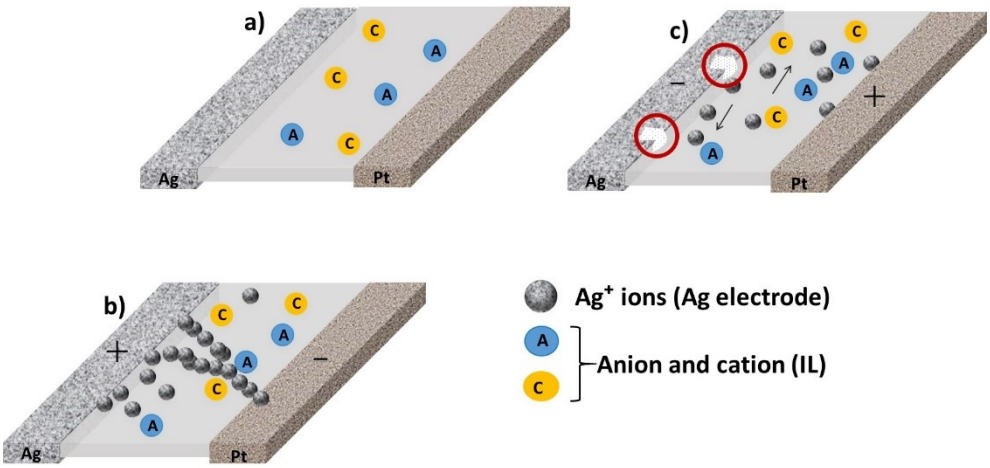

Figure 5.14: Schematic representation of the switching mechanism in planar asymmetric device with PEO_IL as switching matrix. a) Pristine device. b) Device in On state. c) Device in Off state. [The red circle corresponds to the region on the Ag electrode from where the Ag ions have been oxidised and diffused into the switching matrix]

As explained in previous cases, the application of a particular positive voltage should trigger the oxidation of the silver electrode and lead to the movement of silver ions towards the counter electrode. Once they reach the counter electrode, they reduce at the cathode (platinum electrode) and lead to the switching of the device (**Figure 5.14 b**). The reversal of the applied bias leads to the breakage of the formed filament. Note that this rupturing occurs at the top of the filament (near the silver electrode) (**Figure 5.14 c**).

5.5 References

1. Scott, J. C.; Bozano, L. D. (2007). Nonvolatile memory elements based on organic materials. *Advanced Materials*, 19, pages 1452–1463.

2. Rajan, K.; Bocchini, S.; Chiappone, A.; Roppolo, I.; Perrone, D.; Bejtka, K.; Ricciardi, C.; Pirri, C. F.; Chiolerio, A. (2017). Spin-coated silver nanocomposite resistive switching devices. *Microelectronic Engineering*, 168, pages 27-31.

3. Rajan, K.; Bocchini, S.; Chiappone, A.; Roppolo, I.; Perrone, D.; Castellino, M.; Bejtka, K.; Lorusso, M.; Ricciardi, C.; Pirri, C. F.; Chiolerio, A. (2017). WORM and bipolar inkjet printed resistive switching devices based on silver nanocomposites. *Flexible and Printed Electronics*, 2, 024002.

4. Miao, R.; Liu, B.; Zhu, Z.; Liu, Y.; Li, J.; Wang, X.; Li, Q. (2008). PVDF-HFP based porus polymer electrolyte membranes for lithium-ion batteries. *Journal of Power sources*, 184, pages 420-426.

5. Inan, T. Y.; Dogan, H.; Gungor, A. (2013). PVDF-HFP membranes for fuel cell applications: effects of doping agents and coating on the membranes properties. *Ionics*, 19, pages 629-641.

6. Wang, P.; Zakeeruddin, S. M.; Exnar, I.; Gratzel, M. (2002). High efficiency dye-sensitized nanocrystalline solar cells based on ionic liquid polymer gel electrolyte. *Chemical Communications*, 0, pages 2972-2973.

7. Krishnan K.; Tsuruoka, T.; Mannequin, C.; Aono, M. (2016). Mechanism for Conducting Filament Growth in Self Assembled Polymer Thin Films for Redox-Based Atomic Switches. *Advanced Materials*, 28, pages 640-648.

8. Alarcon, C. H.; Pennadam, S.; Alexander, C. (2005). Stimuli responsive polymers for biomedical applications. *Chemical Society Reviews*, 34, pages 276-285.

9. Michael, M. S.; Jacob, M. M. E.; Prabhakaran, S. R. S.; Radhakrishna, S. (1997). Enhanced lithium ion transport in PEO-based solid polymer

electrolytes employing a novel class of plasticizers. *Solid State Ionics*, 98, pages 167-174.

10. Cai, X.; Peng, M.; Yu, X.; Fu, Y.; Zou, D. (2014). Flexible planar/fiber-architectured supercapacitors for wearable energy storage. *Journal of Material Chemistry C*, 2, pages 1184-1200.

11. Liu, B.; Tan, D.; Wang, X.; Chen, D.; Shen, G. (2013). Flexible, planar integrated, all solid state fiber supercapacitors with an enhanced distributed capacitance effect. *Small*, 9, pages 1998-2004.

12. Peng, L.; Peng, X.; Liu, B.; Wu, C.; Xie, Y.; Yu, G. (2013). Ultrathin two-dimensional MnO2/graphene nanostructures for high-performance, flexible planar supercapacitors. *Nano Letters*, 13, pages 2151-2157.

13. Wan, C. J.; Liu, Y. H.; Feng, P.; Wang, W.; Zhu, L. Q.; Liu, Z. P.; Shi, Y.; Wan, Q. (2016). Flexible metal oxide/graphene oxide neuromorphic transistors on flexible conducting graphene substrates. *Advanced Materials,* 28, pages 5878-5885.

14. Semple, J.; Moon, G. W.; Georgiadou, D. G.; McLachlan, M. A.; Anthopoulos, T. D. (2017). Semiconductor free non-volatile resistive switching memory devices based on metal nanogaps fabricated on flexible substrate via adhesion lithography. *IEEE Transactions on Electron Devices*, DOI: 10.1109/TED.2016.2638499.

15. Krishnan, K.; Aono, M.; Tsuruoka, T. (2016). Kinetic factors determining conducting filament formation in solid polymer electrolyte based planar devices. *Nanoscale*, 8, pages 13976-13984.

16. Liu, D.; Wang, N.; Wang, G.; Shao, Z.; Zhu, X.; Zhang, C.; Cheng, H. (2013). Nonvolatile bipolar resistive switching in amorphous Sr-doped LaMnO3 thin film deposited by radio frequency magnetron sputtering. *Applied Physics Letter,* 102, 134105.

17. Rajan, K.; Bejtka, K.; Bocchini, S.; Perrone, D.; Chiappone, A.; Roppolo, I.; Pirri, C. F.; Ricciardi, C.; Chiolerio, A. (2017). Highly performing Ionic Liquid enriched hybrid RSDs. *Journal of Material Chemistry C*, 5, pages 6144-6155.

18. Valov, I.; Waser, R.; Jameson, J. R.; Kozicki, M. N. (2011). Electrochemical metalization memories- Fundamentals, application prospects. *Nanotechology*, 22, 289502.

19. Valov, I.; Linn, E.; Tappertzhofen, S.; Schmelzer, S.; Hurk, J.; Lentz, F.; Waser, R. (2013). Nanobatteries in redox-based resistive switches require extension of memristor theory. *Nature Communications.* 4, 1771.

20. Lin, C. C.; Chang, Y. P.; Ho, C. C.; Shen, Y. S.; Chiou, B. S. (2011). Effect of top electrode materials on the nonvolatile resistive switching characterestics of CCTO films. *IEEE Transaction on Magnetics,* 50, pages 633-636.

21. Chen, C.; Gao, S.; Tang, G.; Fu, H.; Wang, G.; Song, C.; Zeng, F.; Pan, F. (2013). Effect of electrode materials on AIN-based bipolar and complementary resistive switching. *ACS Applied Materials and Interfaces,* 5, pages 1793-1799.

22. Yang, Y.; Gao, P.; Gaba, S.; Chang, T.; Pan, X.; Lu, W. (2012). Observation of conducting filament growth in nanoscale resistive memories. *Nature Communications.* 3, 732.

23. Guo, X.; Schindler, C.; Menzel, S.; Waser, R. (2007). Understanding the switching-Off mechanism in Ag+ migration based resistively switching model systems. *Applied Physics Letters,* 91, 133513.

24. Pan, F.; Chen, C.; Wang, Z. S.; Zeng, F. (2010). Nonvolatile resistive switching memories-characterestics, mechanisms and challenges. *Progress in natural Science: Materials International,* 20, pages 1-15.

25. Liu, T.; Verma, M.; Kang, Y.; Orlowski, M. K. (2012). Coexistence of bipolar and unipolar switching in Cu/TaOx/Pt resistive devices for Cu and oxygen vacancy nanofilaments. *ECS Transactions*, 45, pages 279-285.

26. Guo, H. X.; Gao, L. G.; Xia, Y. D.; Jiang, K.; Xu, B.; Liu, Z. G.; Yin, J. (2009). The growth of metallic nanofilamnets in resistive switching memory devices based on solid electrolytes. *Applied Physics Letters*, 94, 153504.

Chapter 6

Performance comparison of hybrid RSDs

6.1 Introduction

Organic NC based RSDs exploit the intrinsic properties of organic materials, including processability, good retention time, high endurance and mechanical flexibility as mentioned previously. In the present case three different polymer NC based switching devices are studied and compared.

6.2 Electrical Characteristics of individual RSDs

The present work compares the influence of different polymer matrices on the performance of planar asymmetric Resistive Switching Devices (RSDs) based on silver nitrate and Ionic Liquid (IL). PVDF-HFP, PEO and PMMA were used as matrices and compared.

The switching mechanism in all the three sample families is explained by means of a filamentary conduction. A huge difference in the cyclability and the On/Off ratio is experienced when changing the active polymers and explained based on the polymer crystallinity and general morphology of the prepared Nanocomposite. The device used in all the 3 cases is the planar asymmetrical device which is explained in chapter 2 section **2.2.2**. The switching matrix preparation using PVDF-HFP, PEO and PMMA are mentioned in section: **2.3.3**, **2.3.4** and **2.3.5** respectively. All the three matrices has $AgNO_3$ and IL as common

constituents. The major difference in all the matrices is obviously based on the different polymers used. Since the addition of a metallic salt and IL has improved the device performance, we have now included that as two unavoidable ingredients in our polymer NC based RSD.

6.2.1 PVDF-HFP based hybrid device

The unique switching properties of PVDF-HFP as a polymeric host matrix, have already been studied in previous chapters [**1-3**].

The present switching matrix which includes PVDF-HFP_$AgNO_3$_IL exhibits excellent RS behaviour in terms of standard figures of merit. **Figure 6.1** shows the electrical characterization results carried out on the RSD. The electroforming process, in which the device moves from its pristine HRS to LRS usually takes place at a higher voltage bias when compared to set voltage. In the present case, it was found to be around 2.29 V (**Figure 6.1 a**) which corresponds to an electric field of 2.29 kV/cm. **Figure 6.1 b** shows the consecutive switching cycles after the electroforming process. As it can be noted from the figure, there is a clear reduction in the applied field. For the first 10 cycles, the IV loop was quite shrunk, and the On to Off ratio was about 5. This ratio improves in the following cycles, which can be due to the fact that, after electroforming (which took place at a high voltage), a thick and stable filament was formed (**Figure 6.1 c**). This resulted in shrunk initial cyclic sweeps leading to a small memory window. After 10s of cyclic testing, there might have been a breakage of the formed filament which led to a higher memory window (On/Off=10). **Figure 6.1 d** illustrates the On and Off current derived from the cyclic switching characteristics at a read voltage of 0.1 V. The device maintained an On/Off ratio of 15 throughout the working cycles. Even though this On/Off ratio is not a huge value, it should be noted that the device was able to switch continuously for more than 1000 cycles. This is the largest number of cycles reported so far for a planar device with an active gap of 10 μm.

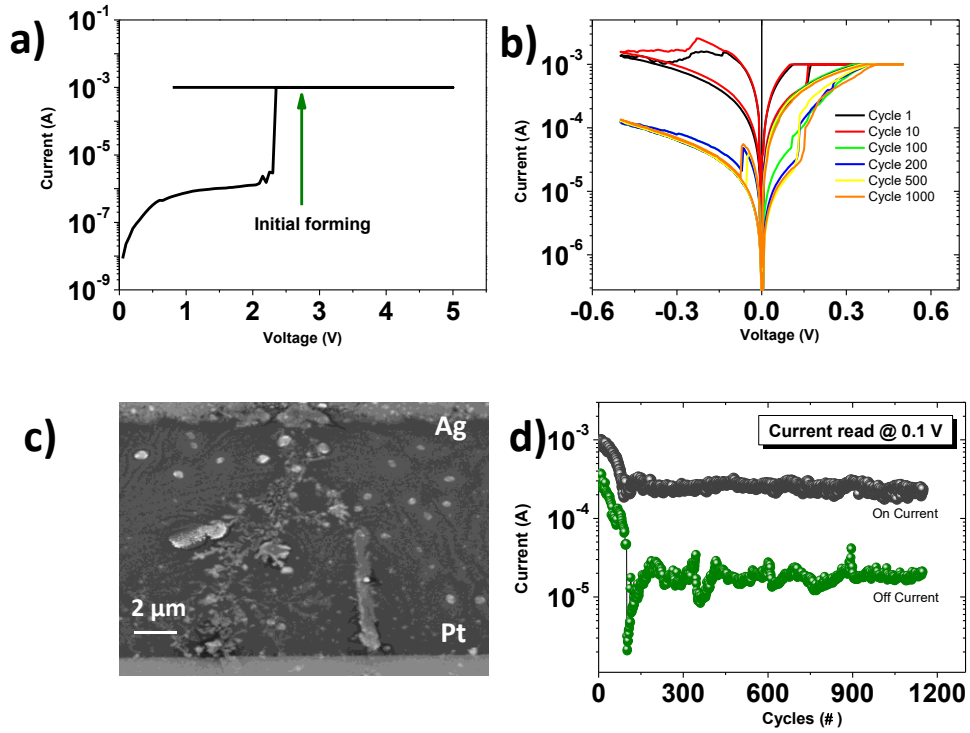

Figure 6.1: Electrical characterization performed on the planar asymmetric RSD with $AgNO_3$_IL_PVDF-HFP as switching matrix. a) Initial electroforming taking place at 2.29 V. b) Cyclic IV behaviour after forming. c) FESEM performed in the active switching gap of the RSD. d) On/Off current ratio at a read voltage of 0.1 V throughout continuous cyclic sweeps.

6.2.2 PEO based hybrid device

In this case where PEO is used as the switching matrix, the device exhibits excellent switching behaviour.

Figure 6.2 shows the electrical characterization results carried out on the RSD. Here the electroforming voltage was found to be around 8.4 V (**Figure 6.2 a**) which corresponds to a field of 8.4 kV/cm. **Figure 6.2 b** shows the consecutive switching cycles after the electroforming process. As it can be noted from the figure the further set took place at 3.4 V, which is 60% less than the initial forming voltage.

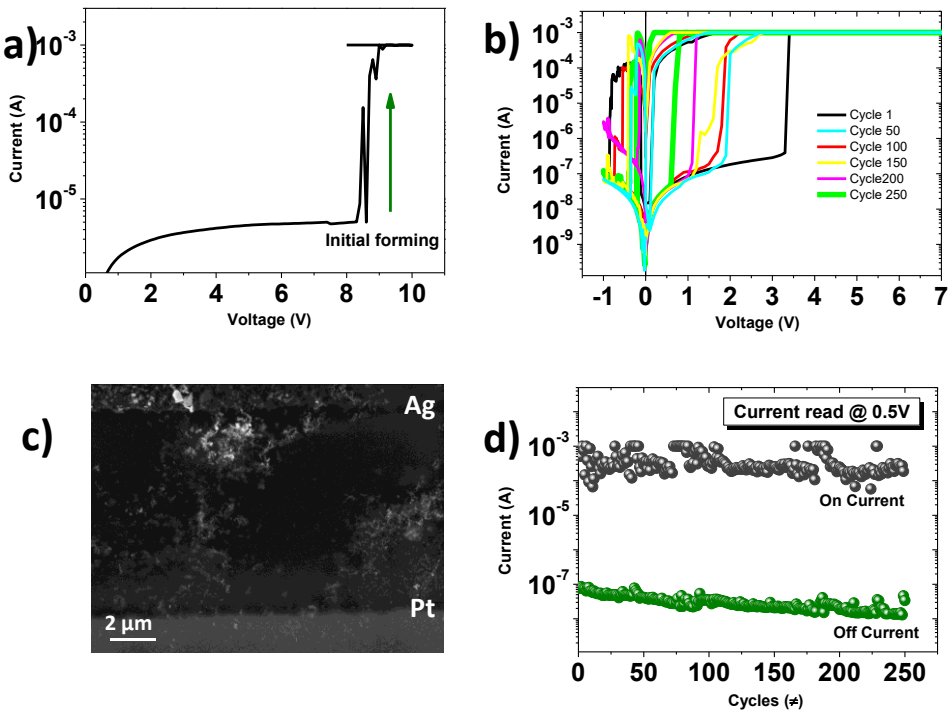

Figure 6.2: Electrical characterization performed on the planar asymmetric RSD with $AgNO_3$_IL_PEO as switching matrix. a) Initial electroforming taking place at 8.4 V. b) Cyclic IV behaviour of remaining cycles after forming. c) FESEM performed in the active switching gap of the RSD. d) On/Off current ratio at a read voltage of 0.5V throughout continuous cyclic sweeps.

It is quite evident from the cyclic sweep that the loop in this case (**Figure. 6.2 b**) is broader than in **Figure 6.1 b**. This means a higher On/Off ratio which in turn implies a larger memory window. **Figure 6.2 c** provides the active gap, where an evident path is present between the electrodes. **Figure 6.2 d** illustrates the On and Off currents derived from the cyclic switching characteristics at a read voltage of 0.5 V. The device maintained an On/Off ratio of 10^4 throughout the working cycles.

6.2.3 PMMA based hybrid device

PMMA is a well proven polymer matrix for resistive switching applications [**4, 5**]. The amorphous nature of this polymer provides a facile path for the movement of ions.

Figure 6.3 provides the electrical characterization performed on the PMMA based hybrid RSD.

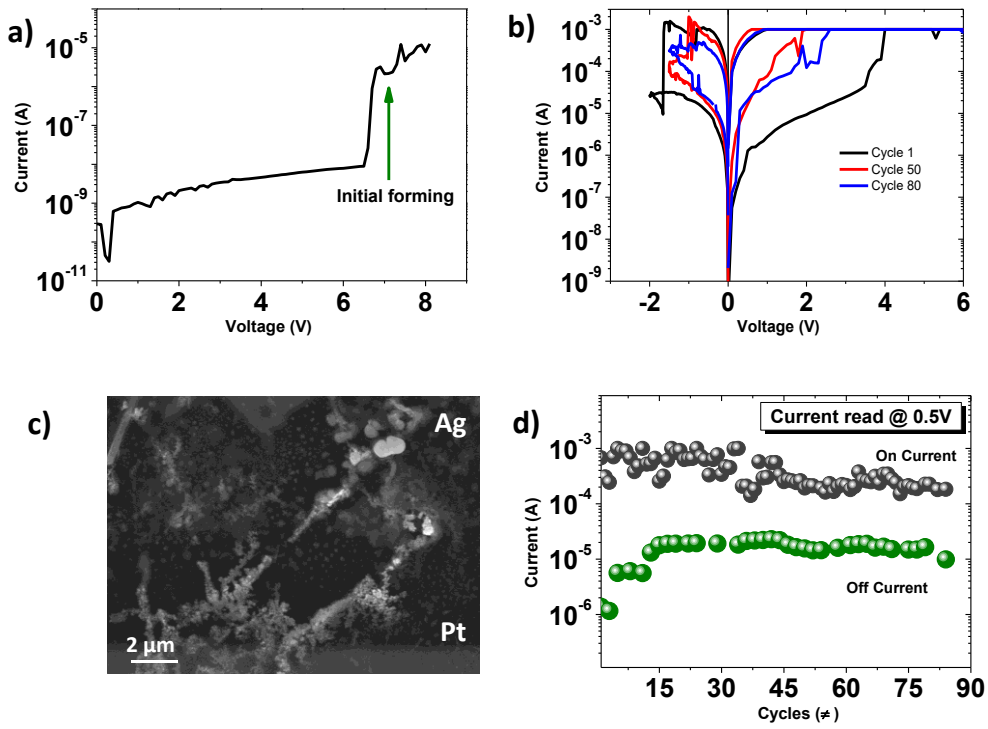

Figure 6.3: Electrical characterization performed on the planar asymmetric RSD with $AgNO_3$_IL_PMMA as switching matrix. a) Initial electroforming taking place at 6.5 V. b) Cyclic IV behaviour of remaining cycles after forming. c) FESEM performed in the active switching gap of the RSD. d) On/Off current ratio at a read voltage of 0.5V throughout continuous cyclic sweeps.

Here the forming was found to be around 6.5 V (**Figure 6.3 a**) which corresponds to an electric field of 6.5 kV/cm. **Figure 6.3 b** shows the consecutive switching cycles after the electroforming process. The set process taking place in the consecutive cycles has decreased after the initial forming. After first few cycles, the reset voltage range reduced and thus the negative sweep was limited to -1.5 V instead of -2 V. The On/Off ratio has also reduced in the following cycles, which can be due to the presence of the remaining stub of the already existing filament [**6**]. **Figure 6.3 c** provides the active gap, where an evident path is present between the electrodes. **Figure 6.3 d** illustrates the On and Off current derived from the cyclic switching characteristics at a read voltage of 0.5 V. The off current is not as stable as the on current. The On/Off ratio reduces with cycles, however on an average the On/Off ratio throughout the 85 cycles is 25.

6.3 Comparison study

Here we will compare the performance difference shown in these 3 matrices based on DSC and SEM characterization results. **Table 6.1** sums up the results obtained from the electrical characterisation of 3 switching matrices.

Table 6.1**:** Summary of the electrical measurement data obtained from the RSD using 3 polymer matrices.

Polymer matrix Polymer/$AgNO_3$/ IL	**Memory effect**	**Initial forming voltage (V)**	**On/Off ratio**	**Avg. LRS (Ω)**	**Avg. HRS (Ω)**	**Endurance**
PVDF-HFP	Non Volatile	2.3	15	400	4K	1200
PEO		8.4	10^4	1.3K	16M	250
PMMA		6.5	25	1.2K	30K	80

It can be seen that it was difficult to obtain all the desired characteristics of an RSD like endurance and On/Off ratio using one single polymer matrix. The contradictory objective of device simplicity and precision makes the development of RSDs very challenging. A general switching mechanism can be used to explain the transition in the resistance states. The pristine device is always found to be in High Resistance State (HRS). The application of positive bias causes the random movement of the silver ions in the matrix. In addition to this, the edge of the silver electrode (active electrode) is also oxidised to Ag^+ [**7**]. Thus the combined effect of movement of silver ions in the switching matrix, along with the movement of the oxidised silver ions from the silver electrode (anode) towards the counter platinum electrode (cathode), with the reduction of the silver ions at the platinum electrode (cathode) leads to the growth of a metallic filament causing the switching of the device to the On state. This process has been pictorially explained in chapter 5, section **5.4** (**figure 5.13**). Once the bias is reversed, the opposite reaction takes place, which is the dissolution of the formed continuous

path along with the formation of voids in the silver electrode. This leads to the Off state of the device. **Figure 6.4** provides the image of the RSDs with all the 3 different polymer matrices. The active switching gap before and after the electrical characterization has been shown.

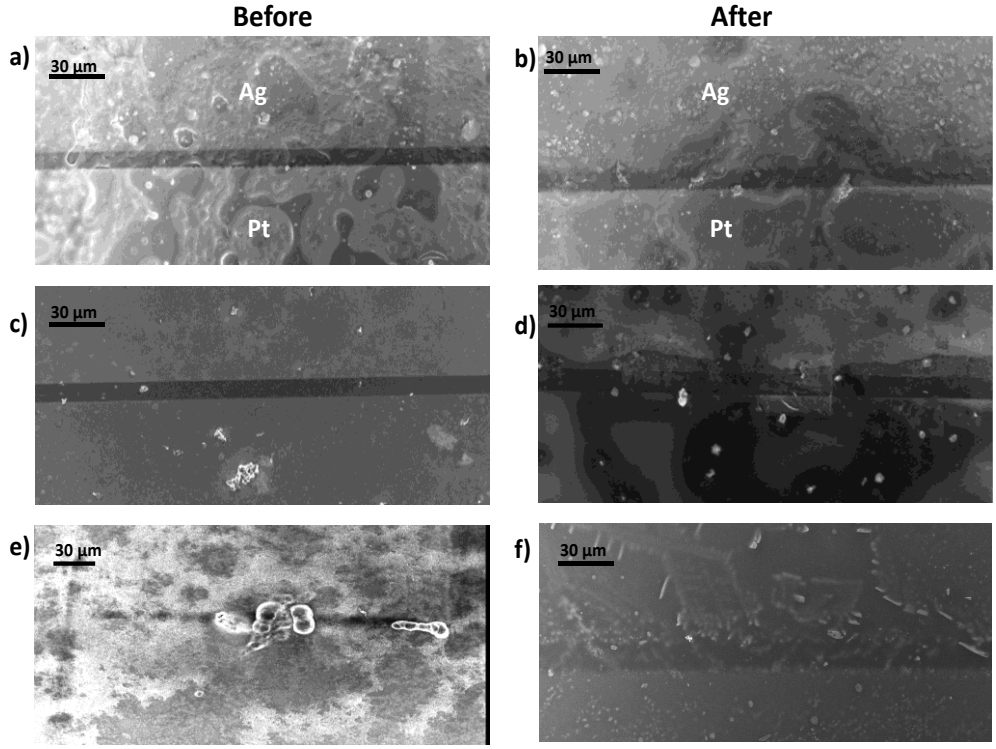

Figure 6.4: FESEM imaging on the active gap of the RSD before and after characterization. a,b: Device before and after characterization of A_gNO_3_IL_PVDF-HFP based matrix. c,d: Device before and after characterization of A_gNO_3_IL_PEO based matrix. e,f: Device before and after characterization of A_gNO_3_IL_PMMA based matrix.

As it can be seen from **figure 6.4** that all the images possess a major difference in the active gap before and after characterisation. The gaps before characterisation indicates a clear gap without any evident connection between the electrodes except in the case of RSD with A_gNO_3_IL_**PMMA** as switching matrix (**Figure 6.4 e** and **f**). The gap after electrical characterisation present an obvious connection between the electrodes which is the basis for the switching On and Off of the device. It was observed that in the case of PMMA based device, the active gap before characterization was not as clear as in other devices. The gap was completely covered by polymer switching matrix.

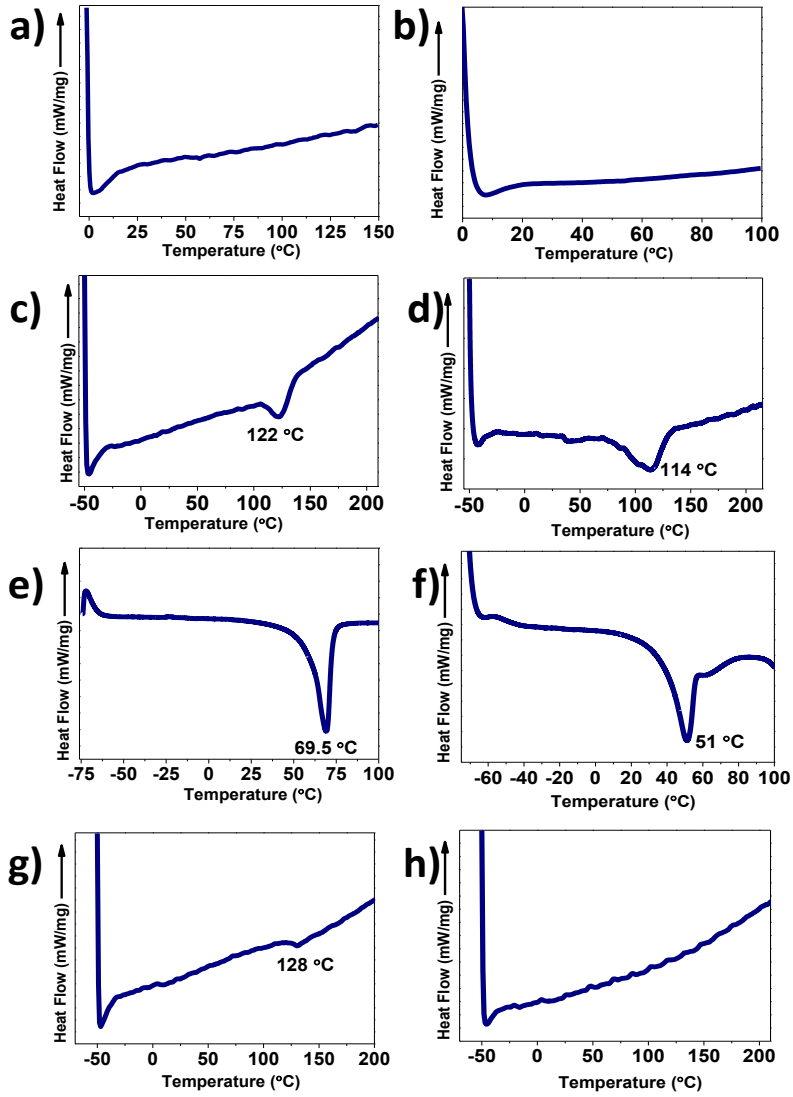

Figure 6.5: DSC thermograms of the polymer based switching composites and individual components of the switching matrix. a) A_gNO_3 b) IL c) PVDF-HFP. d) $AgNO_3$_IL_PVDF-HFP. e) PEO. f) $AgNO_3$_IL_PEO. g) PMMA. h) $AgNO_3$_IL_PMMA.

In order to well understand the electric behaviour of the switching composites, a discussion of the properties of the polymer matrices is required. Thus DSC of all the three switching polymer composites and the individual polymer matrices have been performed. **Figure 6.5** provides the DSC analyses. As it can be seen we have a clear reduction in the melting peaks of every switching matrices when compared to their corresponding individual polymers, except for PMMA, since it is an amorphous polymer. The melting peak corresponding to PVDF-HFP based switching matrix shows the highest melting

temperature at 114 ºC. The switching matrix corresponding to PEO has a melting peak at 51 ºC (**Figure 6.5 f**). **Figure 6.5 h** provides the DSC plot of the switching matrix corresponding to PMMA. As expected for an amorphous polymer, PMMA does not show any evident peak, except for a T_g around 128 ºC (**Figure 6.5 g**). As summarised in **Table 6.1**, the NC based on PVDF-HFP shows the highest number of switching cycles. This can be explained by the high crystallinity of $AgNO_3$_IL_PVDF-HFP matrix. The PVDF-HFP based switching matrix had a crystallinity of 20%, while the switching matrix based on PEO had a crystallinity of 7.5%. The percent crystallinity is determined using the below equation:

$$\% \text{ Crystallinity} = [(\Delta Hm)/\Delta Hm0] * 100\% \qquad (6.1)$$

Where, ΔHm is the heat of melting which is obtained by finding the area of the melting peak from the DSC thermogram of the switching matrix. ΔHm_0 is the reference value corresponding to the individual polymer if it were 100% crystalline. Values of ΔHm and ΔHm0 are given in **table 6.2.**

Table 6.2: Values of ΔHm and ΔHm0 of PVDF-HFP and PEO matrix

Polymer based switching matrix	**ΔHm (J/g)**	**ΔHm_0 (J/g)**
PVDF-HFP	21.05	104.7 [**8**]
PEO	14.86	197 [**9**]

In crystalline solids, the silver particles are localised in the amorphous regions at the grain boundary, as seen from SEM images (**Figure 6.6 a**). Thus, the higher number of switching cycles (1200) may be explained by a higher likelihood to form columnar percolative conductive paths. PEO based matrix is less crystalline and will have more amorphous regions where the Ag ions will be dispersed. During the breakage of the formed filament in the case of PEO, Ag ions will be expelled to those amorphous regions and a lower number of switching cycles (250) will appear. As discussed earlier, the set process in all the 3 cases can be explained by the movement of Ag ions in the matrix along with the oxidation of the Ag from the active electrode. The breakage of the formed filament can be explained by the movement of the silver ions from the formed filament back into

the matrix. Keeping this mechanism in mind, as the PEO-based switching matrix is less crystalline, the ions have a facile path for their movement. This leads to a proper breakage of the formed filament, leading to a higher Off resistance. Thus we obtain a higher memory window in the case of PEO (10^4). On the other hand in the case of PVDF-HFP the memory window is much smaller (15) due to its crystalline nature which makes the breakage of a formed filament less facile when compared to the device based on PEO.

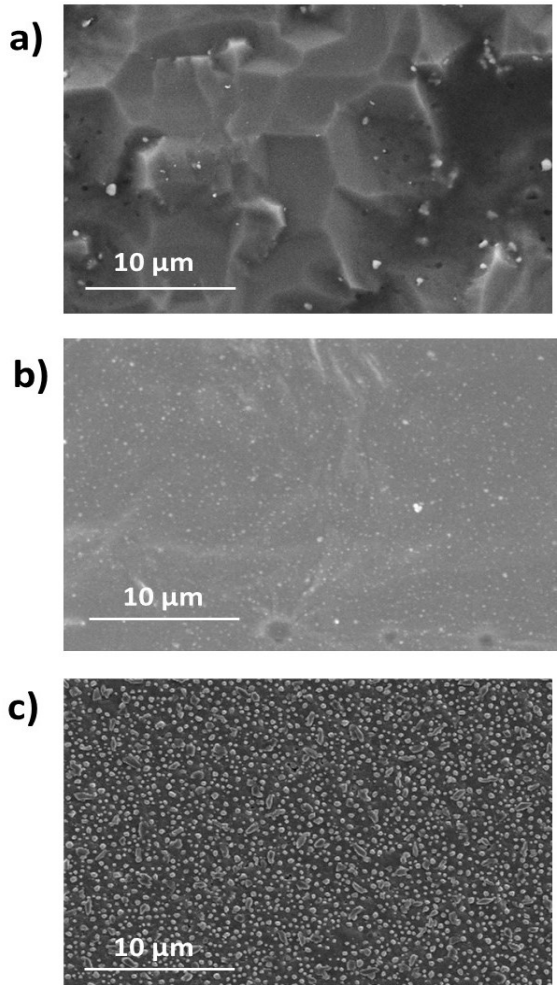

Figure 6.6: FESEM images of the films composed of 3 different NCs. a) $AgNO_3$_IL_PVDF-HFP. b) $AgNO_3$_IL_PEO. c) $AgNO_3$_IL_PMMA.

As seen from **figure 6.6 a,b**, a better distribution of Ag particles can be observed in the switching matrix based on PEO than in the one based on PVDF-HFP. Based on this observation we can explain the evident difference in the initial forming voltages in PVDF-HFP and PEO based RSDs. The presence of well

dispersed Ag NPs in PEO (**Figure 6.6 b**) leads to a comparatively higher set field (8.4 kV cm^{-1}), as here there are more particles ready for the filament formation. Thus, initially a higher field is needed for the particles which are well dispersed throughout the 10 × 300 µm switching gap to move and form a filament. While in the switching matrix with higher crystallinity (PVDF-HFP), good NP dispersion is not observed (**Figure 6.6 a**). They are agglomerated and grouped at certain positions, thus a comparatively lesser set field is sufficient for the formation of the filament (2.29 kV cm^{-1}). PMMA was the other selection of polymer host matrix, because of superior charge transport properties when used as a nanocomposite and also due to its widespread usage in commercial applications **[10, 11]**. It was found that the RSD based on PMMA_ $AgNO_3$_IL exhibited the lowest number of switching cycles (80) which can be attributed to the increased rate of scission of PMMA which led to the degradation of the polymer [**12**]. When subjected to electrical stress at ambient condition, the PMMA film might have undergone a degradation which might have led to the decreased number of switching cycles.

Thus at this point of research, a single switching matrix cannot be chosen as the ultimate matrix for RSDs, as each matrix has its own advantages and disadvantages. It can be noted that all the RSDs discussed here present good switching behaviour with reasonable endurance. The current study displays one of the most cost effective and effortless way to produce an RSD based on solution processable materials.

6.4 References

1. Rajan, K.; Bocchini, S.; Chiappone, A.; Roppolo, I.; Perrone, D.; Bejtka, K.; Ricciardi, C.; Pirri, C. F.; Chiolerio, A. (2017). Spin-coated silver nanocomposite resistive switching devices. *Microelectronic Engineering*, 168, pages 27-31.

2. Rajan, K.; Bocchini, S.; Chiappone, A.; Roppolo, I.; Perrone, D.; Castellino, M.; Bejtka, K.; Lorusso, M.; Ricciardi, C.; Pirri, C. F.; Chiolerio, A. (2017). WORM and bipolar inkjet printed resistive switching devices based on silver nanocomposites. *Flexible and Printed Electronics*, 2, 024002.

3. Rajan, K.; Chiappone, A.; Perrone, D.; Bocchini, S.; Roppolo, I.; Bejtka, K.; CAstellino, M.; Pirri, C. F.; Ricciardi, C.; Chiolerio, A. (2016). Ionic liquid-enhanced soft resistive switching devices. *RSC Advances*, 6, pages 94128-94138.

4. Tsao, H.Y.; Wang, Y. W.; Gao, Z. K. (2016). Resistive Switching Behavior of Ag/PMMA:Na/Ag Devices for Memory Applications. *Thin Solid Films*, 612, pages 61-65.

5. Cheng, B.; Zhao, J.; Xiao, L.; Cai, Q.; Guo, R.; Xiao, Y.; Lei, S. (2015). PMMA interlayer-modulated memory effects by space charge polarization in resistive switching based on CuSCN-nanopyramids/ZnO-nanorods p-n heterojunction**.** *Scientific Reports*, 5, 17859.

6. Valov, I.; Linn, E.; Tappertzhofen, S.; Schmelzer, S.; Hurk, J.; Lentz, F.; Waser, R. (2013). Nanobatteries in redox-based resistive switches require extension of memristor theory. *Nature Communications,* 4, 1771.

7. Valov, I.; Waser, R.; Jameson, J. R.; Kozicki, M. N. (2011). Electrochemical metalization memories- Fundamentals, application prospects. *Nanotechology*, 22, 289502.

8. Rudhziah, S.; Mohamed, N. S.; Ahmad, A. (2013). Conductivity and Structural Studies of Poly(vinylidene fluoride co-hexafluoropropylene)/Polyethyl methacrylate Blend Doped with Ammonium Triflate. *International Journal of Electrochemical Science*, 8, pages 421-434.

9. Pfefferkorn, D.; Kyerematen, S. O.; Busse, K.; Kammer, H. W.; Albrecht, T. T.; Kressler, J. (2011). Crystallization and Melting of Poly(ethylene oxide) in Blends and Diblock Copolymers with Poly(methyl acrylate). *Macromolecules*. 44, Pages 2953-2963.

10. Kim, H. M.; Kim, K.; Lee, S. J.; Joo, J.; Yoon, H. S.; Cho, S. J.; Lyu, S. C.; Lee, C. J. (2004). Charge transport properties of composites of multiwalled carbon nanotube with metal catalyst and polymer: Application to electromagnetic interference shielding. *Current Applied Physics,* 4, pages 577-580.

11. Zeng, Q. H.; Yu, A. B.; Lu, G. Q.; Paul, D. R. (2005). Clay-based polymer nanocomposites: Research and commercial development. *Journal of Nanoscience and Nanotechnology,* 5, pages 1574-1592.

12. Dawes, K.; Glover, L. C.; Vroom, D. A. (2007). The Effects of Electron Beam and g-Irradiation on Polymeric Materials. Physical properties of polymer handbook (P. 867-887).Springer New York.

Chapter 7

PMMA based ultra-low voltage switching device

7.1 Introduction

Electronic devices that consumes low power are always preferred and a lot of research is being done in this regard. When it comes to computing power of devices, a compromise is made between the computing power and the power consumption. By consuming less power, the system will be less expensive to run. By following the Moore's law, the density and the speed of IC computing elements have increased exponentially [**1,2**], but with this fast paced increase, the major concern which limits the computing power is the power dissipation.

Even though the energy consumed by a single CMOS logic has fallen exponentially with the shrinkage in feature size, the overall power consumption of a new personal computer has been increasing every year by 22% [**1**]. The current scenario which is happening is that as the circuit dimension is decreasing, the leakage current is becoming more prominent, which leads to a power consumption even when no switching is taking place. This current usually accounts for half the power consumed by the IC. In this scenario, as there are several efforts happening to build a new memory system with array of memristors, sneak path current is a major issue [**3**]. Selectors [**4-7**] are threshold switching devices that can be used to mitigate the issue of sneak path current without compromising the scalability and 3D stacking capability of memristor. Some of the most important features of a memristor or any switching device is that it should be able to switch at a great

speed with low power consumption. The present work discussed in this chapter introduces a new polymer NC based device which switches at micro volts range in nanoseconds.

7.2 PMMA and Au NP based threshold switching device

The device we tested has a PMMA. A2 (Common positive photoresist) and Au NP composite based switching matrix. The preparation of this matrix has been well explained in chapter 2, section **2.3.6**. A stacked symmetrical device with Au electrodes is used as the device structure (Chapter 2, section 2.2.3.2).

Figure 7.1 provides the electrical characterization results carried out on the device. As seen from **figure 7.1 a**, the device shows a very stable switching behavior throughout the switching cycles. The device shows a switching in the negative cycle, while a LRS is maintained in the positive cycle (**Figure 7.1 b**). This is a peculiar behavior, as we always see the switching at a negative voltage around -250 μV. This is so far the lowest switching voltage reported. Even though we see a switching taking place, the resistance levels in both LRS and HRS are very small. The device has an average LRS of about few tens of ohms. While the HRS is not stable. The variation happening in the HRS is huge (180 to 1100Ω). On an average the On/Off in the case of these devices is around 10 (**Figure 7.1 c**). Since the DC sweeps provide a good endurance, a pulse test was also conducted on the device. As it can be seen from **figure 7.2 a**, the device was made to read at -10 mV and – 100 μV. The initial -10 μV was applied just to be sure that the device was in its HRS. As seen from the DC sweeps, even when pulse was given to the device, the HRS was very unstable (**Figure 7.2 b**). The red circled regions in **figure 7.2 a** shows the exact points where the current was read. As seen from **figure 7.2 b**, the device was made to operate for more than 30,000 cycles. As mentioned in the beginning of this chapter as the device switches at a very low voltage, the switching speed was calculated. The speed at which the device turn ON and turn Off was calculated.

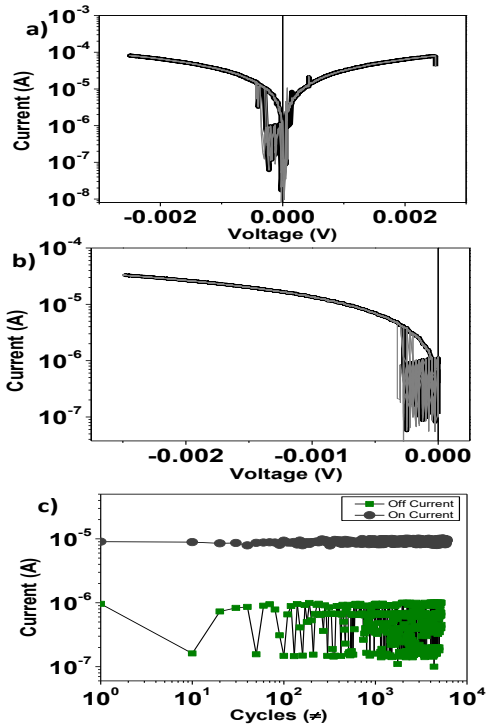

Figure 7.1: Electrical Characterization performed on the device. a) Cyclic IV performed on the device. b) Closer look at the negative cycle. c) On and Off current read at -180 µV from the cyclic IV curve

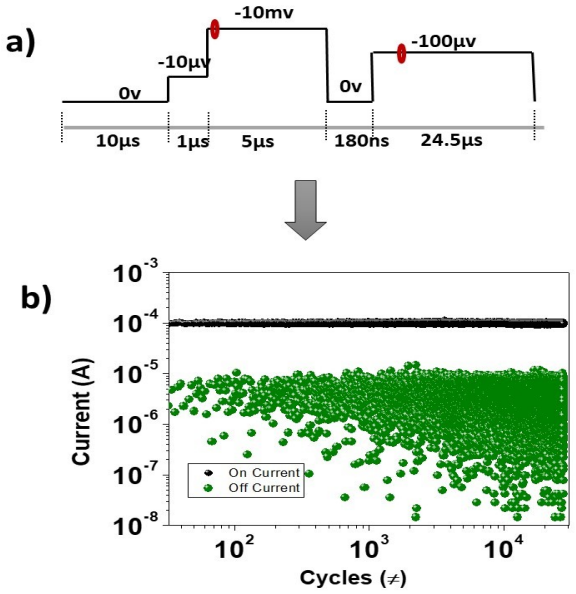

Figure 7.2: Pulse endurance performed on the device. a) Pulse input. b) Output

7.3 Device Switching Speed Analysis

The turn On and turn Off speed of any selector or switching device is a fundamental parameter. Since the device turns On at a low voltage, it was important to find the switching speed at this particular voltage range.

Figure 7.3 shows the electrical characterization tests which were performed to check the device turn On speed at various set voltages. **Figure 7.3 a** shows the pulse that was used to turn On the device. A set voltage of -700mV was used to turn On the device. As it can be seen from **figure 7.3 b**, how the turn On speed has been calculated. The device has switched at a speed of less than 20 ns. A lot of set voltages were tried in order to study the trend of switching speed. It was found that the set voltage and the turn On delay had an inverse relation. Higher the set voltage, lesser was the turn on delay or faster was the switching speed (**Figure 7.3 c**). Here as the set voltage increases, the switching medium gets less resistive leading to a faster turn On of the device. It should be noted that we cannot increase the operating voltage much as this leads to an increase in the power consumption.

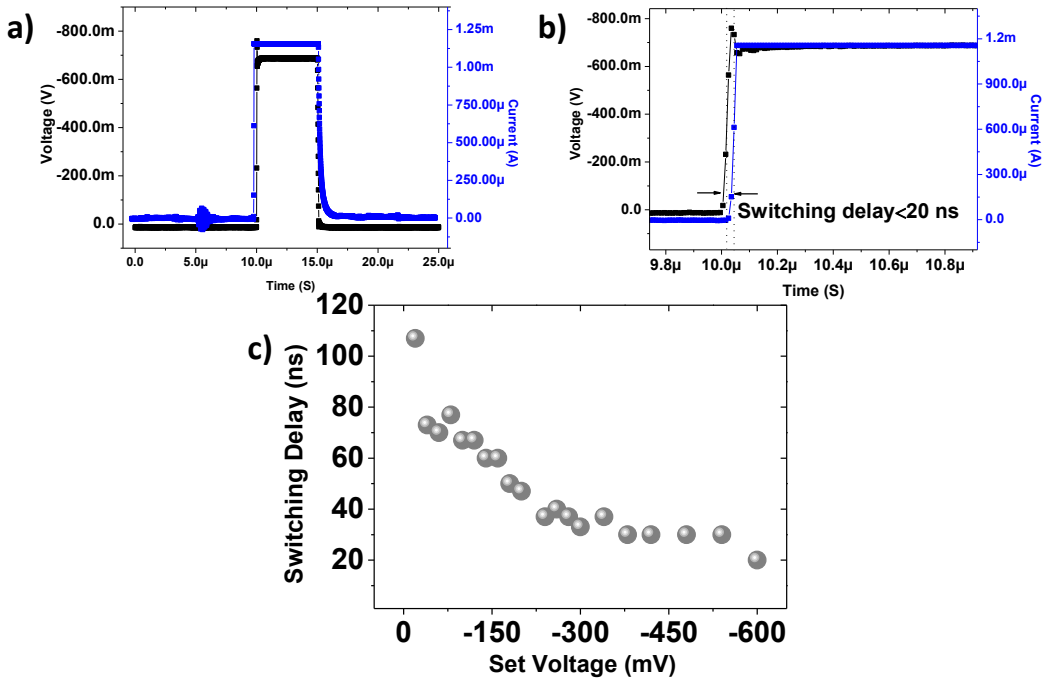

Figure 7.3: Switching speed determination test. a) Input pulse in black and the output current obtained (blue). b) The zoom in section of the switching part. c) Plot of switching speed as a function of set voltage

Figure 7.4 shows the electrical characterization tests which were performed to check the device turn Off speed at various set voltages. **Figure 7.4 a** shows the pulse that was used to turn Off the device. A reset voltage of -20 mV was used to turn Off the device. As it can be seen from **figure 7.4 b**, how the turn Off speed or the relaxation time has been calculated. The device has switched off at 5.5 µs, after the switching bias has been turned off. A lot of voltages were tried in order to study the trend of relaxation speed. It was found that the applied voltage and the relaxation time had a direct relation. Higher the time needed for the device to relax, higher was the applied voltage (**Figure 7.4 c**).

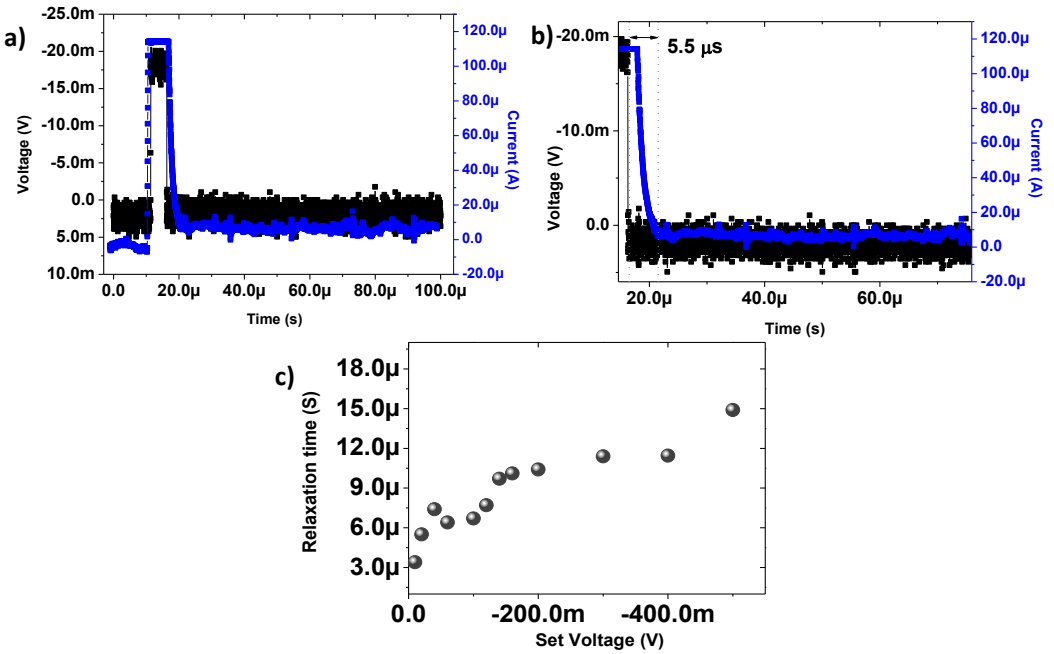

Figure 7.4: Relaxation time determination test. a) Input pulse in black and the output current obtained (blue). b) The zoom in section of the relaxed part. c) Plot of relaxation time as a function of set voltage

Figure 7.5 provides the temperature based measurement carried out on the device in which the switching On speed at various temperatures (265 K to 400 K) have been plotted.

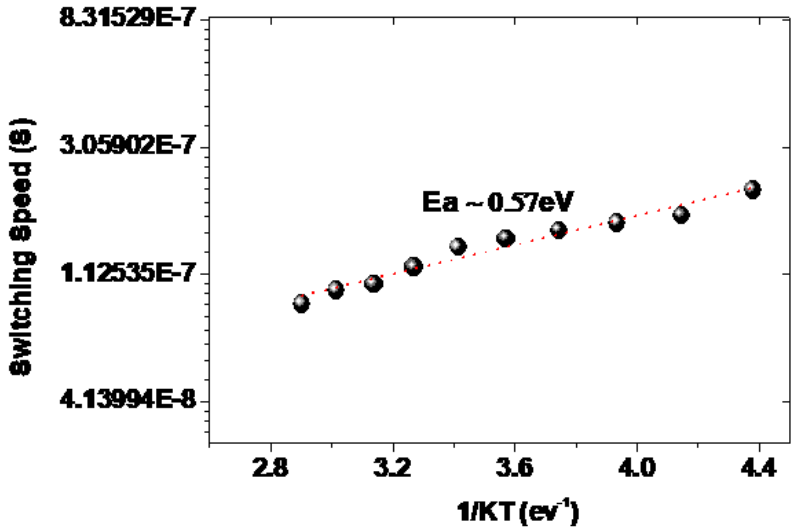

Figure 7.5: Arrhenius plot: Switching speed plotted as function of Temperature

Figure 7.5 is plotted using the below equation.

$$t = t_0 \exp(E_a/K_b T) \qquad (7.1)$$

The linear trend of the switching speed with respect to the inverse of temperature shows that the On state of the device follows the Arrhenius law. An activation energy (E_a) of 0.57 is extracted from the plot which suggests that ionic conduction is taking place in the device. As the device shows a temperature dependence, we can assume that there is more chance for a filamentary conduction to take place. Since the device is in its early experimental stage, a clear switching mechanism cannot be explained. A possible means of conduction can be explained as follows. The low resistive state of the device in its positive bias range can be explained by the highly conductive polymer NC matrix. The Au NPs in the matrix has reached its percolation level and thus the matrix is highly conductive. With the application of a negative bias, Coulomb blockade comes into play. This phenomena comes into play when the device is very small. With negative bias, the electrons inside the device strongly repel the other electrons to flow into the device, resulting in a high resistance state. This HRS is continued until the voltage reaches a certain threshold where the device moves to a LRS under an electrostriction effect due to the application of a certain high electric field. This field causes an overall strain in the device which makes the Au NPs to come closer and lead to the LRS of the device (**Figure 7.6**).

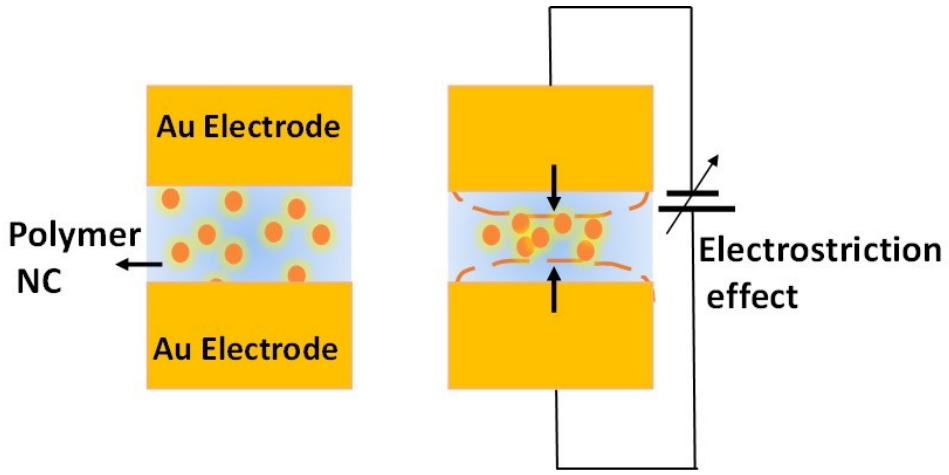

Figure 7.6: Schematic plot showing the state transition of the device due to Electrostriction effect

The high speed switching and the ultra-low voltage that the device requires for switching, makes this device a serious candidate for future memory devices (mainly for switching applications).

7.4 References

1. Paul DeMone. "The Incredible Shrinking CPU: Peril of Proliferating Power". 2004 [http://www.realworldtech.com/shrinking-cpu/3/].

2. Moore, G.E. (1965). Cramming more components onto Integrated Circuits. *Electronics*, 38, pages 114-117.

3. Shevgoor, M.; Muralimanohar, N.; Balasubramonian, R.; Jeon, Y. (2015). Improving memristor memory with sneak current sharing. *IEEE International Conference on Computing Design*, pages 549-556.

4. Midya, R.; Wang, Z.; Zhang, J.; Savelev, S. E.; Li, C.; Rao, M.; Jang, M. H.; Joshi, S.; Jiang, H.; Lin, P.; Norris, K.; Ge, N.; Wu, Q.; Barnell, M.; Li, Z.; Xin, H. L.; Williams, R. S.; Xia, Q.; Yang, J. J. (2017). Anatomy of Ag/Hafnia based selectors with 10^{10} nonlinearity. *Advanced Materials*, 29, 1604457.

5. Wang, Z.; Joshi, S.; Savelev, S. E.; Jiang, H.; Midya, R.; Lin, P.; Hu, M.; Ge, N.; Strachan, J. P.; Li, Z.; Wu, Q.; Barnell, M.; Li, G. L.; Xin, H. L.; Williams, S. R.; Xia, Q.; Yang, J. J. (2017). Memristors with difusive dynamics as synaptic emulators for neuromrphic computing. *Nature Materials*, 16, pages 101-108.

6. Song, J.; Woo, J.; Prakash, A.; Lee, D.; Hwang, H. (2015). Threshold selector with high selectivity and steep slope for crosspoint memory array. *IEEE Electron Device Letters*, 36, pages 681-683.

7. Hurk, J. V.; Linn, E.; Zhang, H.; Waser, R.; Vaolv, I. (2014). Volatile resistance states in electochemical metallization cells enabling non-destructive readout of complementary resistive swicthes. *Nanotechnology*, 25, 425202.

Chapter 8

Summary and Conclusion

8.1 Summary of Results

In the present research work carried out, we have developed various polymer NC hybrid RSDs. The electrical characteristics and the switching mechanism of each of these were studied in detail. Various characterization techniques were used in order to study and confirm our research hypothesis.

The initial work was based on metallic Ag NPs dispersed in a polymer medium. A planar symmetrical device architecture was used in this case. The switching mechanism was explained by means of Ag filament formation along with the clusterization of Ag NPs in the polymer matrix. The device showed a strong switching dependence on the compliance current level set. An increase in current compliance level led to a stronger and stable filament corresponding to a non-volatile memory state. This switching matrix was found to be a promising candidate in the field of printed electronics.

Redox based resistive switching memories which are considered to be the promising candidate for future memory technologies due to their high operating speed, low power consumption and high endurance led us to replace the Ag NPs by $AgNO_3$ and to incorporate RTIL into the polymer matrix. It was seen that the incorporation of RTIL to the switching matrix helped in imparting non-volatility to the device and also helped in the reduction of the set voltage range, which can be related to improved ionic mobility, facile path for ionic movement and reduced crystallinity and viscosity of the switching matrix. A clear dendritic filament

growth was observed by FESEM imaging in between the electrodes, proving the formation of a silver NP conducting filament which led to the change in the state of the device. Even though both planar and stacked structures have been used for the research purpose, main importance have been given for planar device structure as they are easier to be designed and also they are of great importance for the development of the future generation of wearable, eventually printed, soft microelectronic systems. The current study also unlocks an important pathway towards engineering the electrode design for upcoming RSDs where the electric field induced filament growth can be well controlled. The choice of a planar architecture, can be considered very promising in terms of reliability for the next generation of wearable soft neuromorphic devices.

The final part of the thesis explains very briefly about high speed switching ultra-low power selector device. The switching characteristics obtained from this device is really excellent. More changes have to be made on the device structure and on the switching matrix in order to stabilize the HRS. Further research has to be carried on this regard since the HRS of the device is really low. **Figure 8.1** displays the time frame throughout the PhD period during which various experiments were carried out.

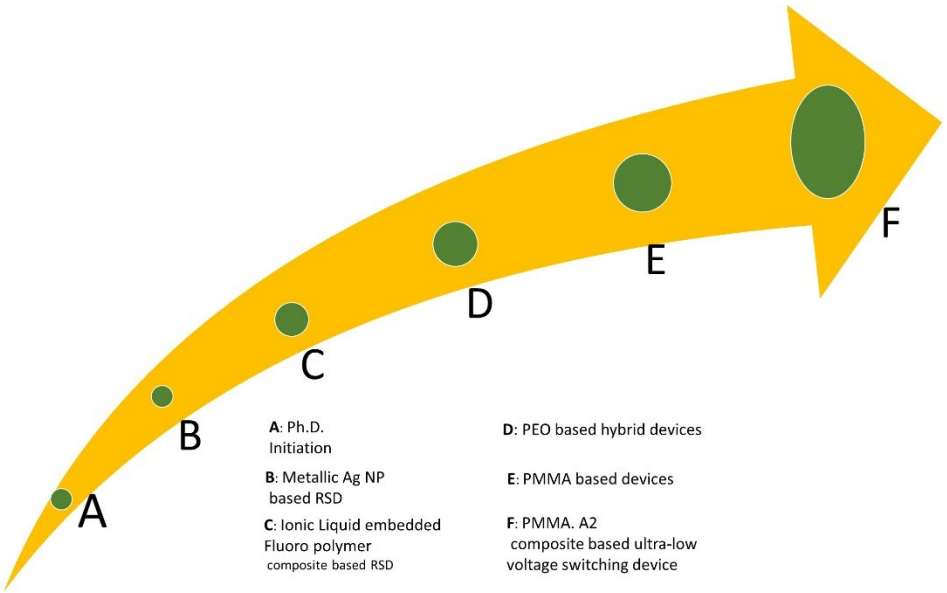

Figure 8.1: Ph.D. Work Time frame

Table 8.1 provides the summary of results obtained so far. The table provides the main features of various RSDs.

Table 8.1: Table summarizing the entire results obtained so far

Active matrix and deposition technique	Device architecture	On/ Off	Cyclic Stability	Non Volatility	Retention(s)
Ex-situ Ag NPs (Spin coat and inkjet printing)	Planar (Symmetrical Au elect.)	65	<10	✓	
In-situ Ag NPs (spin coat)	Stacked structure (ITO and Au)	100	<10	✓	
$AgNO_3$:PVDF-HFP (spin coat)	Planar (Symmetrical Au elect.)			✗	
$AgNO_3$:PVDF-HFP:IL (spin coat)	Planar (Symmetrical Au elect.)	20	100	✓	$>10^4$
$AgNO_3$:PVDF-HFP:IL (spin coat)	Stacked structure (ITO and Au)	100	70	✓	
$AgNO_3$:PEO:IL (spin coat)	Planar (Symmetrical Au elect.)	10	100	✓	500
$AgNO_3$:PEO:IL (spin coat)	Planar (Asymmetrical Ag and Pt elect.)	10^4	>500	✓	$>10^4$
PEO:IL (spin coat)	Planar (Asymmetrical Ag and Pt elect.)	(10^4 - 20)	80	✓	$<10^3$
$AgNO_3$:PVDF-HFP:IL (spin coat)	Planar (Asymmetrical Ag and Pt elect.)	10-15	1200	✓	$<10^3$
$AgNO_3$:PMMA:IL (spin coat)	Planar (Asymmetrical Ag and Pt elect.)	30	80	✓	
PMMA.A2:Au (spin coat)	Stacked structure (Symmetrical Au elect.)	10	>30,000	✗	

8.2 Conclusion and Future Outlook

The three years research work was focused on the development of an organometallic hybrid RSD and its characterization. A thorough study on the Resistive Switching properties and the nonlinear current-voltage behavior were performed. A clear understanding on the filamentary based resistive switching devices based on various polymer composite matrices have been presented. We have presented some potential results which make this work promising. The possibility of printing these polymer based matrices is a great step in introducing flexible RSDs which can be used in bendable and wearable electronics. Although the present devices are designed and characterized for resistive switching applications (Memory devices), these matrices and devices can be employed for developing soft neuromorphic devices in future. The possibility of metallic Ag NP based RSDs to be utilized to emulate short and long term plasticity is promising. This is due to the similar behavior of Ag atoms in the switching matrix as that of the synaptic inflow and outflow of Ca^{2+} which forms the basis of memory and learning. PMMA.A2 based ultra-low voltage switching device can be used as a switch for Nonvolatile RSDs. Since this device switches at a low power, this can be an ideal switch. By optimizing its design, it can be a frontrunner for future selector devices.